Master Thesis in Geosciences

Fresnel-based infill analysis and image quality

by

Miao Li

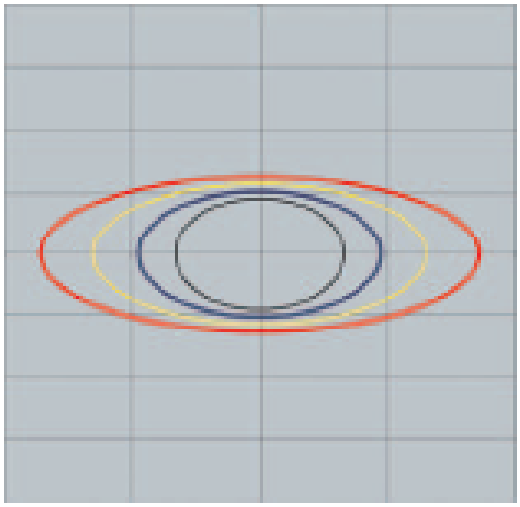

UNIVERSITY OF OSLO

FACULTY OF MATHEMATICS AND NATURAL SCIENCES

Fresnel-based infill analysis and image quality

by

Miao Li

Master Thesis in Geosciences

Discipline: Geophysics

Department of Geosciences

Faculty of Mathematics and Natural Sciences

UNIVERSITY OF OSLO

01.June.2010

Tutor(s): **Leiv-J Gelius (**Department of Geosciences, Faculty of Mathematics and Natural Sciences, University of Oslo), **Sandvin Ottar** (Fugro As Oslo)

This work is published digitally through DUO – Digitale Utgivelser ved UiO

http://www.duo.uio.no

It is also catalogued in BIBSYS (http://www.bibsys.no/english)

Acknowledgements

This work was carried out at Fugro Seismic imaging As Norway. I would like to appreciate Dr Xiaoping Li for giving this opportunity to cooperate with Fugro. I also thank my external supervisor Ottar Sandvin for providing me with this interesting thesis topic and for giving me the needed assistance and support. I am also thankful to all the processing staff members who gave me a lot of help and support during my thesis work.

I am also thankful to the internal supervisor Leiv-J Gelius at the Department of Geosciences, University of Oslo. This thesis would never be accomplished without his constructive instruction and encouragement.

Last I am grateful for the encouragement and attention of my parents and friends in China.

Miao Li
01/06/2010 Oslo

Abstract

In a 3D marine survey, often large areas of poor coverage (‘coverage holes’) exist caused by feathering during the actual acquisition. Infill management is introduced to fill those ‘coverage holes’, but a high percentage of infill shooting will increase the cost of time and economy in the real survey. Recently, based on the concept of the Fresnel zone, a new infill management technique, called the Fresnel zone binning, was introduced by Monk (2010). In this article, the theoretical formulas to calculate and construct the Fresnel zone binning for different offsets and velocity cases were introduced. In my thesis, this new Fresnel zone binning technique will be tested against ray tracing simulations in NORSAR3D. Based on ray tracing and time migration, the Fresnel zone binning calculated by the theoretical formulas will be evaluated. The overall goal is to see if this new concept can effectively decrease the percentage of the infill shooting and improve the quality of seismic imaging.

Table of contents

Chapter 1 Introduction

1.1 infill management

In a 3D marine survey, the traditional common-cell bins are constructed and used in the data processing after the actual acquisition. The typical dimension of the rectangular bin cell in a 3D marine survey is 12.5m ×37.5m (Yilmaz 1988). However, the complete survey area will normally not be well illuminated during the seismic acquisition and there are several 'coverage holes' caused by the feathering.

To overcome this coverage problem ('coverage holes'), infill management is applied to decide how much infill shooting is required. Figures 1.1 (a) and (b) show that for a typical survey, the size of the 'coverage holes' is small at near offset and gradually increases at middle and far offsets due to stronger feathering. A criterion involving the amplitude loss is always employed when making a judgment if the survey area is well covered by the seismic acquisition. In a real survey, the requirement of infill management is strict at near offset (1dB amplitude loss) and conversely, at far offset, slightly more relaxed (2dB amplitude losses).

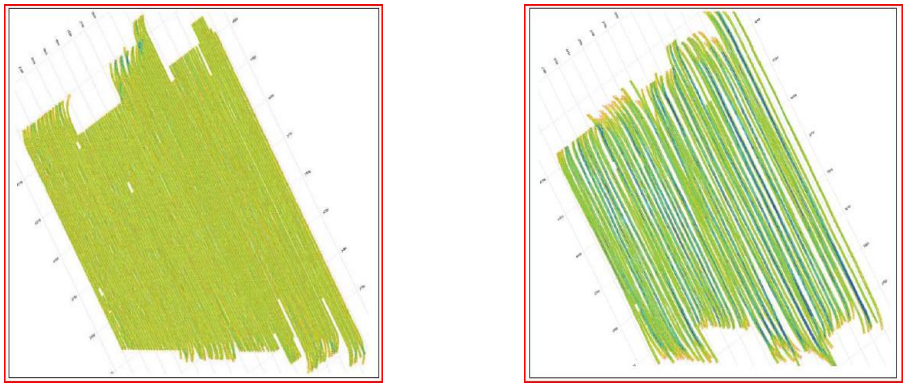

(a) (b)

Figure 1.1: The 'coverage holes' at respectively near offset (a) and far offset (b) (Monk 2009)

Some methods of infill management have been proposed to decrease the percentage of infill shooting. For example, Lindsy (1989) pointed out that the number of 'coverage holes' will decrease if the topography of the survey area is well investigated before the actual seismic acquisition. Capelle (2008) demonstrated an effective decrease in the percentage of infill shooting after a series of infill management were employed, such as varying the bin size with offset, introducing new equipments and trace interpolation during processing. Strand.et al (2008), demonstrated that the percentage of infill shooting was decreased by steering the vessel along pre-defined lines. A new acquisition technique, called wide-azimuth towed streamer (WATS)

(Long. A, 2006), is also applied to fill in 'coverage holes' during the actual seismic acquisition.

Recently, based on the concept of Fresnel zone, a new technique called Fresnel zone binning (Monk 2010), was introduced as a possible method to effectively decrease the percentage of infill shooting and correspondingly improve the quality of the coverage map.

1.2 Fresnel zone and Fresnel zone binning

The basic definition of the Fresnel zone can be found several places in the literatures (see f.ex. Sheriff,1980). The Fresnel zone is defined by the area of non-specular points that have a one-way travel path no more than one quarter wavelength different from that of the specular point. An illustration of the Fresnel zone is shown in Figure 1.2.

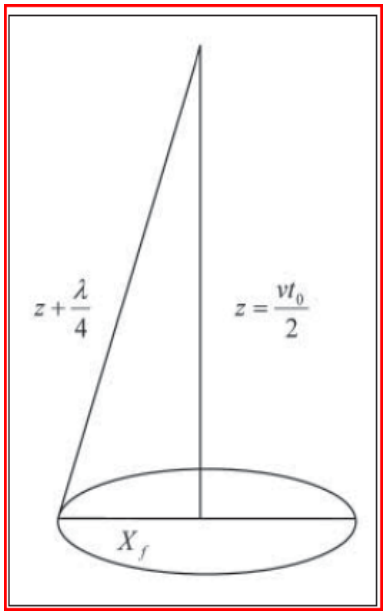

Figure 1.2: Illustration of the Fresnel zone after Monk (2010)

The Fresnel zone will be circular in case of zero-offset, constant velocity and a horizontal surface. In case of an offset the shape of the Fresnel zone will be elliptical. Replacing a constant-velocity model with a gradient-velocity model still gives an elliptical shape of the Fresnel zone in case of a horizontal reflector. Figure 1.3 shows how the size of the Fresnel zone increases with depth and that at near offset the shape is circular and gradually becomes elliptical with increased offset.

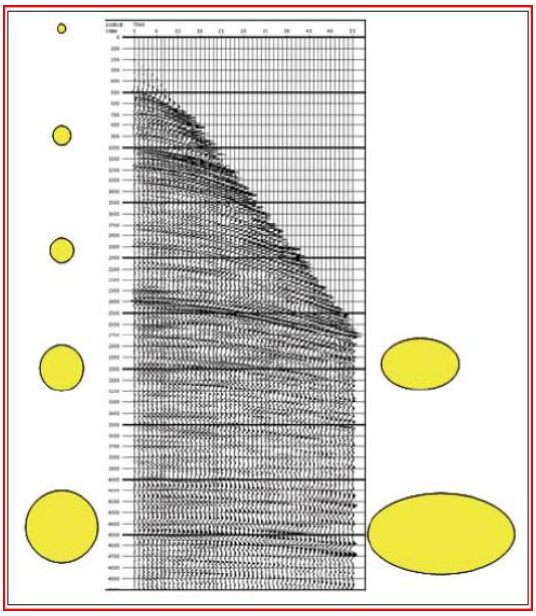

Figure 1.3: Variation of the size and shape of the Fresnel zone varies with depth and offset (Monk, 2009).

Monk (2010) gives formulas describing the dimension/shape of the Fresnel zone for both a constant-velocity and gradient velocity case. In case of zero-offset and constant velocity, the radius of the circular Fresnel zone is given as:

$$X_f = \sqrt{(Z_f + \frac{\lambda}{4})^2 - {Z_f}^2} \qquad (1.1)$$

Where X_f is the radius of the Fresnel zone, Z_f is the depth of surface, and λ is the center wave-length. This formula can be further approximated (due to λ^2 is small compared to depth Z_f) (Sheriff 1980):

$$X_f \approx \frac{V}{2}\sqrt{t_0 \tau} \qquad (1.2)$$

Where V is the constant sediment velocity, τ is the center period and t_0 is the one-way travel time in case of zero offset.

In case of an offset case, Monk (2010) made use of the Double Square Root (DSR) equation (Claerbout, 1985) for a constant velocity (V) and finite offset (h):

$$t = \sqrt{\frac{t_0^2}{4} + \frac{(x+h)^2}{V^2}} + \sqrt{\frac{t_0^2}{4} + \frac{(x-h)^2}{V^2}} \qquad (1.3)$$

to derive an expression for the crossline width of the Fresnel zone:

$$Y_F = \sqrt{L_1^2 - Z_f^2 - h^2} \qquad (1.4)$$

Where Z_f is the depth of the surface and h is the half-offset between shot and receiver. The term L_1 is defined by the one way ray path distance L and the half-wavelength ΔL, e.g. $L_1 = 0.5(2L + \Delta L)$. Figure 1.4 shows a sketch of the corresponding geometry.

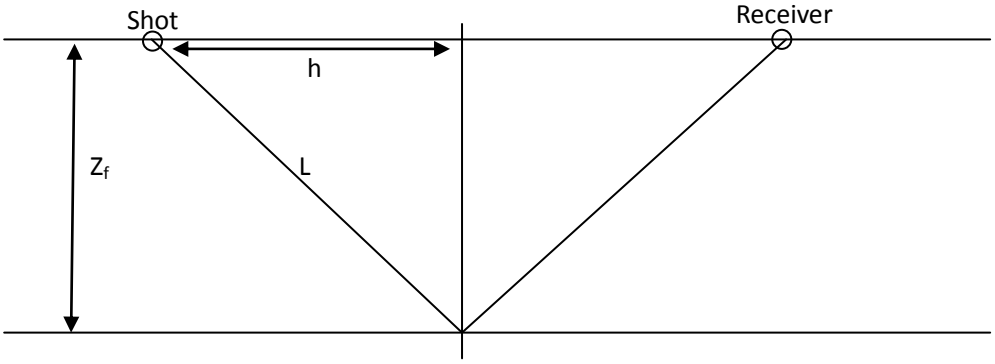

Figure 1.4: Sketch of geometry illustrating Eq. (1.4)

Monk (2010) suggests that the dimension of the Fresnel zone in the inline direction can be estimated from this expression:

$$X_F = \frac{Y_F}{\cos(\theta)} \qquad (1.5)$$

Where θ is the angle of incidence as illustrated in Figure 1.5.

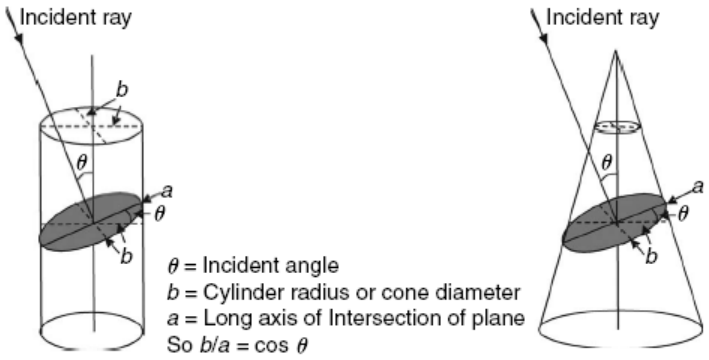

Figure 1.5: The angle of incidence θ approximated as the intersection of a cylinder and a plane (Monk, 2010).

In his paper, Monk (2010) also provided Fresnel zone formulas in case of a gradient-velocity model:

$$Y_F = \sqrt{\frac{(\cosh(g(t_x + \Delta t) - 1))\left(2V_0(V_0 + gZ_F)\right)}{g^2} - Z_F^2 - h^2} \qquad (1.6)$$

And

$$X_F = \frac{Y_F}{\cos(\theta)} \qquad (1.7)$$

Where g is the velocity gradient, Z_F is the depth of surface, h is half-offset, V_0 is the initial velocity, and Δt is one-quarter of the period. Based on the same approximation as in case of constant velocity, the dimension of the Fresnel zone in the inline direction (X_F) is determined by Y_F via the angle of incidence. The term t_x represents the one-way travel time and is given explicitly as

$$t_x = \left(\frac{1}{g}\right)\cosh^{-1}\left[1 + \frac{g^2(h^2 + z^2)}{2V_0(V_0 + gz)}\right] \qquad (1.8)$$

Based on these theoretical formulas, the corresponding Fresnel zone 'bins' can be constructed at various offsets. Figure 1.6 shows a sketch of the Fresnel zone bin and the traditional common cell bin.

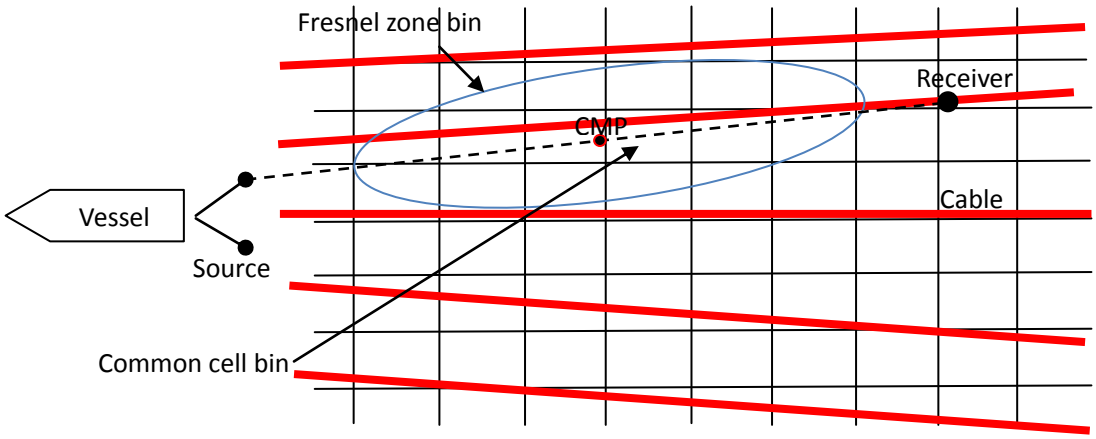

Figure 1.6: Sketch of the Fresnel zone bin (blue circle), and the common cell bin (black rectangles) in case of cables (solid red lines) with feathering.

As seen from Figure 1.6, the Fresnel zone bin utilizes the idea that a given trace contains information from not only the specular point but from an area defined by the Fresnel zone. By adding Fresnel zones corresponding to all possible source-receiver combinations for a given survey and introducing an amplitude criterion to approve the

potential Fresnel zone bin infills, an improved coverage can be obtained. By employing a reasonable amplitude criterion, the quality of migration is hopefully preserved.

The concept of Fresnel zone binning can be used in two ways:

1. To actually reduce the ‘coverage holes’ in the acquired 3D data based on Fresnel zone mapping.

2. To perform an analysis to identify which remaining areas need to be reshooted (based on an amplitude criterion).

In the next chapters analyzing the actual robustness and applicability of this new binning concept will be the focus of this thesis work.

Chapter 2: Fresnel zone binning

The concept of Fresnel zone binning introduced in the article of Monk (2010), as opposite to the traditional nominal bin, gives a possible new strategy to decide the level of infill shooting required to fill in 'coverage holes' caused by feathering in the survey area. The basic criterion of Fresnel zone binning, as discussed in Chapter 1, is based on the fact that seismic arrivals from a target horizon are associated with a Fresnel zone rather than specular points only. Hence these Fresnel zones can be employed in infill management. In order to investigate the concept of Fresnel zone binning further, two different models were generated using NORSAR3D: a simple model consisting of four flat horizons and a more complex model simulating more realistic geological conditions. Furthermore, navigation lines corresponding to an offshore survey area were employed to define a realistic survey geometry including feathering.

2.1 Simple Model

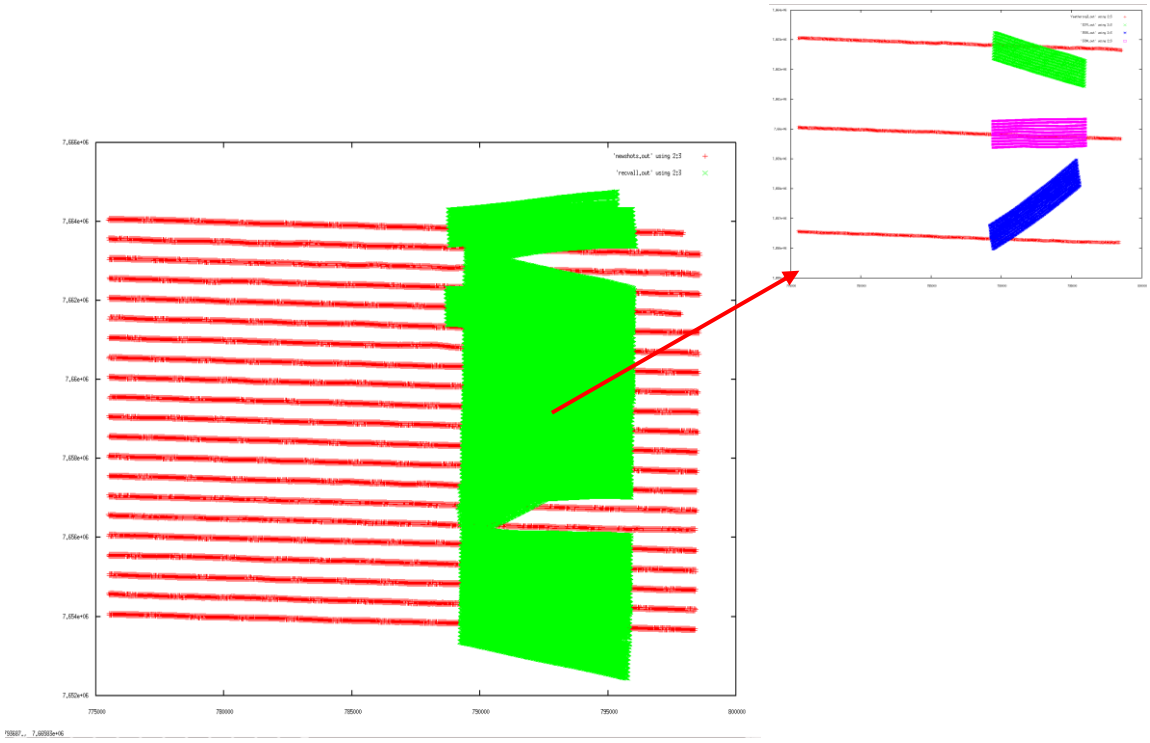

Figure 2.1: Survey area included all navigation lines (total of 21 lines shown by red colors) in case of the simple model. The corresponding streamers associated with a single shot along a given navigation line shown by green color. In the sub-figure, the featherings in three navigation lines were selected.

The survey geometry applied to the simple model is described in Figure 2.1. For a fixed shot-point, the corresponding steamer points associated with three selected

navigation lines are indicated. The feathering is clearly observed, especially at the middle and far offsets. The survey area is 30km along the inline direction and 25km along the crossline direction. The basic parameters of investigation are listed in table 2.1:

Table 2.1: Acquisition parameters

Parameters:	Inline offset (m)	Cable length (m)	Number of cables	Cable separation (m)	CDP offset (m)	Crossline offset (m)
	200	6600	10	100	6.25	25

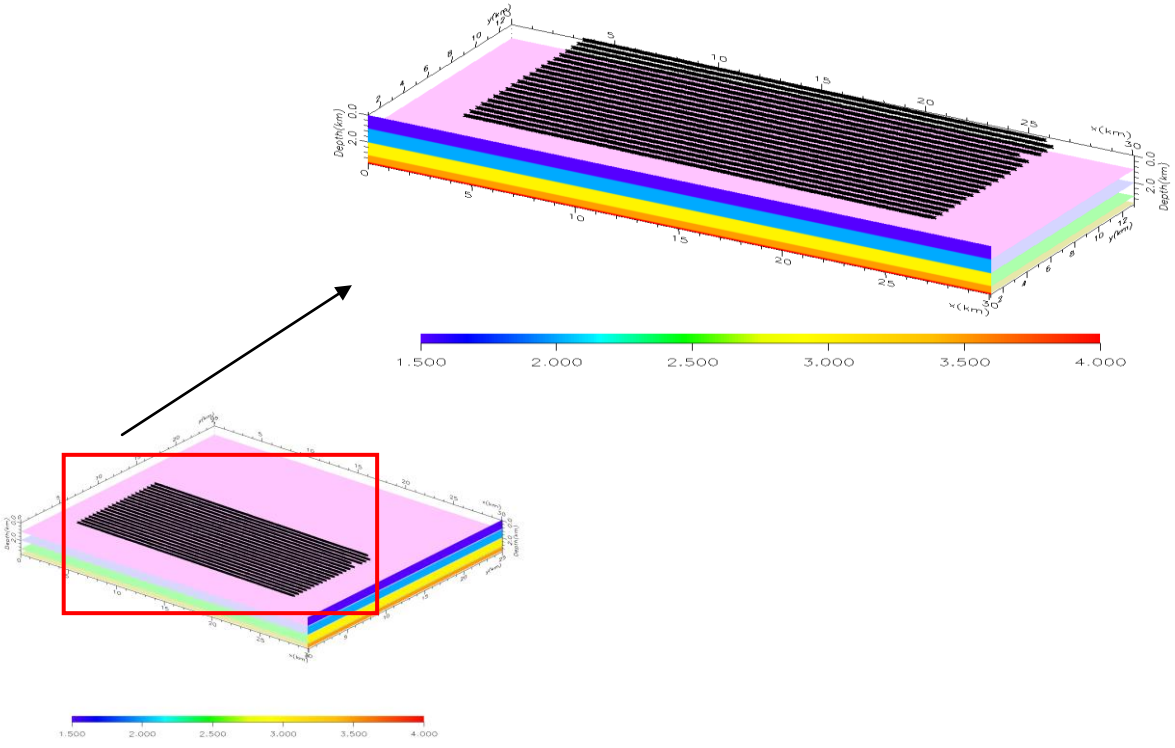

Figure 2.2: Geometry of the simple NORSAR3D model and the acquisition layout defined by navigation lines; the survey area is shown in the low-left sub-figure.

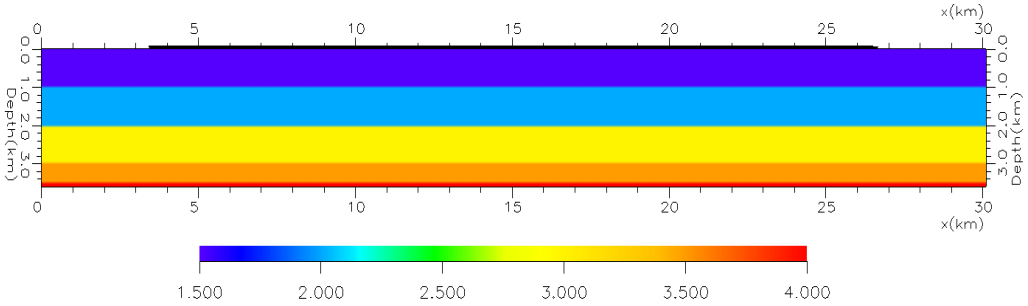

Figure 2.3: Velocity model of each layer

As shown in Figure 2.2, the simple model is composed by four horizontal layers located at a depth of 1km, 2km, 3km and 3.5km respectively. The velocity of each layer is respectively 1.5km/s (average velocity in the sea), 2.0km/s and 3.5km/s. A reasonable frequency should also be assigned to each layer because the size of the Fresnel zone is also influenced by frequency. The governing rule is that frequency is gradually decreased with depth because of absorption. All basic parameters used in the simulations are given in Table 2.2.

Table 2.2: Key parameters associated with the simple model

	Depth (km)	Velocity (km/s)	Frequency (Hz)
Horizon 1	1	1.5	60
Horizon 2	2	2	50
Horizon 3	3	3	30
Horizon 4	3.5	3.5	20

Following offset defines, the distance between a given source and receiver. In the experiment three different ranges of offset (half-offset) were considered: near offset (0.248km), middle offset (1.739km) and far offset (3.358km). The size of the Fresnel zone (the length of half axis) in the two directions parallel and perpendicular to the shot-receiver axis were calculated for all four horizons at near offset. (Table 2.3).

Table 2.3: The size of the Fresnel zone at near offset

	Horizon1	Horizon2	Horizon3	Horizon4
Xpara (km)	0.127	0.203	0.390	0.558
Xperp (km)	0.124	0.201	0.388	0.556

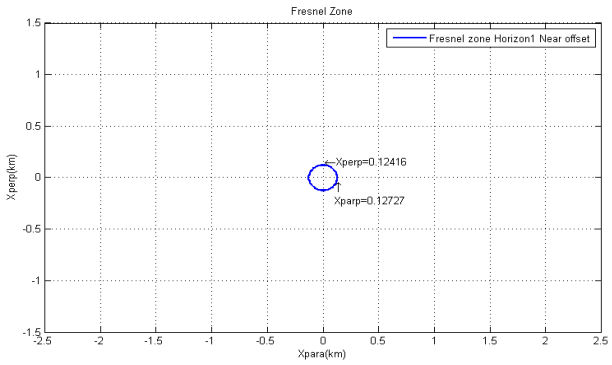

(a)

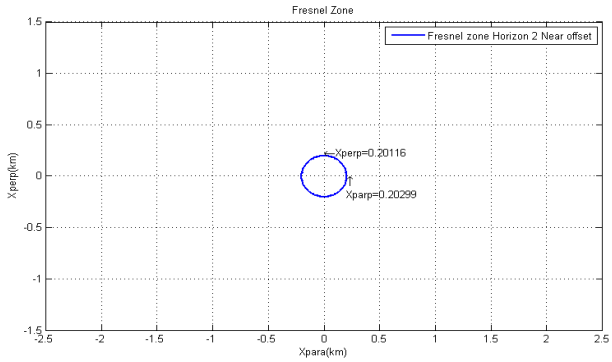

(b)

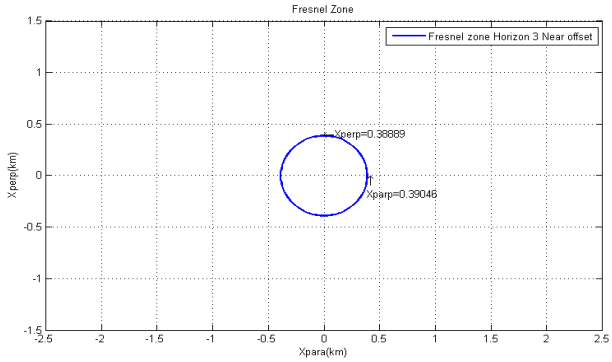

(c)

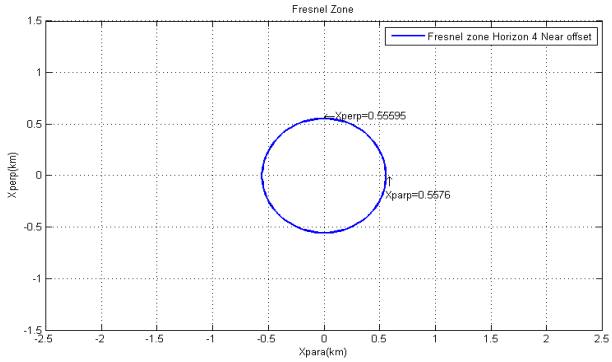

(d)

Figure 2.4 (a)-(d): The size of the Fresnel zone associated with each of the four horizons at near offset.

Moreover, Figures 2.4 (a)-(d) show the real size of the Fresnel zone along each horizon. From these figures, it is obvious that the size of the Fresnel zone gradually increases with the depth of a horizon and that its shape is close to a circle at near offset. Formula (1.4) in Chapter 1 describes the Fresnel zone width perpendicular to the direction of the shot-receiver axis in case of constant velocity and finite offset. By introducing explicitly the definition for L_1, this formula can be slightly modified as follows:

$$Y_F = \sqrt{L\Delta L + \frac{1}{4}(\Delta L)^2} \tag{2.1}$$

$$X_F = \frac{Y_F}{\cos(\theta)} \tag{2.2}$$

Where L is the one way ray path distance given by $\sqrt{h^2 + Z_f^2}$ (h is the half-offset and Z_f is the depth of horizon), ΔL is half wavelength given by $\frac{V}{2f}$ (V is the constant velocity and f is frequency). From Eqs (2.1) and (2.2), it is reasonable that the size of the Fresnel zone at a fixed near offset will increase with depth to each horizon because the velocity increases and the frequency decreases.

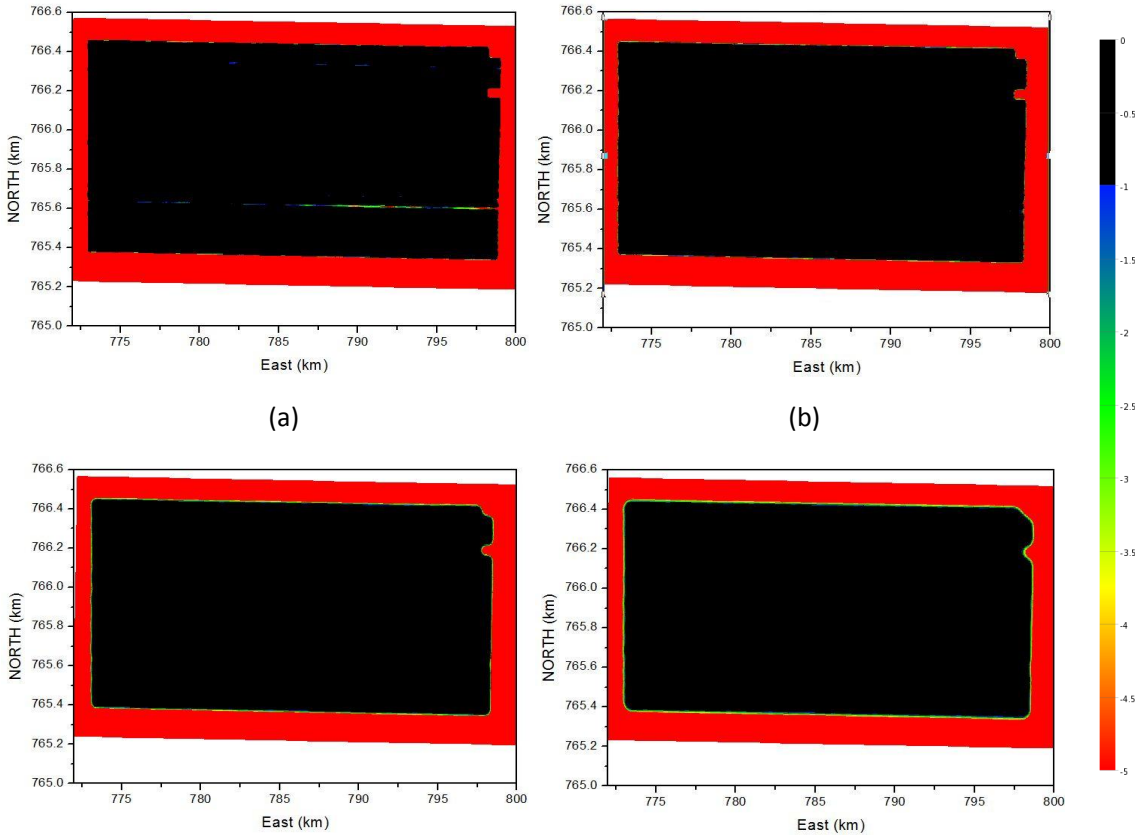

Figure 2.5 (a)-(d): The coverage along each of the four reflectors after Fresnel zone binning analysis (near offset): (a): horizon 1; (b) horizon 2; (c) horizon 3; (d) horizon 4

Figures 2.5 (a)-(d) show the resulting coverage after Fresnel zone binning along each horizon (near offset). The coverage is computed by adding all Fresnel zones corresponding to each shot along the navigation lines and applying an amplitude criterion. In order to be able to estimate the coverage of a given horizon one needs a criterion to judge if the amplitudes have not degraded too much. In general, the requirement in the infill management is that the amplitude loss in dB should be less than 1 dB at near offset. However, in some cases and especially at far offsets, amplitude loss down to 2dB is also acceptable if feathering is strong. At near offset, the feathering is not as serious as at far offset during the acquisition. From Figure 2.5 it follows that the size of the Fresnel zones are large enough to overcome the feathering at near offset and there are no obvious coverage holes along each horizon even though the amplitude loss requirement is restricted to 1dB. Therefore, the conclusion is that the coverage of each horizon at near offset is good enough after Fresnel zone binning has been applied.

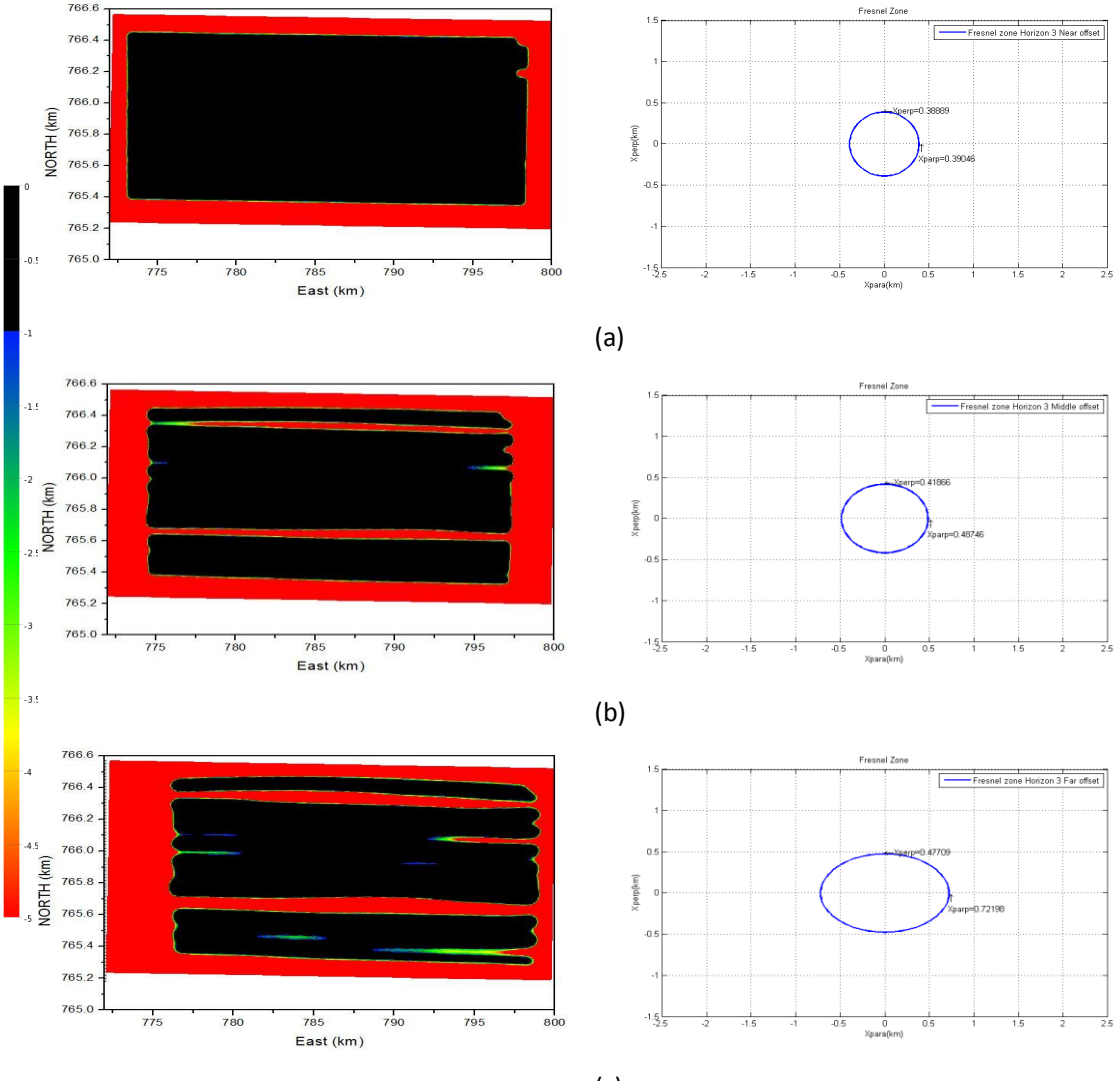

Figure 2.6 (a)-(c): The coverage on the horizon 3 after Fresnel zone analysis (left) and the size and shape of the corresponding Fresnel zone (right) on the horizon 3 at near, middle and far offset. (a) near offset; (b) middle offset; (c) far offset.

From the theory in Chapter 1, the size of the Fresnel zone increases with offset. In addition, the shape of the Fresnel zone is stronger elliptical at far offset. Horizon 3 in the simple model is now chosen as a target reflector to further analyze the Fresnel zone binning concept. Figures 2.6 (a)-(c) show the coverage along the target horizon for different offset ranges (left) and the corresponding Fresnel zones (right). At medium and far offsets, there exist obvious 'coverage holes' with amplitude losses down to more than 1dB. The tabulated size of the Fresnel zone along horizon 3 for the offset ranges considered is listed in Table 2.4.

Table 2.4: The size of the Fresnel zone along horizon 3 (near offset to far offset)

	Near offset	Middle offset	Far offset
Xpara (km)	0.390	0.487	0.722
Xperp (km)	0.388	0.419	0.477

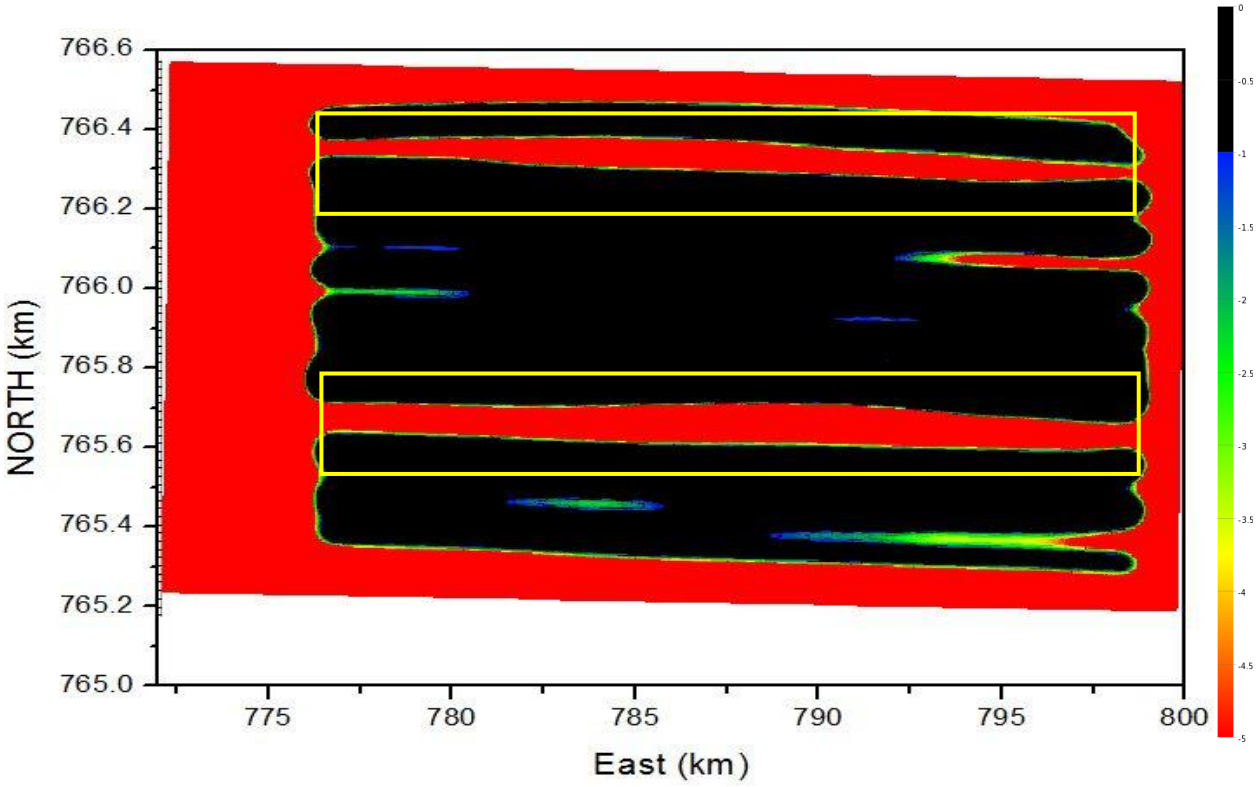

Figure 2.7: The coverage of horizon 3 at far offset (simple model).

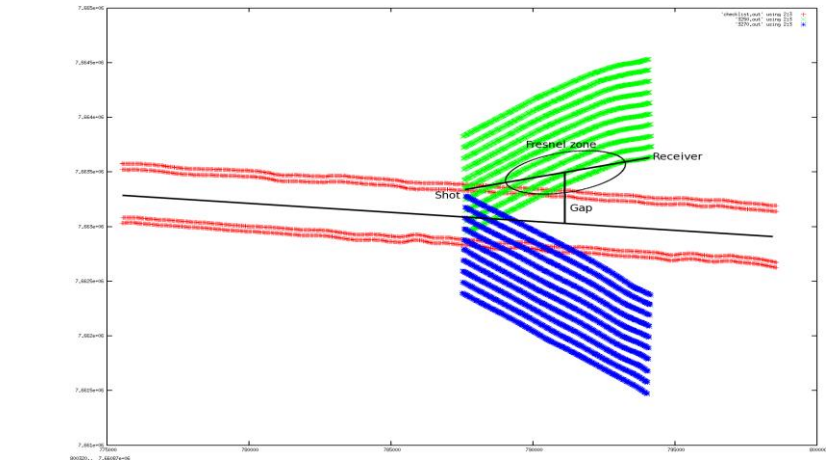

(a)

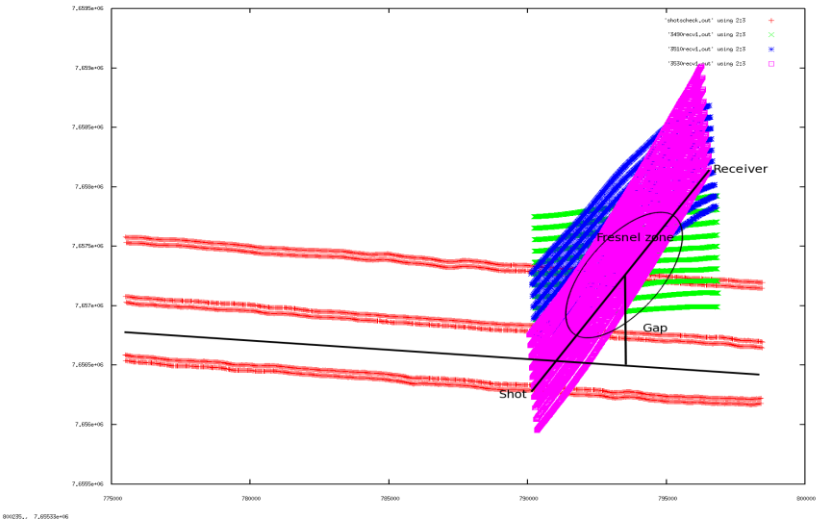

(b)

Figure 2.8 (a)-(b): Two examples of strong feathering with navigation lines and all receivers associated with one shot (the Fresnel zone plotted in the figure is not true size but merely gives its direction).

At middle and far offsets, two larger 'coverage holes' (amplitude loss below -5dB) can be seen in Figures 2.6 (b) and (c). In Figure 2.7 an amplified version of the coverage of horizon 3 at far offset is shown, and where the areas of poor coverage are framed by two yellow rectangles. The reason to these large 'coverage holes' is the strong feathering during acquisition. Two navigation lines with corresponding cable positions for a single shot located inside the upper yellow frame of Figure 2.7 are shown in Figure 2.8a. The direction and size of the Fresnel zone at far offset are also sketched. Although the half width of the Fresnel zone in the direction perpendicular to the shot-receiver axis is approximately 0.47km, their directions being highly non-parallel with the navigation lines imply that the area between these two lines can not be covered by Fresnel zone binning. Hence, large holes in the coverage will still exist due to this extreme feathering.

In the lower yellow frame in Figure 2.7, similar arguments can explain the large

'coverage holes'. Considering now Figure 2.8b where navigation lines located in this area are selected. As before, the location of all receivers for one shot is also plotted. In this figure, it can be easily observed that the directions along shot-receiver pairs are highly non-parallel to the navigation line and that the angle between the cable and navigation line is quite large, even close to 90 degrees. As a result, although the size of the Fresnel zone at horizon 3 at far offset is not that small (approximately 0.5km in the direction perpendicular to shot-receiver direction), the area covered by Fresnel zone binning can not compensate this strong feathering.

In the example considered a real 3-D acquisition geometry was employed involving two cases of extreme cable feathering. It was clearly demonstrated that if the Fresnel zones are highly non-parallel to the navigation lines, Fresnel zone binning fail to compensate.

2.2 Complex Model

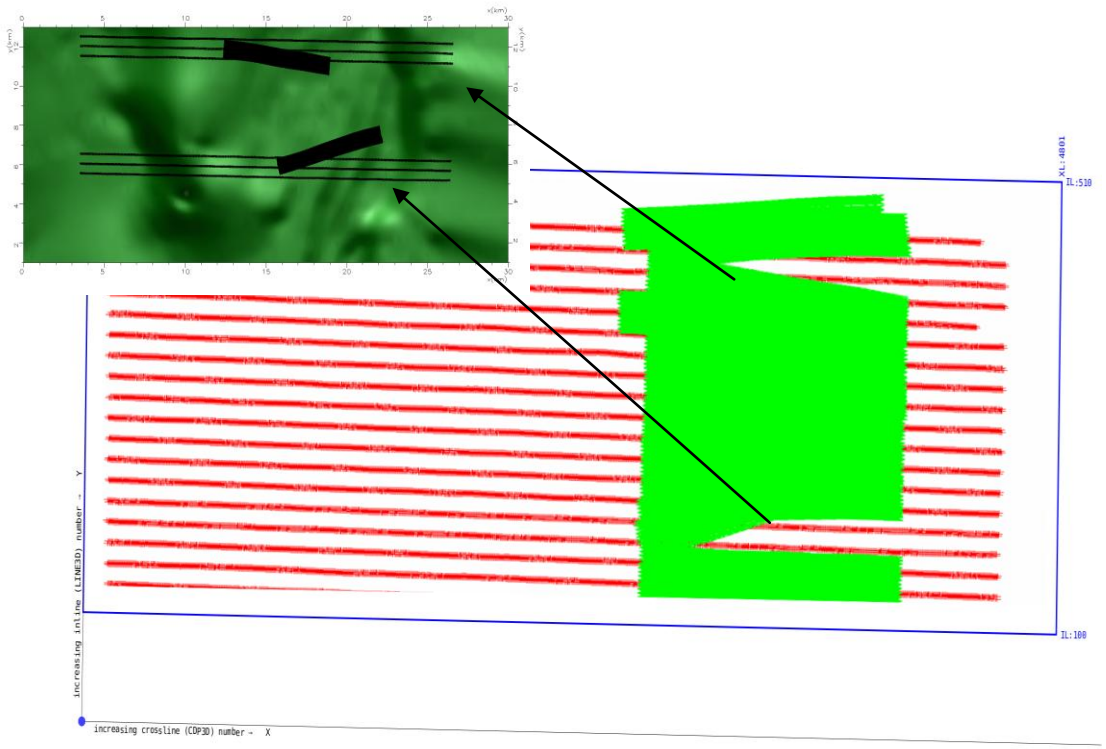

Figure 2.9 (a): Survey area used for the complex model and with the cable feathering highlighted in the sub-figure.

In this section, a more realistic subsurface model will be considered employing the same realistic acquisition geometry as before.

The complex model was generated in NORSAR3D and consisted of four horizons: waterbottom, FZBDeep, FZBComplex, and Deapflat ordered with increasing depth. In our simulations, the waterbottom represents the seafloor, the overburden is represented by the FZBDeep horizon followed by the target horizon FZBComplex and a deep horizontal layer located at 7km. The dimensions of the model are 30km

(inline) and 25km (crossline). The basic structure of the model is shown in Figure 2.9b.

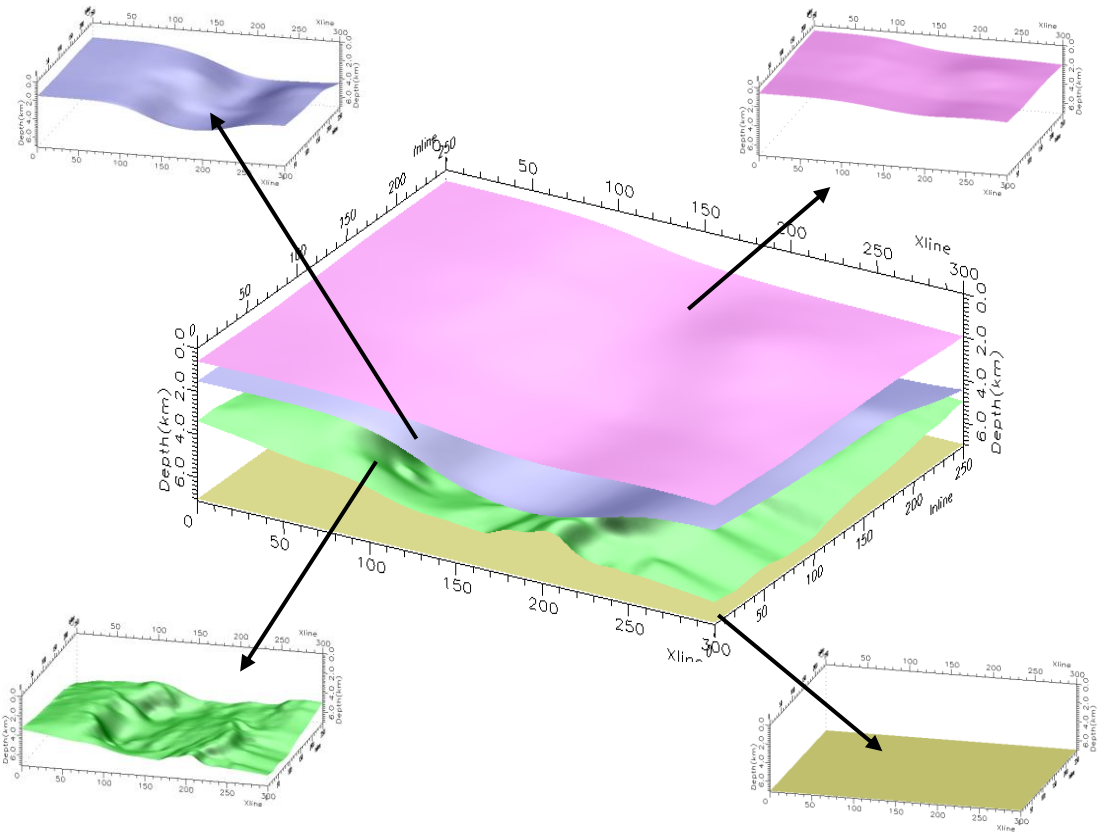

Figure 2.9 (b): Complex model with four horizons, waterbottom (pink), FZBDeep subsurface (blue), FZBComplex (green), and DeapFlat (brown)

A couple of navigation lines (P190 files) of a total of 18 P190 files were modified to adapt to the model. In Figure 2.9 (a), the blue frame indicates the survey grid file and the red and green lines represent respectively the navigation lines and streamers. The actual length of each navigation line is 120km in the inline direction which is far longer than our model. Therefore, some parts of the real geometry data were chopped to adapt well to the length of the model in the inline direction. In the inline direction, the CDP numbering runs from 1 to 4801 corresponding to 30km in length. In the crossline direction, we choose CDP line numbering from 100 to 510 which corresponds to a subset of approximate 10km in the crossline direction (out of 25km) (see Fig.2.9c). This area of selection covers some complex geological features associated with the FZBComplex subsurface. Therefore, it can serve as a test of the capability of the Fresnel zone binning to handle complex subsurfacs and possible decrease the percentage of infill management.

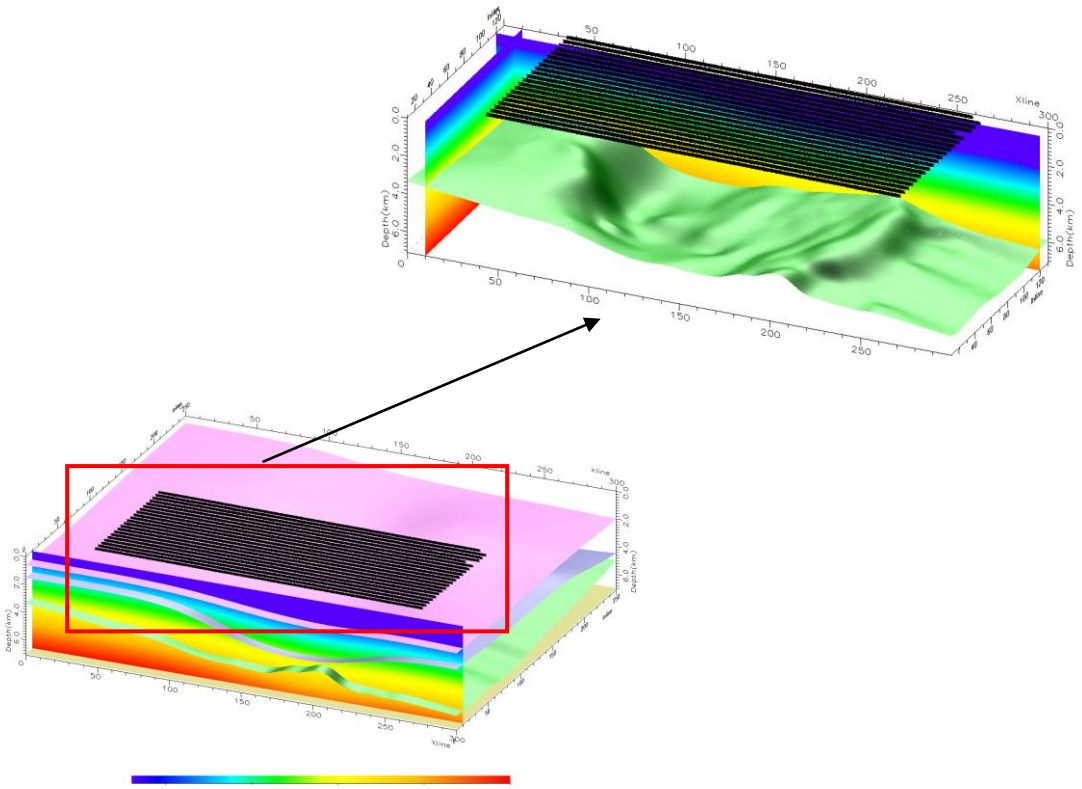

Figure 2.9 (c): The survey area covered by all 18 navigation lines (complex model)

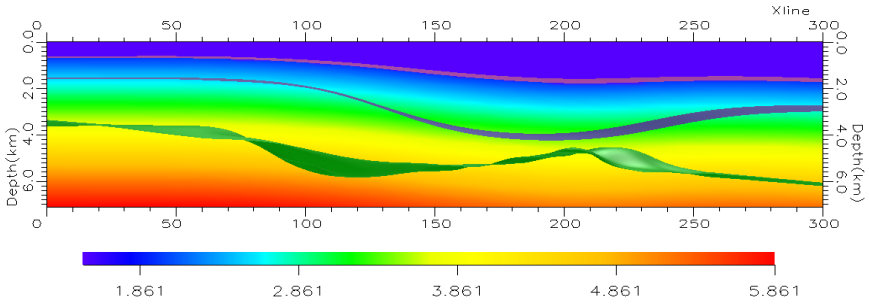

Figure 2.10: The P- velocity field employed in the complex model

The P-velocity model employed for the complex model is shown in Figure 2.10. A constant gradient model was assumed below the seafloor with the same initial velocity V_0 (2km/s) along the sea bottom:

$$V_z = V_0 + g(z - z_0) \tag{2.3}$$

Where g is the gradient (0.6 $m.s^{-1}m^{-1}$), z is depth, V_z is the velocity at depth z and z_0 is the depth of water.

The initial frequency of the seismic signal at the seafloor is set to 60 Hz and is gradually decreased with depth as given by the formula:

$$f_{(z)} = f_0 \frac{V_{average}}{V_0} \qquad (2.4)$$

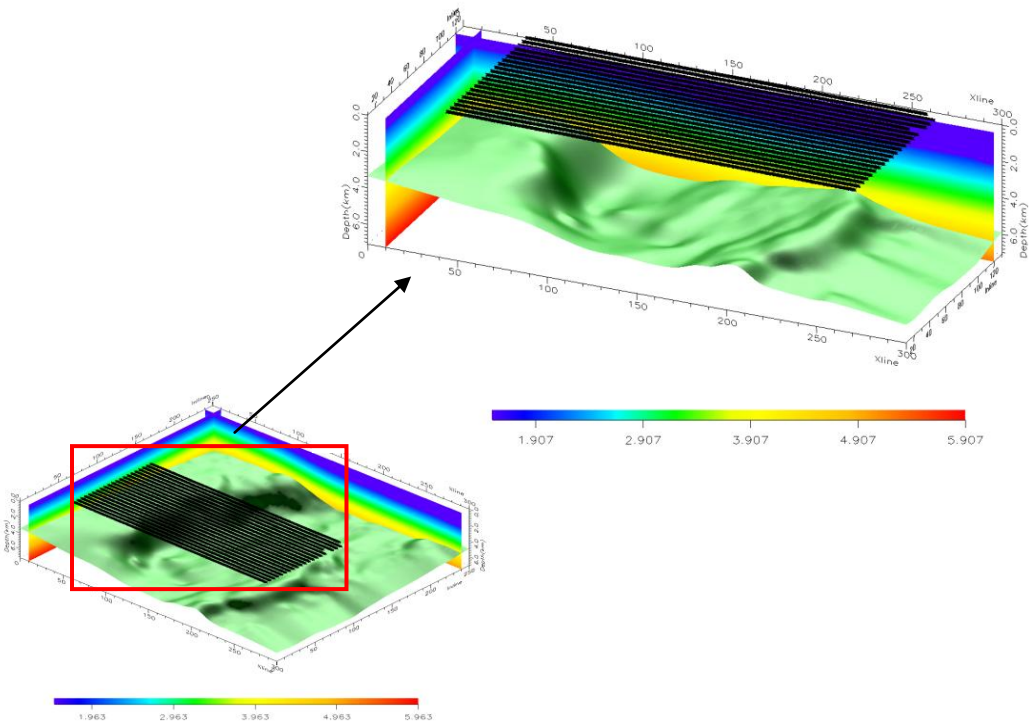

Figure 2.11: FZBComplex horizon (target horizon)

In the complex model, the FZBComplex horizon is chosen as the target horizon to test the Fresnel zone concept when applied to complex geological structures. The coverage on this target horizon at near, middle and far offsets are shown in Figure 2.12 (left). To the right in Figure 2.12, the corresponding Fresnel zones are shown for an average target depth. In case of near offset, the target surface is well covered by the Fresnel zone. The black color in the figure means 1 dB amplitude loss which is a reasonable and accepted decrease in subsurface imaging. At the middle and far offsets, there are two obvious areas where the amplitude losses are down more than 5 dB.

Since essentially the same acquisition geometry has been employed as in the simple model case, the reasons for these 'coverage holes' are again due to extreme feathering as discussed before.

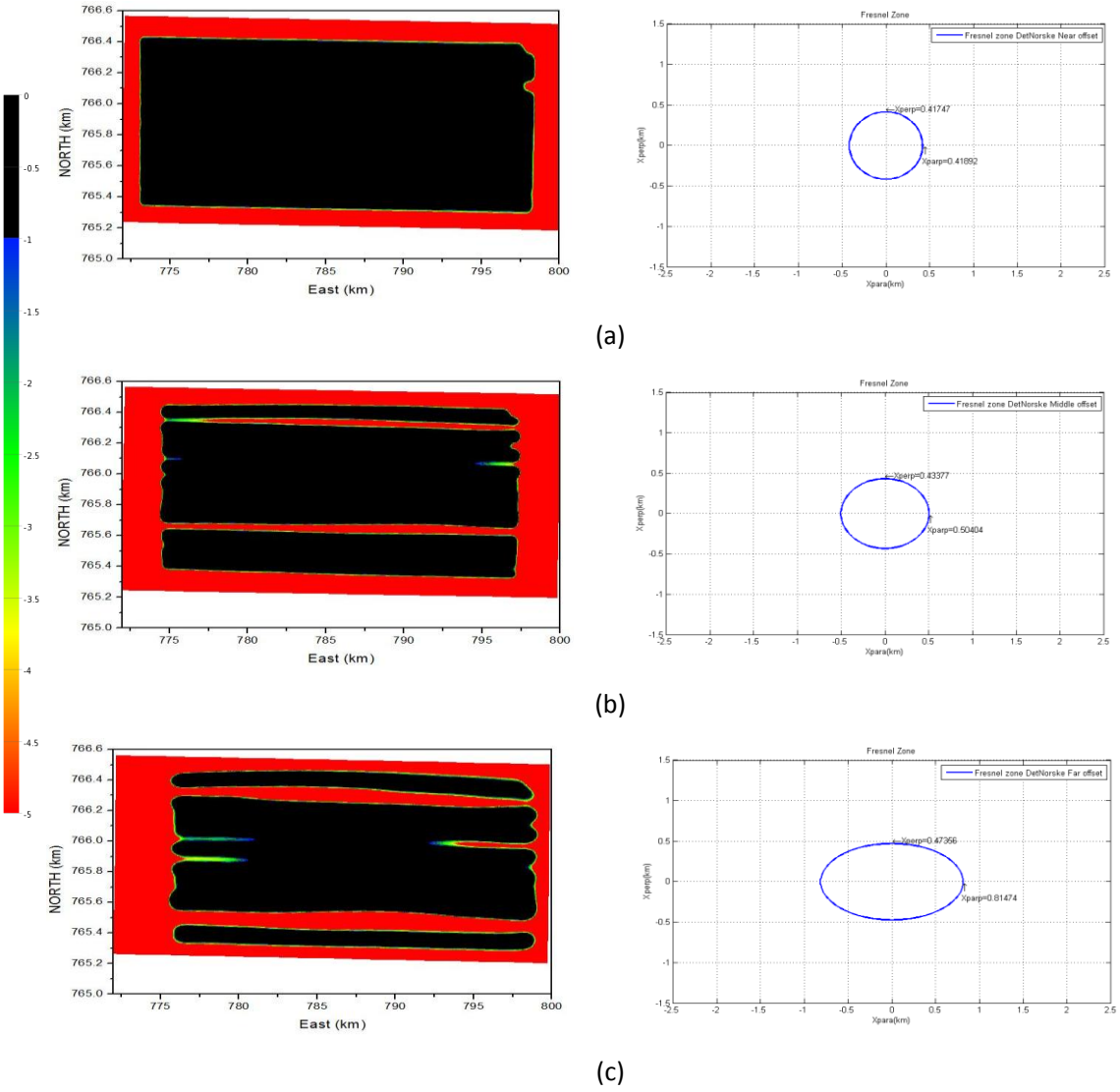

Figure 2.12: Coverage result for FZBComplex horizon (target horizon) at near (a), middle (b), and far offset (c) (left); The corresponding Fresnel zones are shown to the right.

2.3 Infill management

As shown in Figure 2.12, there are two obvious 'coverage holes' caused by the strong feathering in our survey. The basic aim of the Fresnel zone binning analysis is to decide which areas of the survey that need to be infilled by new survey lines. Based on the coverage of our target surface, three new survey lines were designed to infill two 'coverage holes' at middle and far offset. A sketch of all navigation lines including the three new infill lines is shown in Figure 2.13.

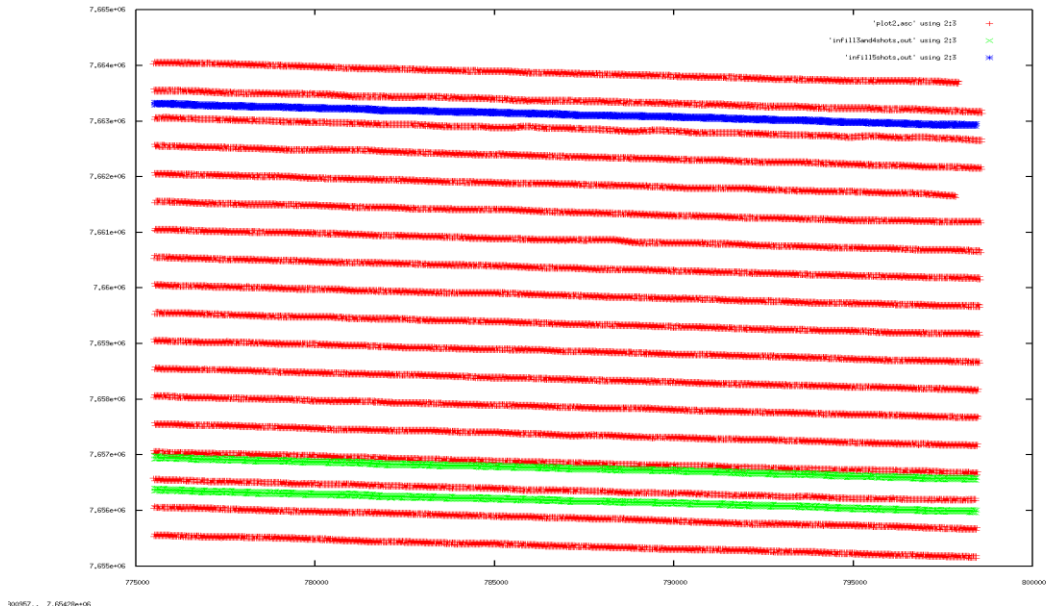

Figure 2.13: Survey plan after infill design: red lines (original survey lines); blue and green lines (infill survey lines)

The new coverage of the target subsurface after Fresnel zone binning is given in Figures 2.14 (a) and (b) (middle and far offsets). These results are to be compared with Figure 2.12.

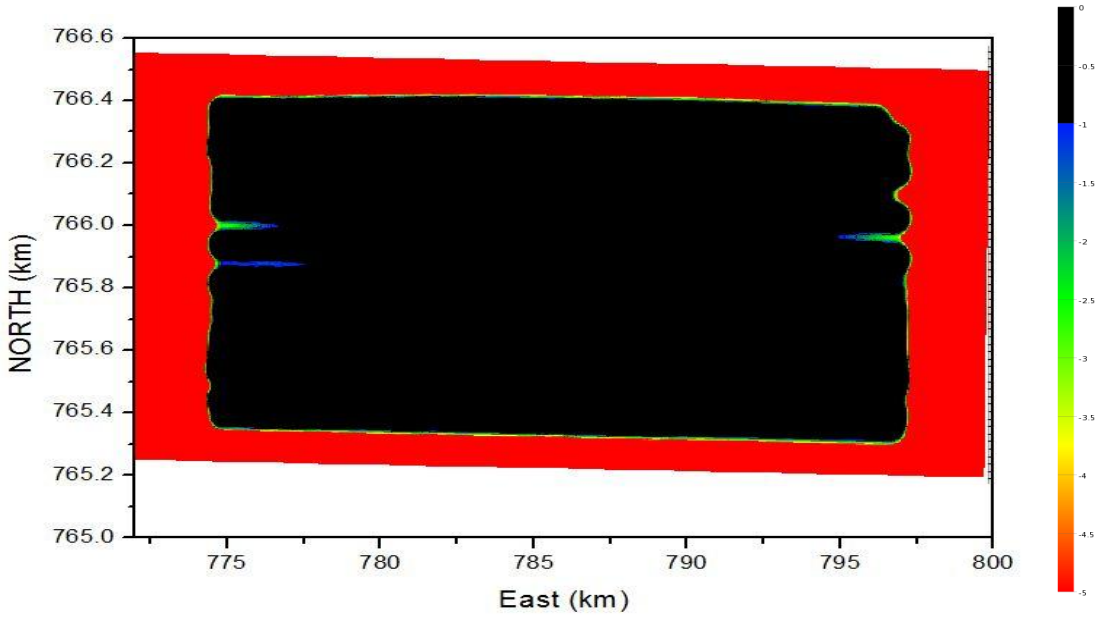

(a)

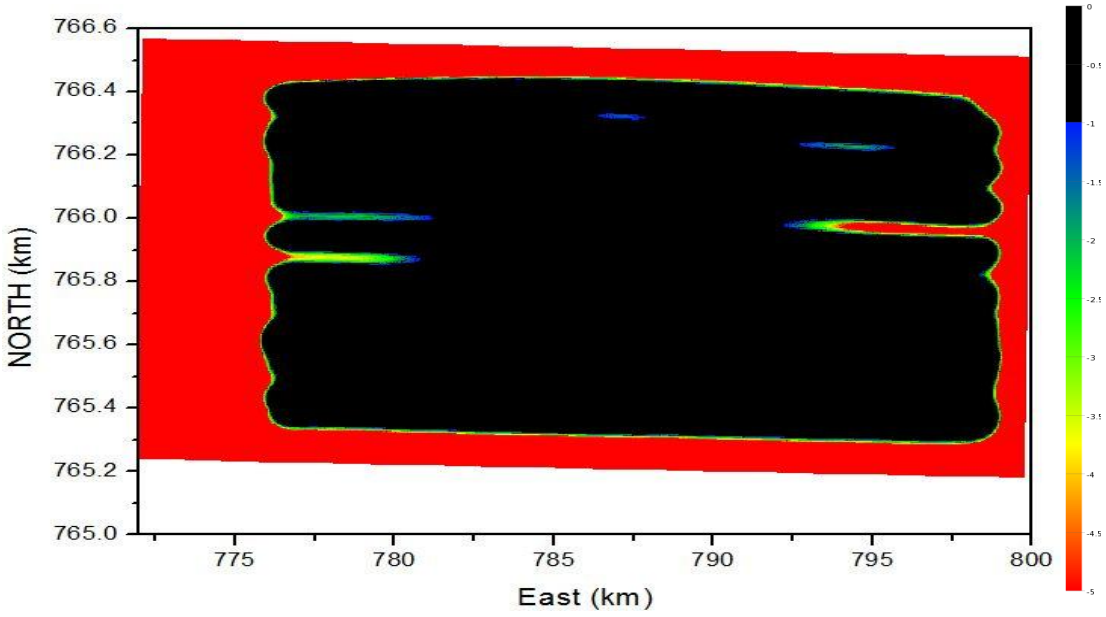

(b)

Figure 2.14: Coverage target surface at middle (a) and far (b) offset after infill management (1 dB amplitude criterion).

In Figures 2.14 (a) and (b), the acceptable amplitude losses are restricted down to 1dB at middle and far offset. The 'coverage hole' at both middle and far offsets are well filled based on Fresnel zone binning when compared with Figures 12 (b) and (c). Although some small 'coverage holes' still exist, most anomalies due to the strong feathering have been removed. If the amplitude criterion of acceptance is lowered to 2dB the results shown in Figures 2.15 (a) and (b) are obtained. As expected the Fresnel zone binning technique will improve the coverage even further.

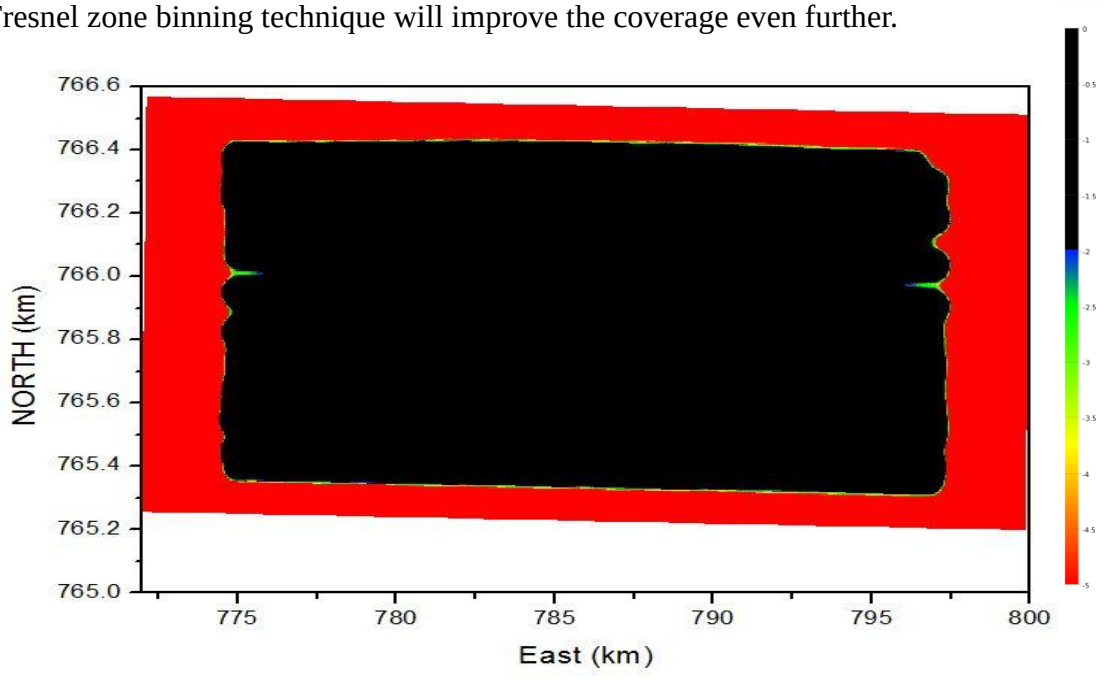

(a)

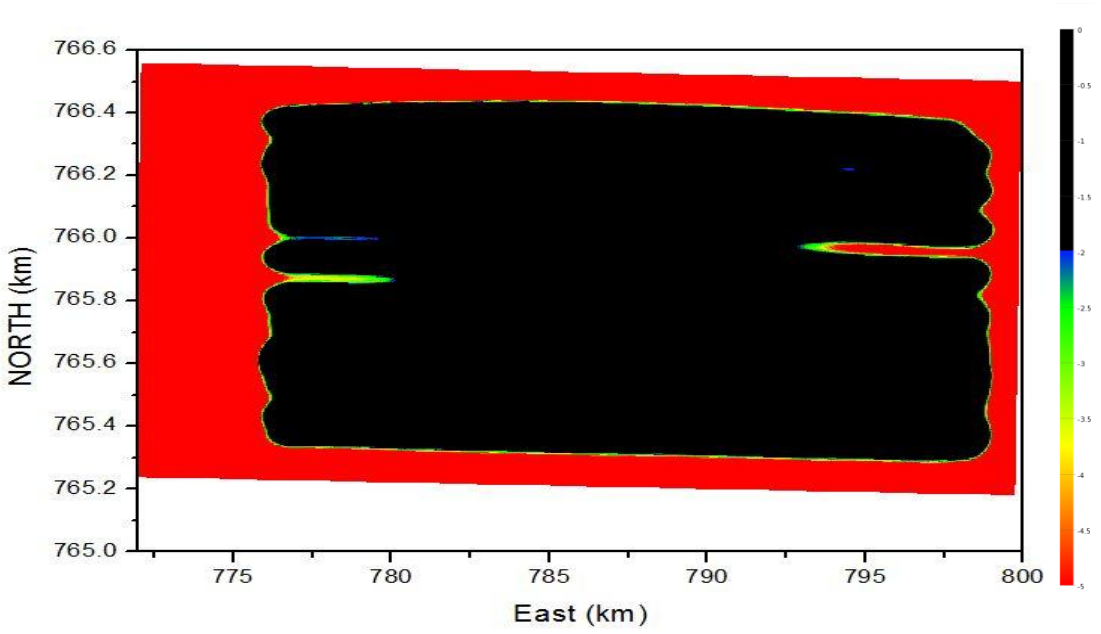

(b)

Figure 2.15: Coverage of target surface at middle (a) and far (b) offset after infill management (2dB amplitude criterion).

2.4 Quality Control of Fresnel zone binning theory (gradient model)

When applying a velocity-gradient model (as in the case just discussed), the velocity V_z at a given depth Z is given by:

$$V_z = V_0 + g(z - z_0) \tag{2.5}$$

Where the velocity V_0 represents the sediment velocity at the (possibly varying) seafloor (depth Z_0). Eq. (2.5) can be rewritten on the form:

$$V_z = (V_0 - gz_0) + gz \tag{2.6}$$

Or

$$V_z = V' + gz \tag{2.7}$$

Which clearly shows that the same velocity gradient g is assumed for the water layer. This is certainly an approximation. To evaluate the accuracy of this simplification the two cases shown in Figure 2.13 were considered:

1: calculate travel time with V_z using Eq.(2.6)

2: calculate travel time employing curved ray in the subsurface and no gradient in water.

Based on the differences in travel times between these two cases, the validity of Eq.

2.5 can be found.

The calculations tried to resemble the complex model in section 2.3 as close as possible. The average velocity in the water was set to 1.5km/s, the sediment velocity V_0=2.0 km/s and the gradient g to 0.6 s^{-1}. Since in the complex model, there are no flat horizons, average depths down to each surface were employed instead.

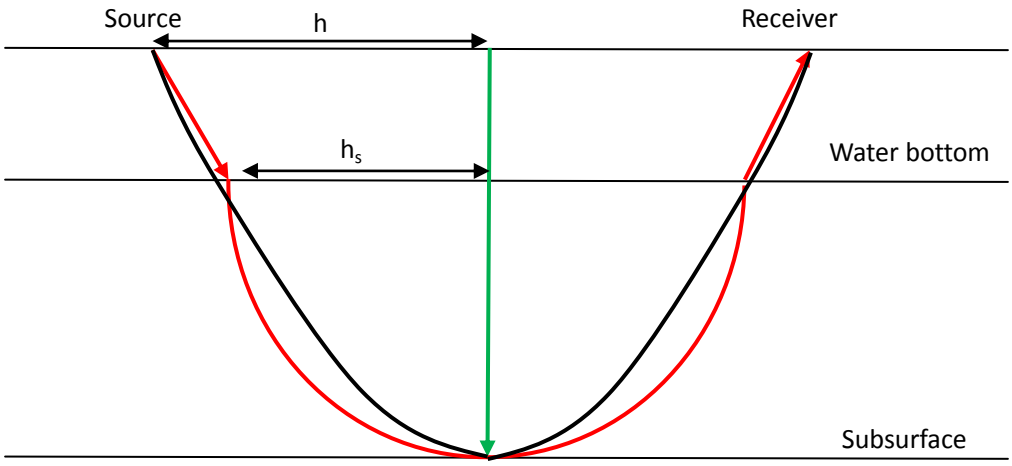

Figure 2.13: Travel paths for the two cases: black line (case 1); red line (case 2); The zero offset case is given by the green line.

In case 1, only curved rays exist. In case 2, the rays follow straight lines in the water and then curves in the subsurface because of the velocity gradient.

In case 1, the one way travel time is calculated by the formula (Monk, 2010):

$$T_1 = \left(\frac{1}{g}\right)\cosh^{-1}\left[1 + \frac{g^2(h^2 + z^2)}{2V_0(V_0 + gz)}\right] \tag{2.8}$$

Where h is the half offset between source and offset, g is velocity gradient; z is the depth of target horizon and $V_0 = V'$ in Eq.2.7.

In case 2, the total one-way travel time is divided into two parts, e.g water and subsurface.

$$T_2 = T_{water} + T_s \tag{2.9}$$

In the water, the travel time is given by explicitly as:

$$T_{water} = \frac{\sqrt{(h - h_s)^2 + d^2}}{1.5} \tag{2.10}$$

Where h_s is the distance from the middle point between source and receiver to the refraction point along the water bottom; d is the depth of water. The travel time T_s is:

$$T_s = \left(\frac{1}{g}\right)\cosh^{-1}\left[1 + \frac{g^2\left({h_s}^2 + (z-d)^2\right)}{2V_0\left(V_0 + g(z-d)\right)}\right] \qquad (2.11)$$

From Eq.2.9, 2.10 and 2.11, an explicit expression for h_s can be found employing Fermat's principle. In practice it was solved numerically, e.g. we solve for $\frac{dT_2}{dh_s} = 0$.

Employing these formulas, the one way travel time for each of the two cases are calculated and listed in Table 2.5:

Table 2.5: One-way travel time for the two cases (the average depth of water is set to 1.2km)

	Average depth (km)	T_1 (s)	T_2 (s)	$T_1 - T_2$(s)	$\frac{T_1-T_2}{T_2}$(%)
Near offset	2.8	1.403	1.461	0.058	4.0
	5.0	2.014	2.071	0.057	2.8
	7.0	2.425	2.481	0.056	2.3
Middle offset	2.8	1.640	1.702	0.062	3.6
	5.0	2.122	2.180	0.058	2.7
	7.0	2.490	2.547	0.057	2.2
Far offset	2.8	2.120	2.188	0.068	3.1
	5.0	2.378	2.438	0.060	2.5
	7.0	2.651	2.709	0.058	2.1

From Table 2.5 it follows that the relative errors range between 2.1% and 4.0%. These errors are reasonable and indicate that the gradient-velocity model assumed in Fresnel zone binning analysis is fair.

Up to now, the concept of Fresnel zone binning analysis has been introduced by considering two different subsurface models and a real acquisition geometry. Using simple formulas describing the Fresnel zone, the coverage of a given target reflector can be analyzed by adding together all Fresnel zones associated with the given acquisition layout along the horizon considered. By introducing a simple amplitude criterion, the quality of the coverage can be judged.

However, before being able to quality control the output from the Fresnel zone binning analysis, the actual seismic data must also be taken into account. In the next chapter, controlled data will be generated in the complex model employing dynamic ray tracing and the same real navigation data. Based on illumination maps using the actual controlled data, the potential of the Fresnel zone binning concept can be further analyzed.

Chapter 3: Controlled data

By introducing the seismic waves, various forms of illumination maps can be introduced and employed to further benchmark the Fresnel zone binning technique.

3.1 Ray tracing in complex model

The NORSAR3D is employed to generate seismic data based on dynamic ray tracing. The complex model introduced in Chapter 2 was input to NORSAR3D together with all navigation lines. However, the actual model was slightly changed to ensure reflected seismic waves from each of the layers:

Modification 1: artificially add a velocity jump at the interface between two geological layers.

Modification 2: the gradient in the different geological layers will not be the same. The condition is that velocities along each interface are preserved.

After the modifications, the actual ray paths in the new model will not completely resemble those in the original model built up in Chapter 2. Furthermore, the size and location of the Fresnel zones are also not fully consistent with the ones calculated in Chapter 2 because of differences in ray paths and travel times. However, the discrepancies are assumed small, especially in size of Fresnel zone binning (less than several tens of meters).

The typical ray tracing model and velocity fields for the new model are shown in Figure 3.1. Figure 3.2 shows a plot of the global P-velocity field as well as an indication of the velocity jumps associated with the interfaces.

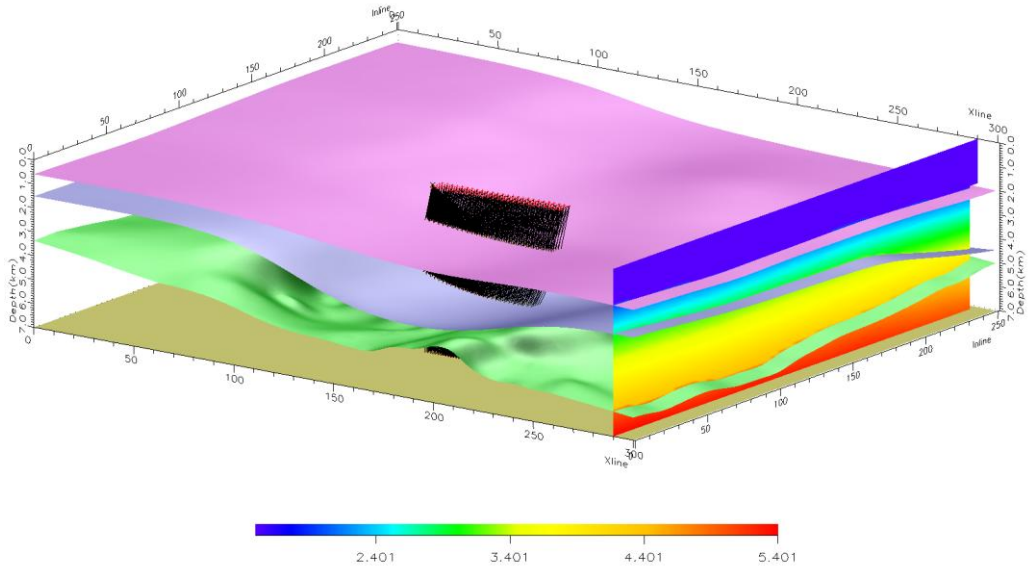

Figure 3.1: Example of typical dynamic ray tracing in the NORSAR3D velocity model

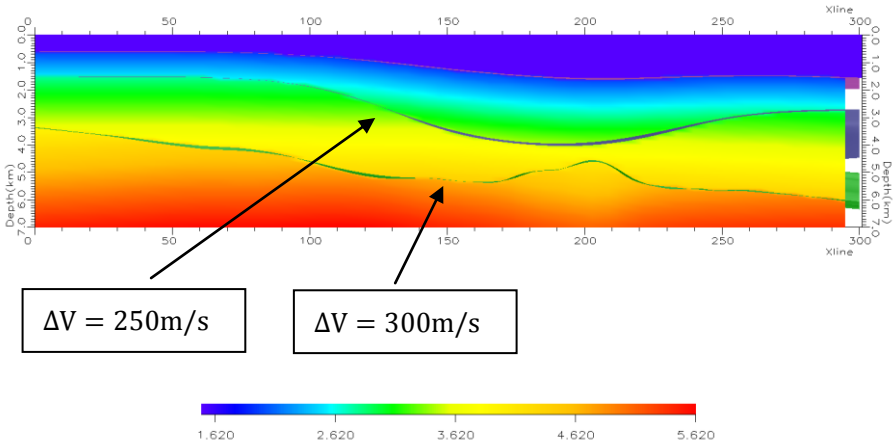

Figure 3.2: The velocity field and the variation of velocity across the interface between two geological layers.

The simulation of controlled data corresponding to the survey including the actual feathering as described in Chapter 2, was carried out both before and after infill management. In addition, a new survey was constructed of 18 navigation lines covering the same survey area but with no feathering. Hence, this latter survey represents the ideal case and can serve as a reference.

3.2 Illumination map

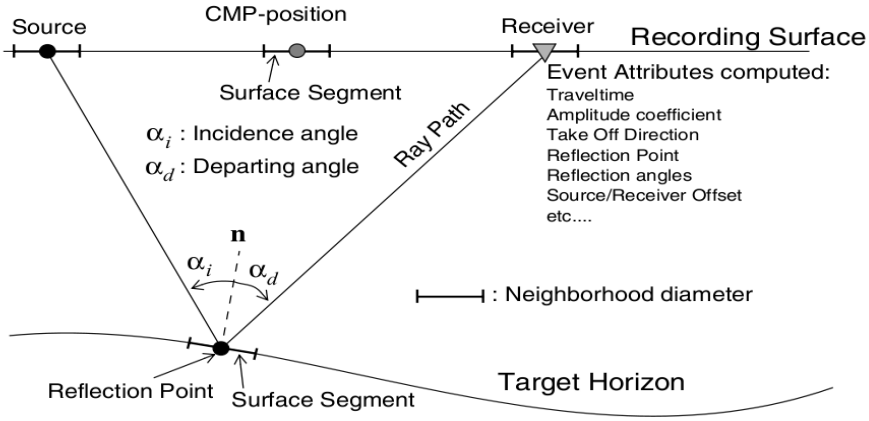

Figure 3.3: Possible event attributes in NORSAR3D (NORSAR3D UserGuide)

As indicated in Fig.3.3, several event attributes can be provided by NORSAR3D. Such maps can give the actual coverage of the seismic waves in a quantitative manner, such as hit map, hit density map and SMA (simulation migration amplitude). In my thesis, the hit map is used to quantify the number of reflections within each bin-cell associated with a horizon, where the bin-cell is from the event position. The bin-cells in the hit map are built up employing the Nominal bin-cell option in NORSAR3D.

Figures 3.4 (a)-(c) show hit maps of the target horizon (FZBComplex) at near, middle and far offsets. Comparison of the hit maps before and after infill management (left and right column in Fig 3.4) shows that the two big 'coverage holes' in our survey are now filled, especially at middle offsets. Figure 3.5 (main figure) shows the hit map after infill management (far offset), where several residual 'coverage holes' still exist. By introducing Fresnel zone binning (cf. Fig 2.14), most of these artifacts are restored and the overall coverage is significantly improved (upper right in Fig.3.5).

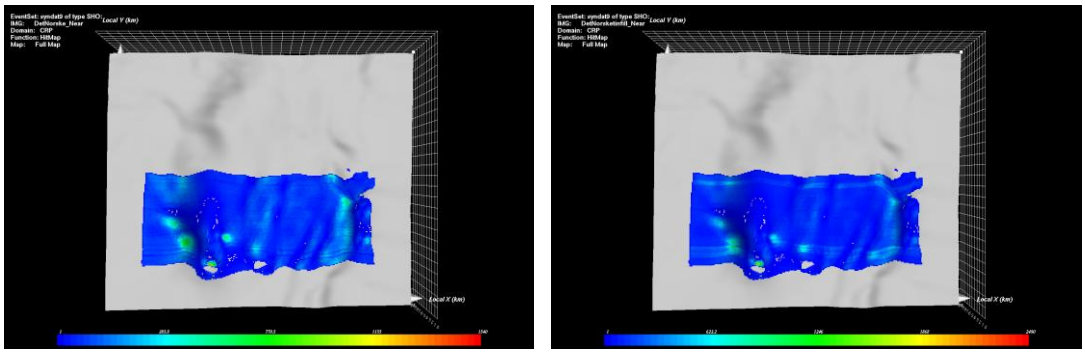

(a)

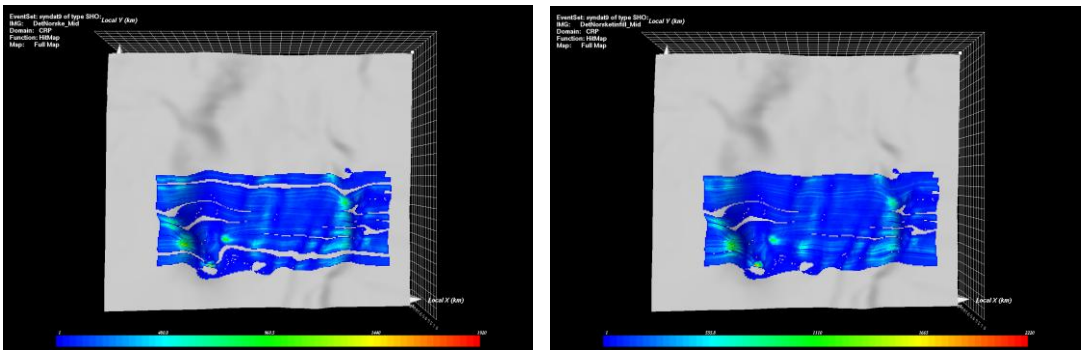

(b)

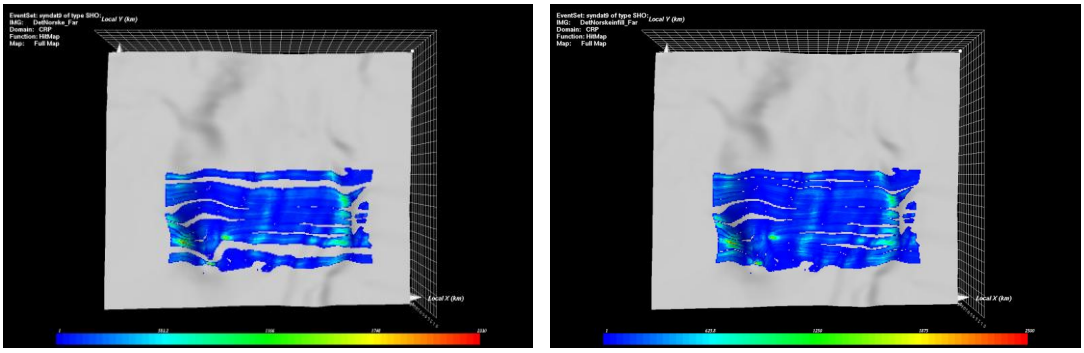

(c)

Figure 3.4: Hit maps at the target surface at near (a), middle (b), far (c) offsets. Hit maps before infill management in the left column; hit maps after infill management based on Fresnel zone binning analysis to the right.

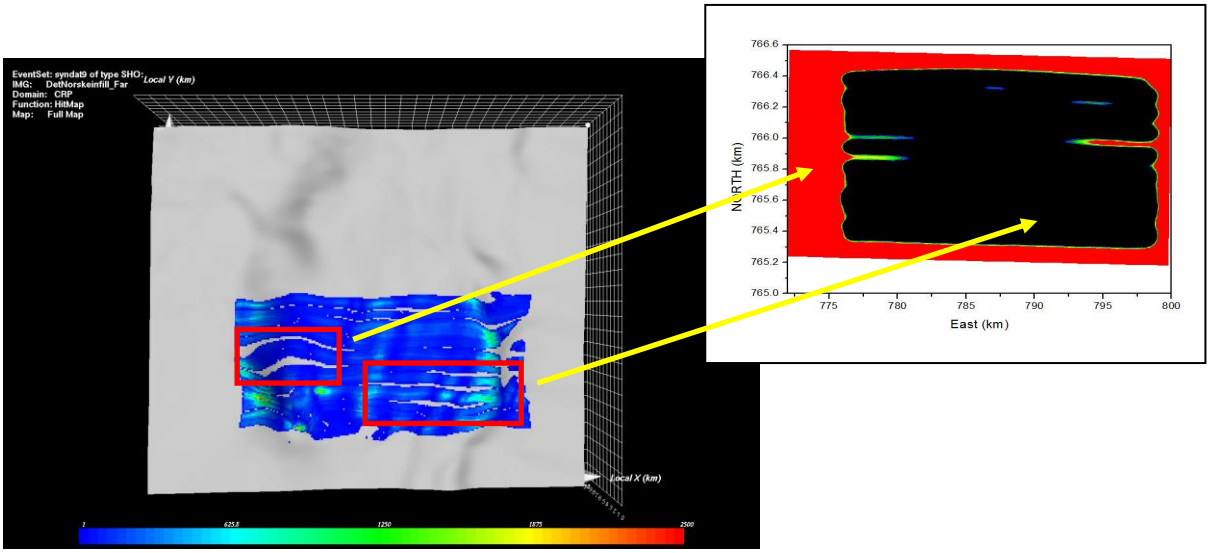

Figure 3.5: Many residual 'coverage holes' in the coverage map (main figure) are restored after Fresnel zone binning (upper right).

3.3 Fresnel zone binning analysis in NORSAR3D

It has been demonstrated how Fresnel zone binning analysis can be employed to design infill management. Moreover, by generating controlled data and associated hit maps, the potential of Fresnel zone binning to improve the coverage without reshooting has been discussed. However, up to now, the Fresnel zone calculations have been carried out employing simplified formulas (Monk 2010). In this section, the actual Fresnel zones calculated from ray tracing will be compared with these simplified expressions.

3.3.1 Constant velocity (model A)

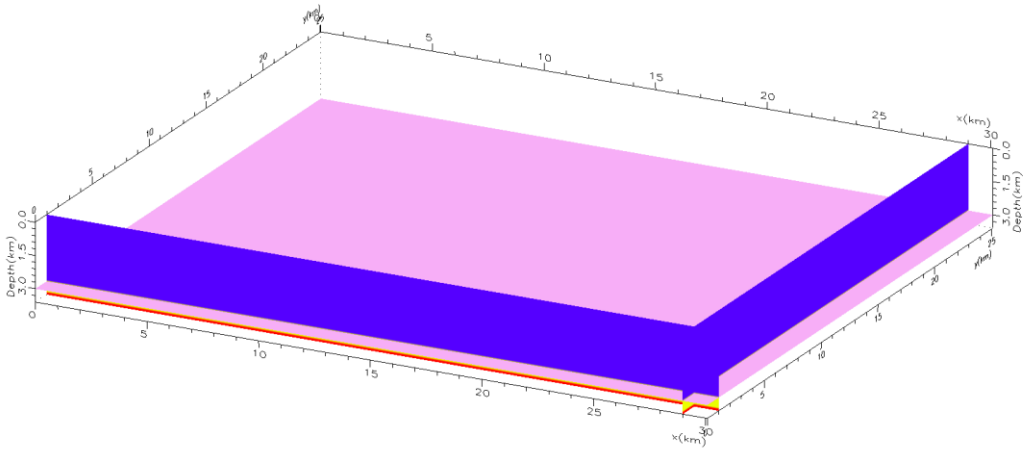

Figure 3.6: Constant velocity model

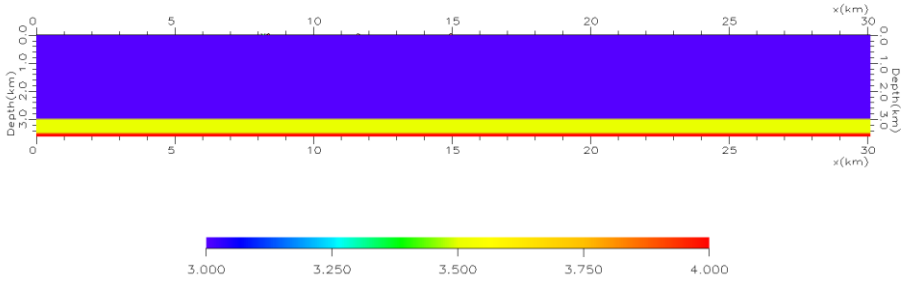

Figure 3.7: Constant velocity field in model A

Figures 3.6 and 3.7 show the simple model including one horizontal target layer at a depth of 3km. The interval velocity is 3km/s. One shot-receiver pair from one of the navigation lines was selected. In the actual calculations the following definition of the first Fresnel zone was employed: the area defined by rays which travel time differences are no more than a half-period when compared with the specular one.

First, the spatial coordinate of the specular point and its associated travel time (T_1) at respectively near, middle and far offset are calculated (e.g. Fig 3.8 left). Secondly, a square matrix consisting of one million non-specular points (1000 by 1000 grid points in respectively X and Y directions) was constructed around the corresponding specular point. Then the travel times (T_2) from the shot to those grid points are calculated. The interval distance between two neighboring grid points in the subsurface was 2 meters. Thirdly, a shot was fixed at the location of the true surface 'receiver' and the travel times (T_3) from this shot to the same grid points in the subsurface were calculated (e.g. Fig 3.8 right). After those three steps, the difference in travel time could be calculated. If the absolute value of this difference was less or equal to the half-period, this non-specular point was stored. The Fresnel zone for a given offset was then defined by all such non-specular points.

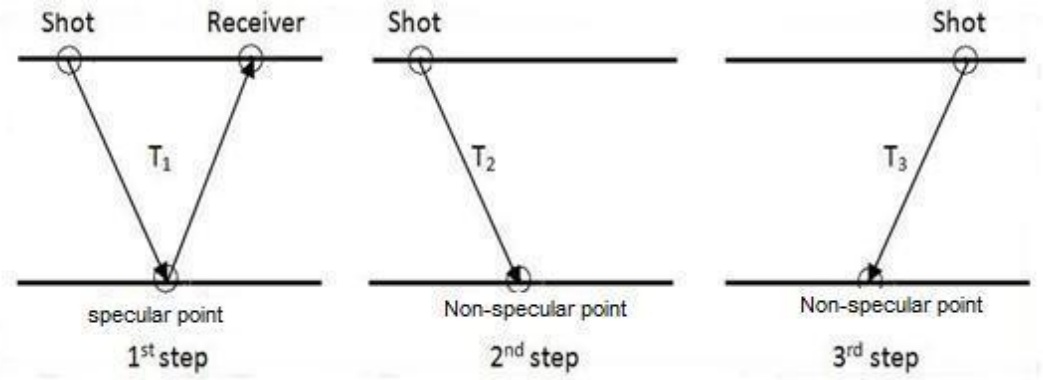

Figure 3.8: Calculation of specular and non-specular rays.

Table 3.1 shows the size of the Fresnel zones obtained from both ray tracing and the theoretical formulas. Both the inline (X) and crossline (Y) dimension is given. As expected, the difference for this ideal case of constant velocity and flat horizon are

negligible (only caused by numerical errors).

Table 3.1: The size of the Fresnel zones calculated from ray tracing and from theoretical formula

	Near offset		Middle offset		Far offset	
	X (m)	Y(m)	X(m)	Y(m)	X(m)	Y(m)
Fzb (theory)	676	672	834	722	1234	822
Fzb(T/2 experiment)	668	670	824	720	1218	820

Figure 3.9 (a)-(c), visualize the results obtained in Table 3.1 with red curve representing the theoretical Fresnel zone and the black area the result from ray tracing.

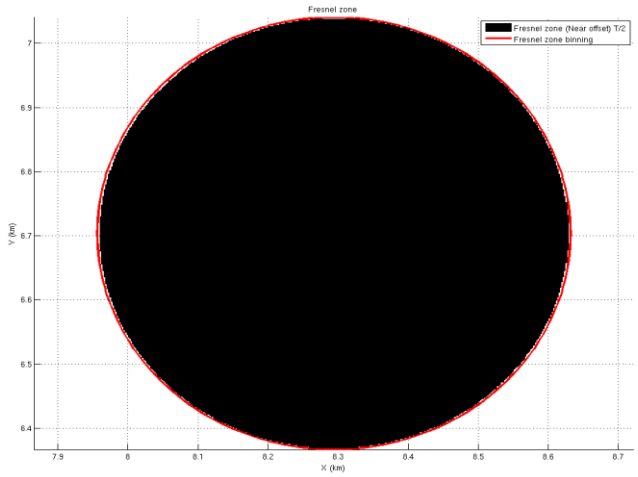

(a)

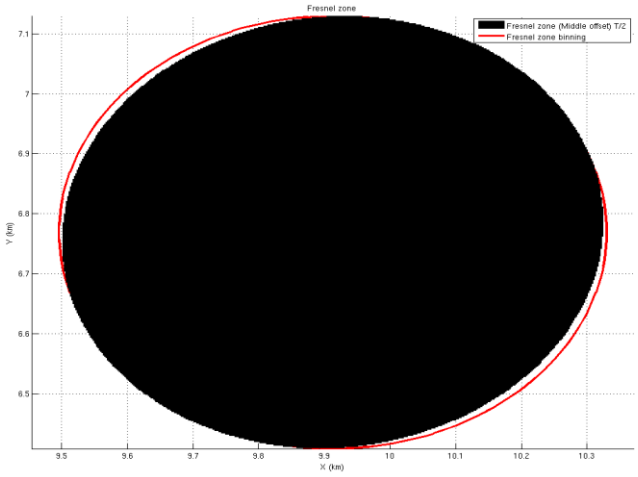

(b)

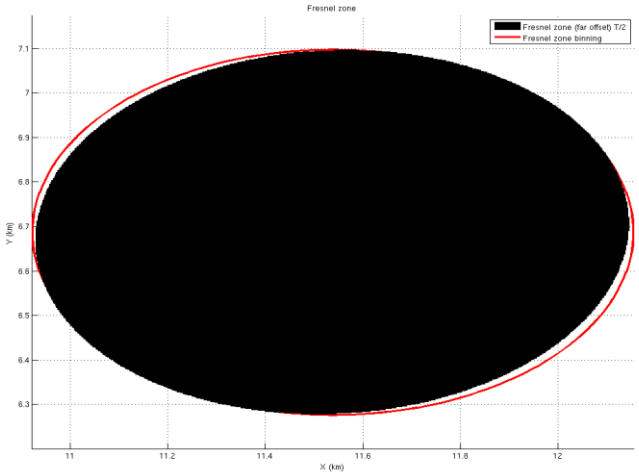

(c)

Figure 3.9 (a)-(c): Fresnel zones; Red curves represent theoretical formulas calculated for near, middle and far offsets.

In our simulation, 528 receivers were assumed along the cable with a receiver interval of 12.5m. In the calculations, receiver number 1, 260 and 520 were chosen corresponding to a half-offset of respectively 248m, 1740m and 3358m. The depth down to the target surface is 3km giving the following incident angles at these offsets: 5, 30 and 48 degrees. In Monk's article (2010), it is suggested that the theoretical formulas are accurate up to at least 45 degrees, which seems to be verified by our simulations.

3.3.2 Gradient velocity (model B)

In this section the same type of calculations are carried out again, but this time introducing a gradient-velocity model above the horizontal target layer. (cf. Figs. 3.10 and 3.11)

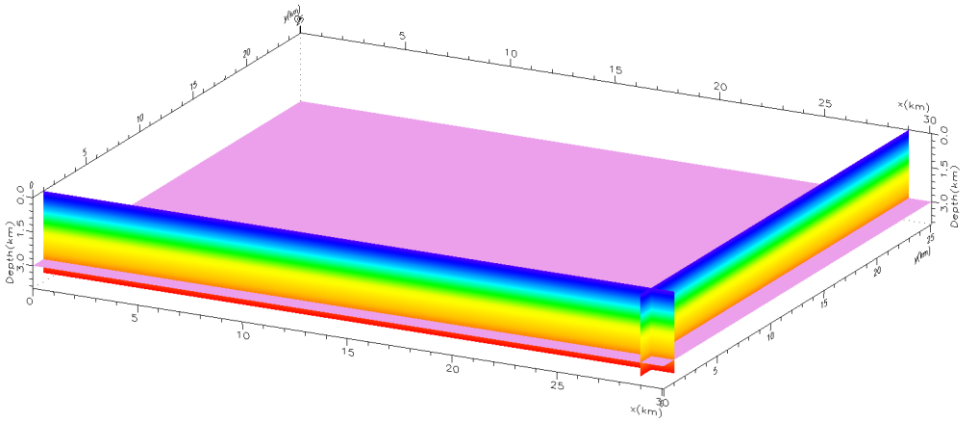

Figure 3.10 Model with gradient velocity

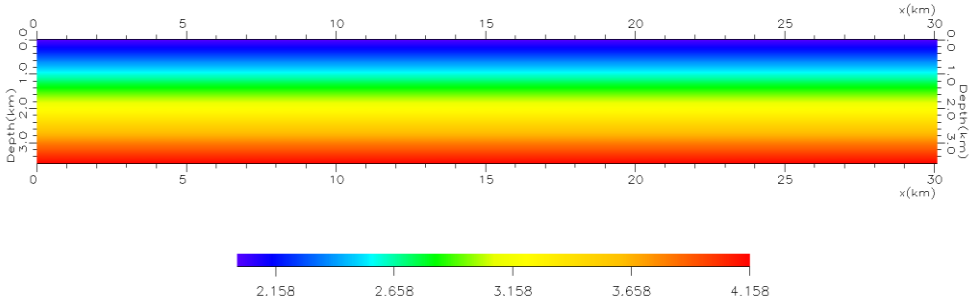

Figure 3.11 The velocity field in model B

The initial velocity V_0 is 2km/s, the velocity gradient g is 0.6 s^{-1}, and the depth of the target surface is also 3 km as before. The same receiver numbers are selected to represent respectively the near, middle, and far offsets. The dimensions of the Fresnel zones from ray tracing and theoretical calculations are presented in Table 3.2.

Table 3.2: Size of the Fresnel zones calculated using ray tracing (experiment) and theoretical formulas.

	Near offset		Middle offset		Far offset	
	X (m)	Y(m)	X(m)	Y(m)	X(m)	Y(m)
Fzb (theory)	646	640	908	692	2092	804
Fzb(T/2 experiment)	628	628	804	688	1366	804

Figures 3.12 (a)-(c) visualize the results obtained in Table 3.2. Again the red curves represent theoretical results and black areas represent results from ray tracing.

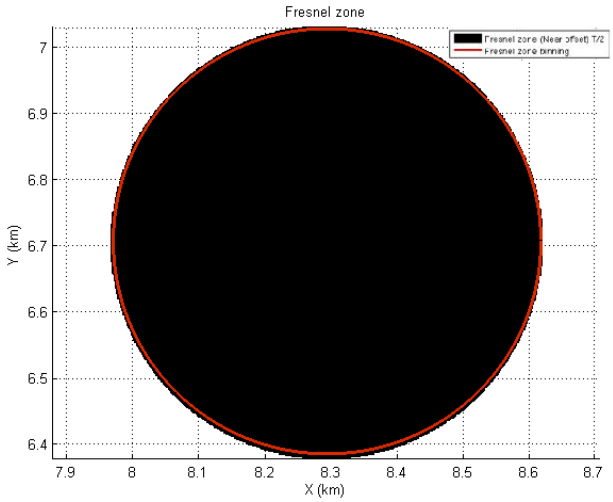

(a)

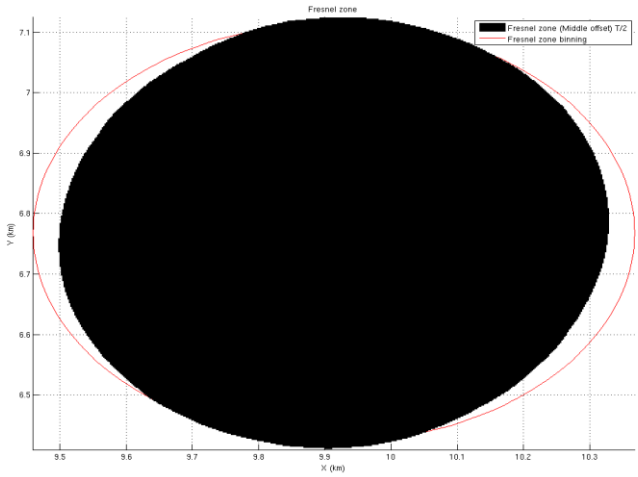

(b)

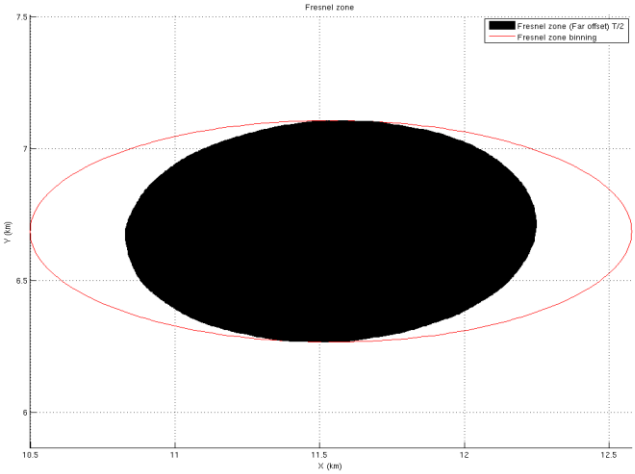

(c)

Figure 3.12 (a)-(c): Fresnel zone calculations employing ray tracing and theoretical formulas

Based on the results in Table 3.2 and Figure 3.12, the following observations can be made:

a. at near offset, the match between ray tracing and theoretical formulas is good.

b. at intermediate and especially large offsets, the theory of Monk predicts a significantly larger inline width of the Fresnel zone.

However, the crossline width is still in good match. This width is also the most useful one when it comes to binning. Table 3.3 provides a more systematic analysis in terms of angle of incidence.

To further analyze at which angle (offset) the gradient velocity formulas break down every 20^{th} of the total number of 528 receivers was analyzed. In Table 3.3, incident angle, half offset and size of Fresnel zone both from simulations and the theoretical calculations are listed.

Table 3.3: Incident angle, half offset and size of Fresnel zone from ray tracing and theoretical calculation.

Receiver no.	Incident Angle(degree)	Half Offset (m)	Simulation		Theory	
			Inline	Crossline	Inline	Crossline
1	6	249	628	628	644	640
20	8	318	632	632	646	640
40	10	416	636	634	652	642
60	13	526	644	640	661	644
80	16	641	656	646	672	646
100	18	759	672	652	686	650
120	21	879	678	652	702	654
140	24	1001	686	652	721	658
160	27	1123	694	652	744	662
180	30	1246	710	656	770	668
200	32	1369	734	666	798	672
220	35	1492	762	680	830	678
240	38	1616	786	688	868	686
260	40	1740	804	688	908	692
280	43	1864	826	692	952	700
300	45	1988	862	704	1000	706
320	47	2112	898	716	1056	714
340	50	2236	926	722	1118	722
360	52	2361	958	728	1184	730
380	54	2485	1000	736	1264	740
400	56	2610	1048	752	1342	748
420	58	2734	1088	756	1434	758
440	60	2859	1134	764	1538	766
460	62	2984	1188	776	1652	776
480	64	3108	1246	788	1780	786
500	65	3233	1300	796	1926	794
520	67	3358	1366	804	2092	804

Figure 3.13 (a) shows a plot of the crossline width of the Fresnel zone as a function of half-offset computed from ray tracing and theoretical formula. Figure 3.13 (b) shows the same quantities but as a function of incident angle. From both figures it follows that the crossline widths are well correlated between the two techniques.

However, in case of the inline width of the Fresnel zone larger differences were observed as shown in Figure 3.14 (a) and (b). In Monk's paper (2010), the inline width was approximated from the crossline width using the formula:

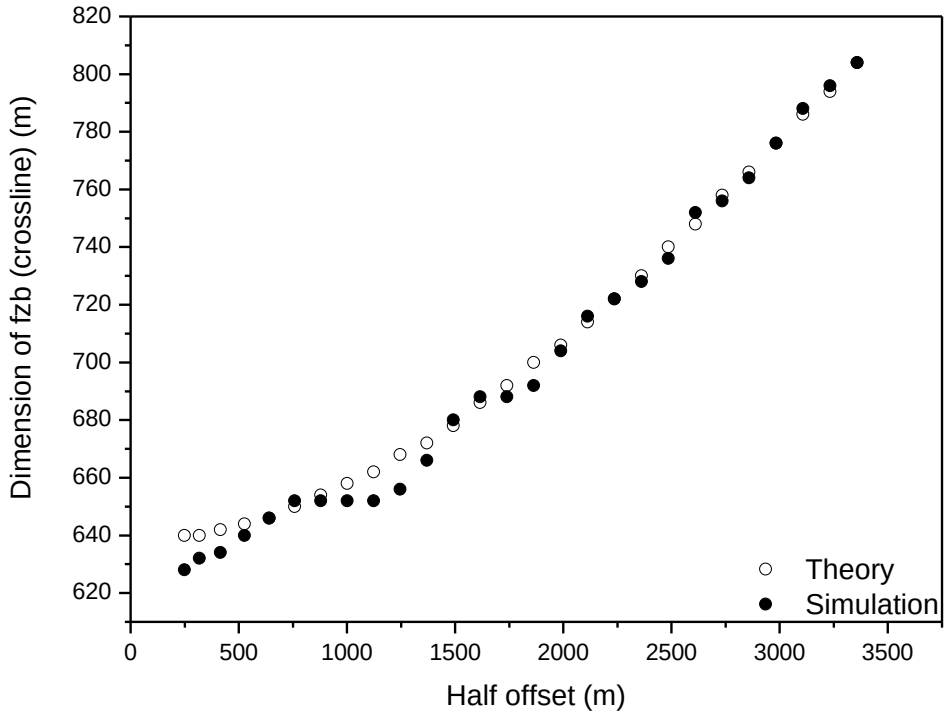

(a)

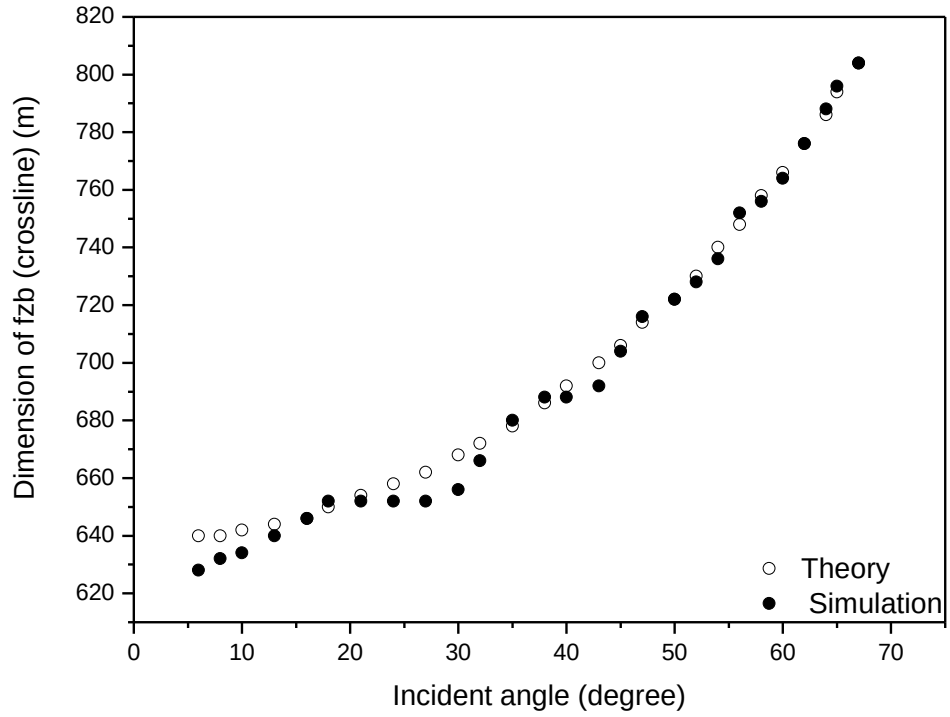

(b)

Figure 3.13 Width of Fresnel zone in crossline direction with offset (a) and incident angle (b)

$$X_F = \frac{Y_F}{\cos(\theta)} \tag{3.1}$$

Where θ is the incident angle and determined from the formula:

$$\sin(\theta) = p(V_0 + gz) \tag{3.2}$$

And p is the ray parameter which can be expressed by

$$p = \frac{2h}{\sqrt{(g^2(h^2 + z^2)^2 + 4V_0(V_0 + gz)(h^2 + z^2)}} \tag{3.3}$$

Where h is half-offset, z is depth of target surface, g is velocity gradient and V_0 is initial velocity.

In his paper, Monk states that in case of a homogenous velocity model, the approximation given by E.q (3.1) is valid up to about 45 degrees except for very shallow reflectors. From the analysis carried out here, it seems that in case of a velocity-gradient model, this approximation is worse. Based on the result obtained in Figure 3.14 (b), the limiting angle is now close to 27 degrees (the errors are then 50 meters in inline direction).

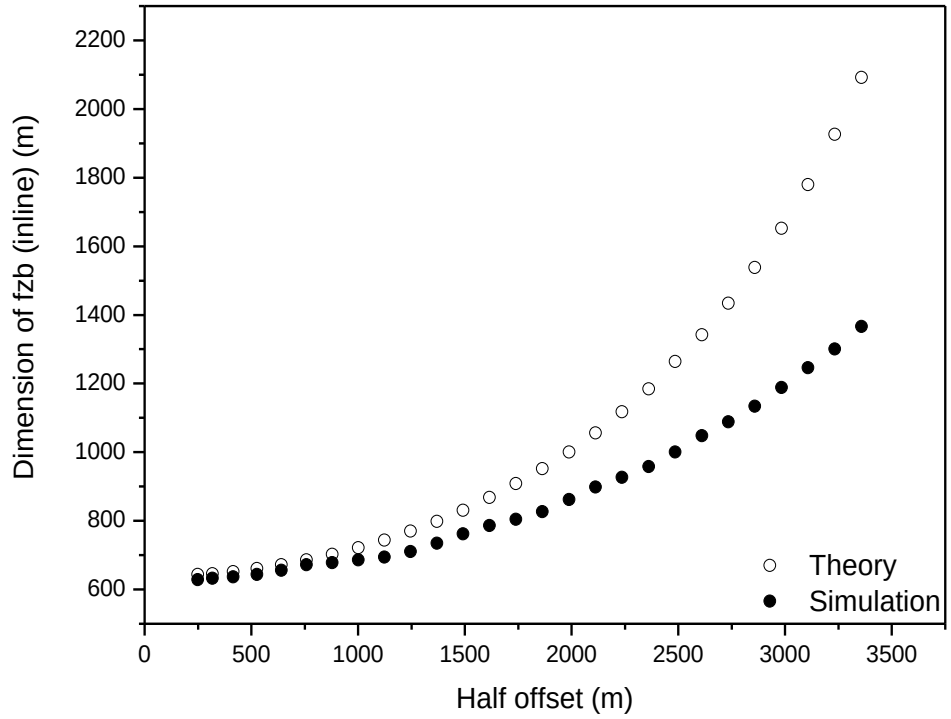

(a)

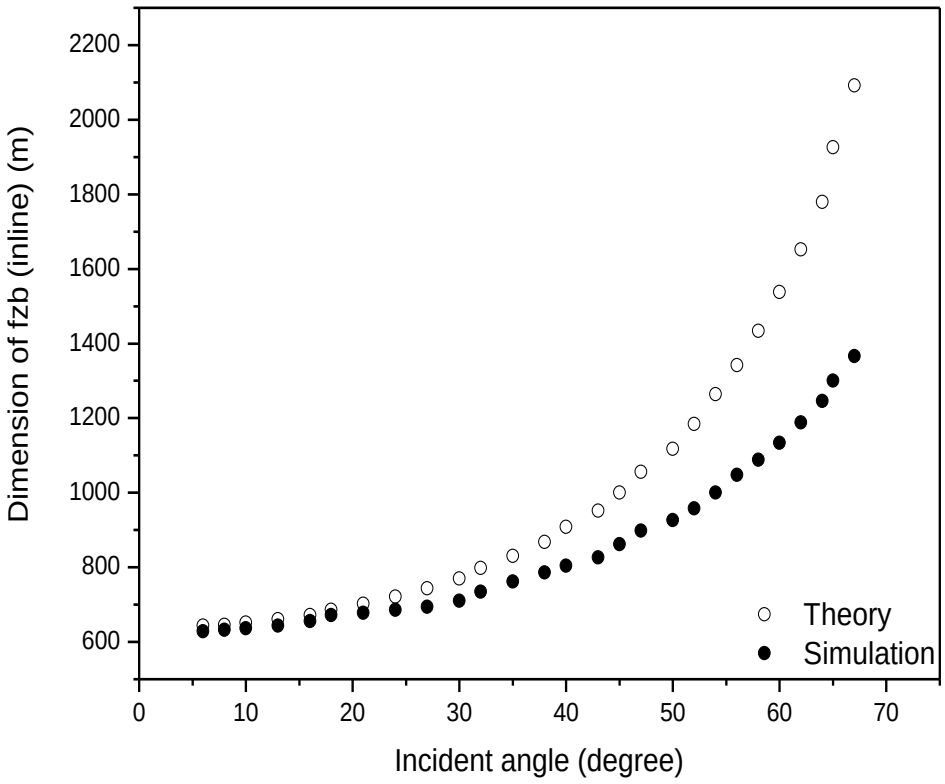

(b)

Figure 3.14: Width of Fresnel zone in inline direction with offset (a) and incident angle (b).

The dimensions of the Fresnel zone associated with a flat horizon have already been discussed with the use of NORSAR3D simulations and theoretical formulas taken from Monk's article (Monk 2010). The case involving a dipping layer should also be considered correspondingly. However, no formulas for the Fresnel zone are provided by Monk (2010) if dips exist, but ray tracing can still be employed to calculate its size.

In our simulations, the Fresnel zone for a given shot-receiver pair will be calculated for a flat horizon rotating around its specular point (with specular point defined when no dip) The velocity field in the dipping layer model is same as the one used in model B and the depth of the horizon is 3km.

Figure 3.15 gives a sketch of the simulated cases with the location of the specular point moving upwards along the surface when the angle increases. In Table 3.4, the dimensions of the Fresnel zone for different dip angles are listed in case of no dip.

Table 3.4: The dimensions of the Fresnel zones for different dipping layers.

Dipping angle (θ, degree)	0 (flat horizon)	5	10	15	20	25	30	35
Inline (m)	1208	1188	1182	1178	1139	1125	1101	1082
Crossline (m)	776	764	752	732	688	648	592	516

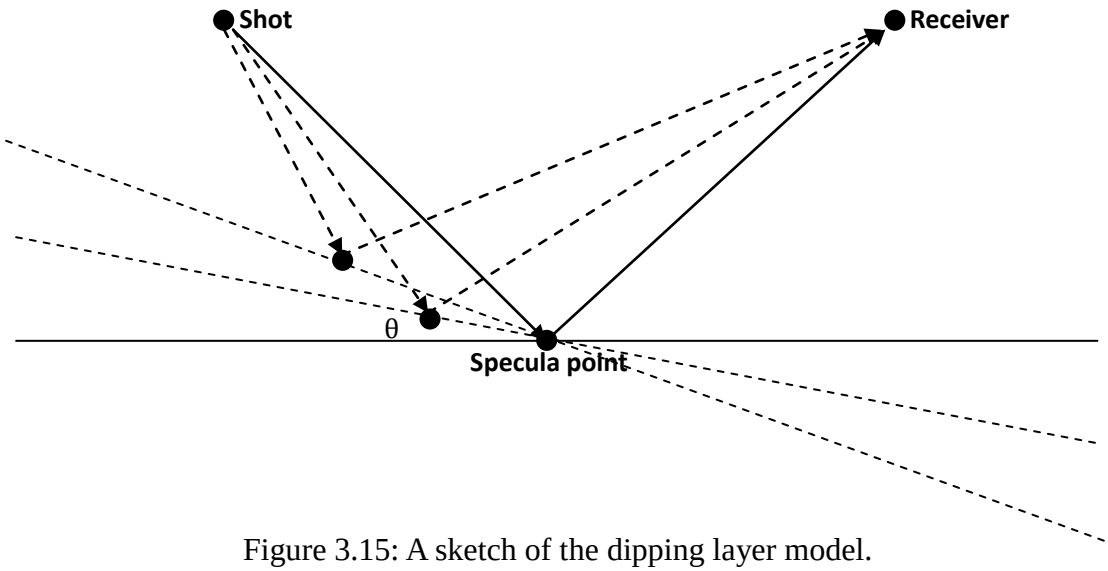

Figure 3.15: A sketch of the dipping layer model.

In Figure 3.16 the widths of the Fresnel zone as given in Table 3.4 is plotted against dip angle.

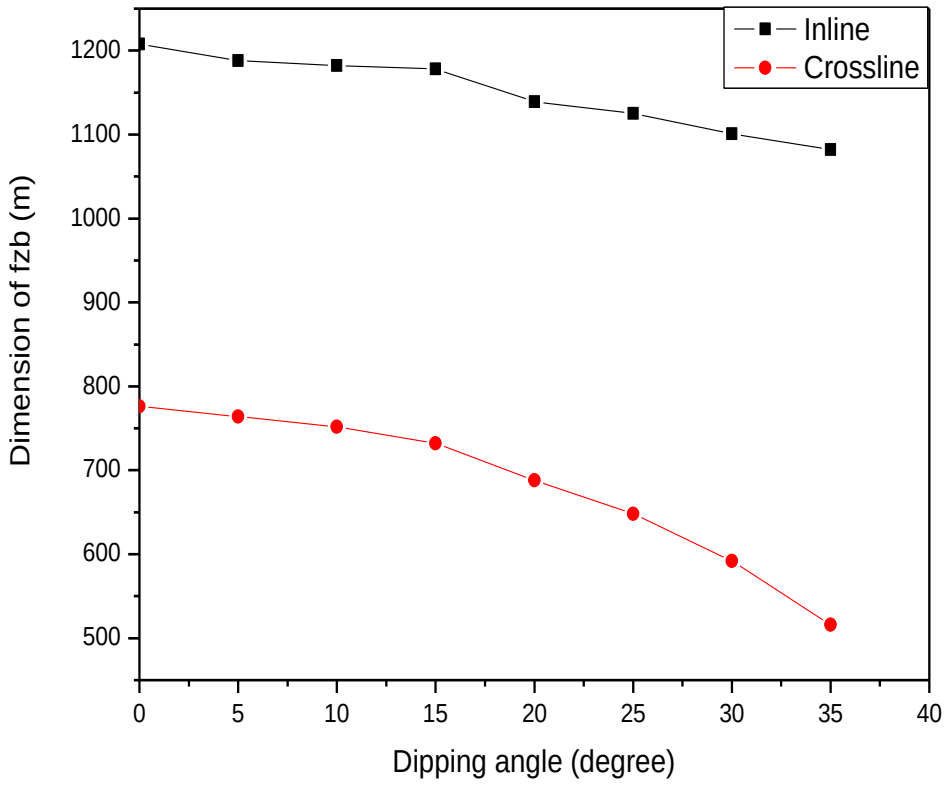

Figure 3.16: Width of the Fresnel zones with different dipping angles

From Fig.3.16, it follows that the width of the Fresnel zone shrinks with increasing dip angle. This is especially true for the crossline direction. These observations show that straight forward use of the Fresnel zone dimensions valid for a non-dipping reflector to also predict the zone in case of layer dipping is not accurate enough when

applied in Fresnel zone binning (angles larger than about 10^{o}).

3.3.3 Quality control of Fresnel zone simulation

In case of a gradient-velocity model it has already been shown that the analytical formulas of Monk (2010) show a large discrepancy when compared with ray tracing in case of the inline width of the Fresnel zone.

As an independ check of this result ray tracing was replaced by the analytical travel time formulas valid for a gradient model:

$$t = \left(\frac{1}{g}\right)\cosh^{-1}\left(1 + \frac{g^2(h^2 + z^2)}{2V_0(V_0 + gz)}\right) \qquad (3.4)$$

Where h is half-offset, g is velocity gradient, z is the depth of target surface and V_0 is the sediment velocity.

As before the travel times (T_2+T_3) for the non-specular points were calculated (by varying h_s in Fig.3.17) and compared with the corresponding two-way travel time T_1 of the specular point. The Fresnel zone was then defined by the area of non-specular points fulfilling the $\frac{T}{2}$ condition.

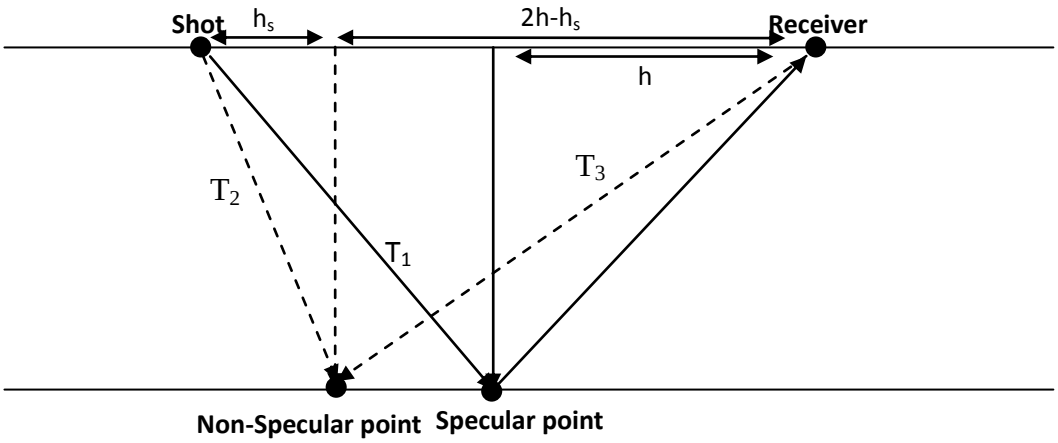

Figure 3.17: A sketch showing ray paths for different cases (specular and non-specular)

Employing the formula in Eq. 3.4, the inline dimensions of the Fresnel zone could be computed as listed in Table 3.5.

As expected, the difference between ray tracing and the use of the analytical travel time formula is negligible (only a 2-3 percent difference on average).

Table 3.5: The inline dimension of the Fresnel zones calculated from raytracing (NORSAR3D), analytical travel time formula (Matlab) and average velocity (Matlab)

Receiver no.	Incident angle (degree)	Half offset (m)	Simulation (NORSAR3D)	Simulation (Matlab) (analytical travel time)	Simulation (Matlab, average velocity)
			Inline (m)	Inline (m)	Inline (m)
1	6	249	628	-	-
20	8	318	632	636	636
40	10	416	636	652	640
60	13	526	644	660	644
80	16	641	656	666	654
100	18	759	672	678	662
120	21	879	678	686	670
140	24	1001	686	700	682
160	27	1123	694	718	698
180	30	1246	710	732	712
200	32	1369	734	754	726
220	35	1492	762	772	744
240	38	1616	786	796	764
260	40	1740	804	820	784
280	43	1864	826	848	804
300	45	1988	862	876	828
320	47	2112	898	908	852
340	50	2236	926	944	876
360	52	2361	958	980	906
380	54	2485	1000	1018	934
400	56	2610	1048	1060	960
420	58	2734	1088	1104	992
440	60	2859	1134	1152	1022
460	62	2984	1188	1204	1056
480	64	3108	1246	1260	1088
500	65	3233	1300	1322	1122
520	67	3358	1366	1388	1156

Based on the different cases, the inline dimension of the Fresnel zones were plotted together in Figure 3.17.

Also the approximation of replacing the gradient velocity model with an average velocity (straight ray) model was investigated. Figure 3.17 shows a plot of the results obtained for the various approaches. It follows from this figure that in case of a velocity gradient model, the inline width of the Fresnel zone should be calculated from the constant-velocity formula (with the proper average velocity employed) rather

than the gradient velocity formula as proposed by Monk (2010).

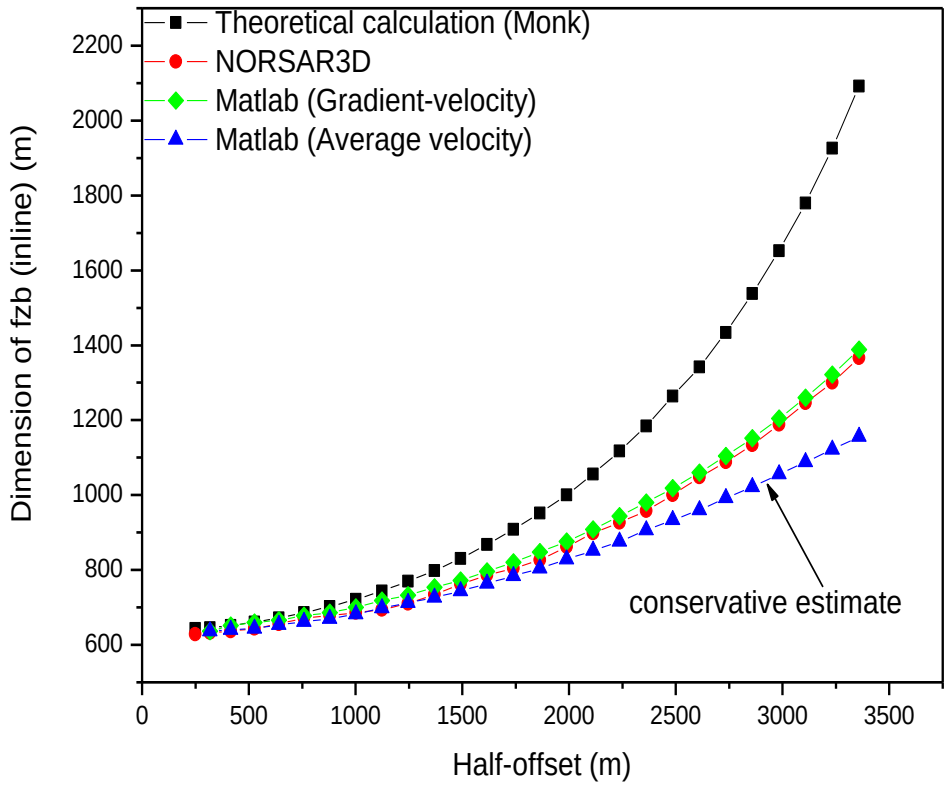

Figure 3.17: The inline dimension of the Fresnel zone as predicated from the various approaches.

3.3.4 Sensitivity analysis of the inline Fresnel zone width

In the first simulation Eq. (3.4) was used to investigate how the inline Fresnel zone width varies with the velocity gradient.

The initial sediment velocity V_0 is 2km/s, the target layer was at 3km depth and the gradient was varied between 0.4 to $1s^{-1}$. Figure 3.18 shows how the inline dimension of the Fresnel zone varies with different velocity gradients. The corresponding results are summarized in Table 3.6 for various offsets.

Table 3.6: The inline dimension of the Fresnel zones calculated using Eq.(3.4) (Matlab implementation)

Receiver no.	Half offset(m)	Gradient (g=0.4)	Gradient (g=0.6)	Gradient (g=0.8)	Gradient (g=1)
1	249	--	--	--	--
20	318	580	636	636	636
40	416	584	652	708	768
60	526	588	660	716	776
80	641	594	666	726	786

100	759	602	678	734	798
120	879	614	686	750	814
140	1001	626	700	762	830
160	1123	638	718	782	850
180	1246	652	732	800	876
200	1369	670	754	822	898
220	1492	684	772	848	928
240	1616	704	796	872	956
260	1740	724	820	904	992
280	1864	748	848	936	1028
300	1988	772	876	968	1068
320	2112	796	908	1008	1112
340	2236	824	944	1048	1160
360	2361	854	980	1090	1214
380	2485	882	1018	1138	1274
400	2610	916	1060	1192	1336
420	2734	948	1104	1248	1404
440	2859	986	1152	1310	1482
460	2984	1024	1204	1376	1564
480	3108	1064	1260	1448	1660
500	3233	1110	1322	1530	1762
520	3358	1156	1388	1616	1880

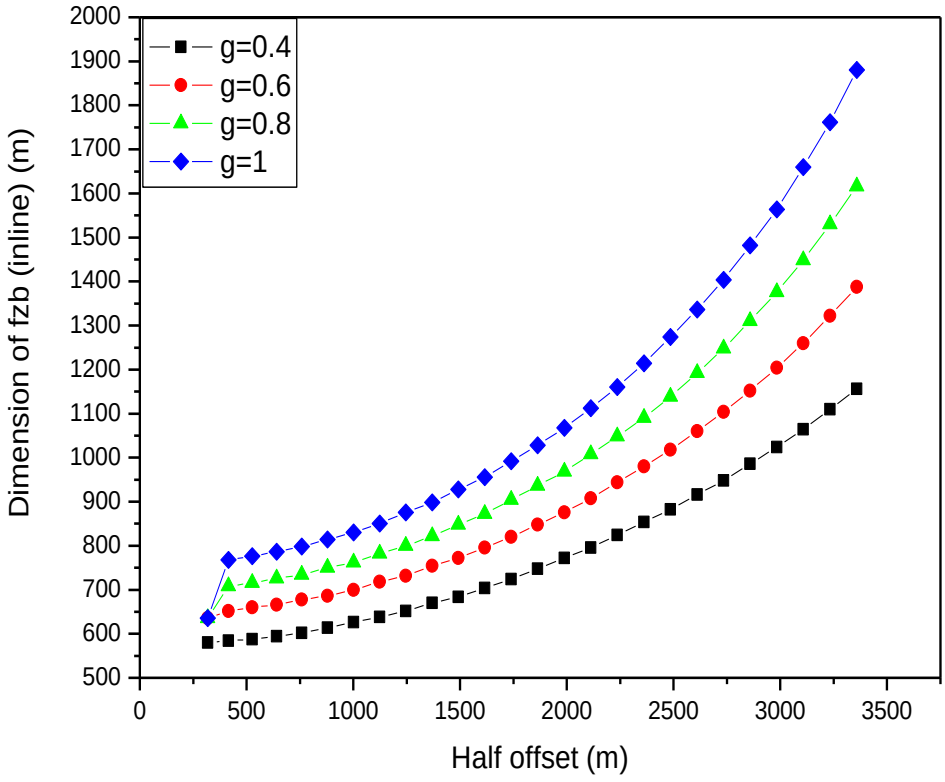

Figure 3.18: The inline dimension of the Fresnel zone for different gradients

In his paper Monk (2010) presented a similar study as that in Fig.3.18 (for a fixed half-offset of 1500m) with the same range of velocity-gradients.

Again he used the approximate formula Eq.(3.1) to calculate the inline Fresnel zone width. As before, the results obtained in Fig.3.18 are much more conservative than the ones advocated by Monk (2010).

For a fixed velocity gradient ($g=0.6\ s^{-1}$) and varying frequency (cf. Eq(2.4)), the sensitivity of the inline width of the Fresnel zone was also investigated with respect to target depth.

Table 3.7: The inline dimension of the Fresnel zone calculated for different depths of target surface.

Receiver no.	Half offset (m)	The depth of target surface (1km)	The depth of target surface (2km)	The depth of target surface (3km)
1	249	--	--	--
20	318	216	480	636
40	416	332	484	652
60	526	356	496	660
80	641	382	506	666
100	759	418	522	678
120	879	458	538	686
140	1001	502	562	700
160	1123	554	586	718
180	1246	616	612	732
200	1369	678	642	754
220	1492	752	672	772
240	1616	832	708	796
260	1740	928	748	820
280	1864	1032	788	848
300	1988	1156	836	876
320	2112	1304	884	908
340	2236	1476	940	944
360	2361	1698	998	980
380	2485	1970	1062	1018
400	2610	2320	1136	1060
420	2734	2752	1216	1104
440	2859	3254	1306	1152
460	2984	3792	1404	1204
480	3108	4328	1516	1260
500	3233	4850	1650	1322
520	3358	5352	1800	1388

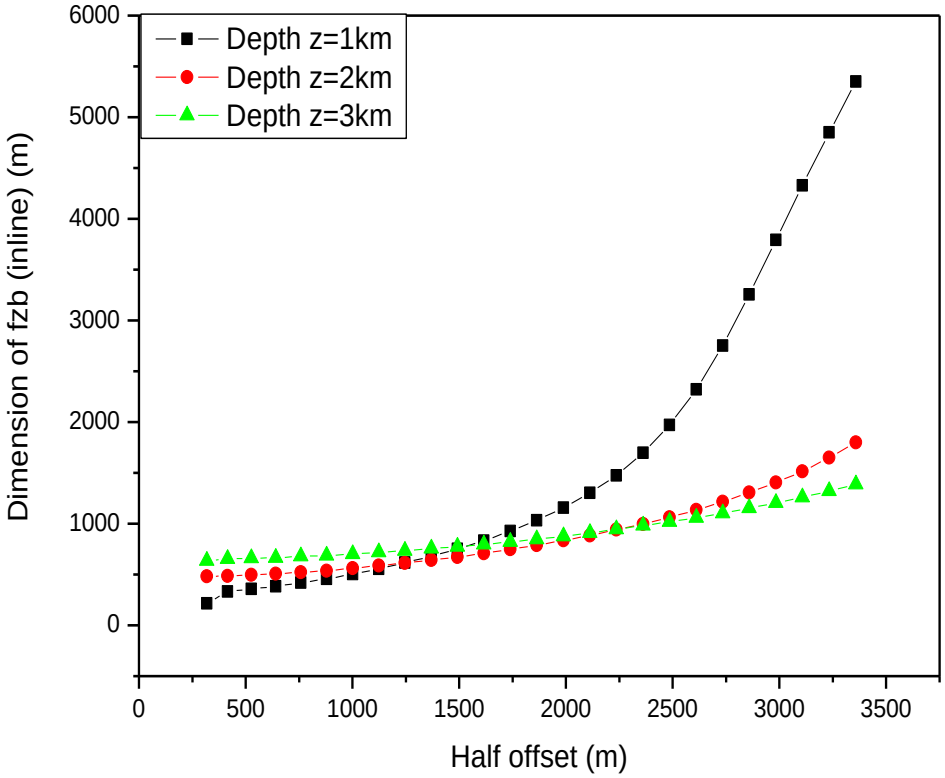

Figure 3.19: The inline dimension of the Fresnel zone calculated for different depths of target surface.

The results obtained are presented in both Table 3.7 and Figure 3.19. Monk (2010) presented a similar analysis for a constant-velocity model and a fixed frequency of 30Hz. The main observations made here are similar to that of the constant velocity case: the Fresnel zone dimension increases with depth at near offset, however, at far offsets the Fresnel zone dimension decreases with depth. Based on theoretical formulas (Eqs. 1.6 and 1.7) in article (Monk, 2010), Figure 3.20 (a), (b) and (c) show Fresnel zones corresponding to different depths at far offset (half offset is 3.358km).

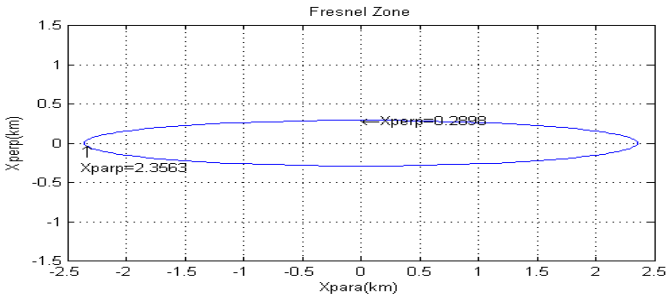

(a)

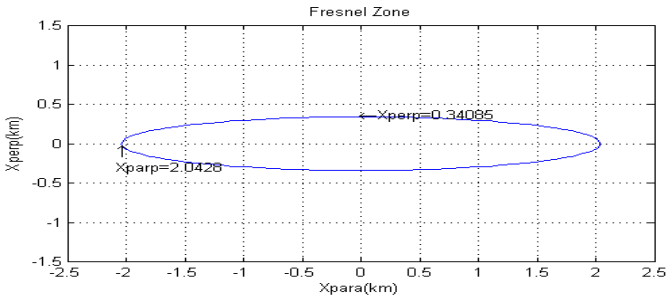

(b)

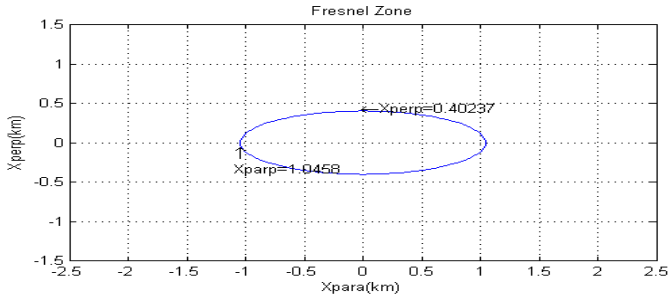

(c)

Figure 3.20 (a)-(c): The Fresnel zones of different depths at far offset: (a): 1km; (b): 2km; (c): 3km.

The dimensions of the Fresnel zones in Figure 3.20 (a)-(c) are listed in Table 3.8

Table 3.8: The dimensions of the Fresnel zones at far offset

	Depth (z=1km)	Depth (z=2km)	Depth (z=3km)
X_{para} (km)	2.356	2.043	1.046
X_{perp}(km)	0.290	0.341	0.402

3.3.5 The Fresnel zone in a complex model

The model in section 3.1 was employed to simulate the Fresnel zones in a complex model defined by curved surfaces. Figure 3.21 illustrates the ray paths for a fixed source at near, middle and far offsets. At both near and middle offsets, there were only one specular reflection event. However, at far offset three reflection events were present (cf. upper-right magnified figure). At the left specular point (on the dipping slope), the ray path represents the most energy one. At the right specular point, the travel time of the ray path is the minimum one of all three reflection events. In Figure 3.22, the actual Fresnel zones of these three specular points are illustrated in 3D. The Fresnel zones in Fig.3.22 are computed employing the ray tracing approach.

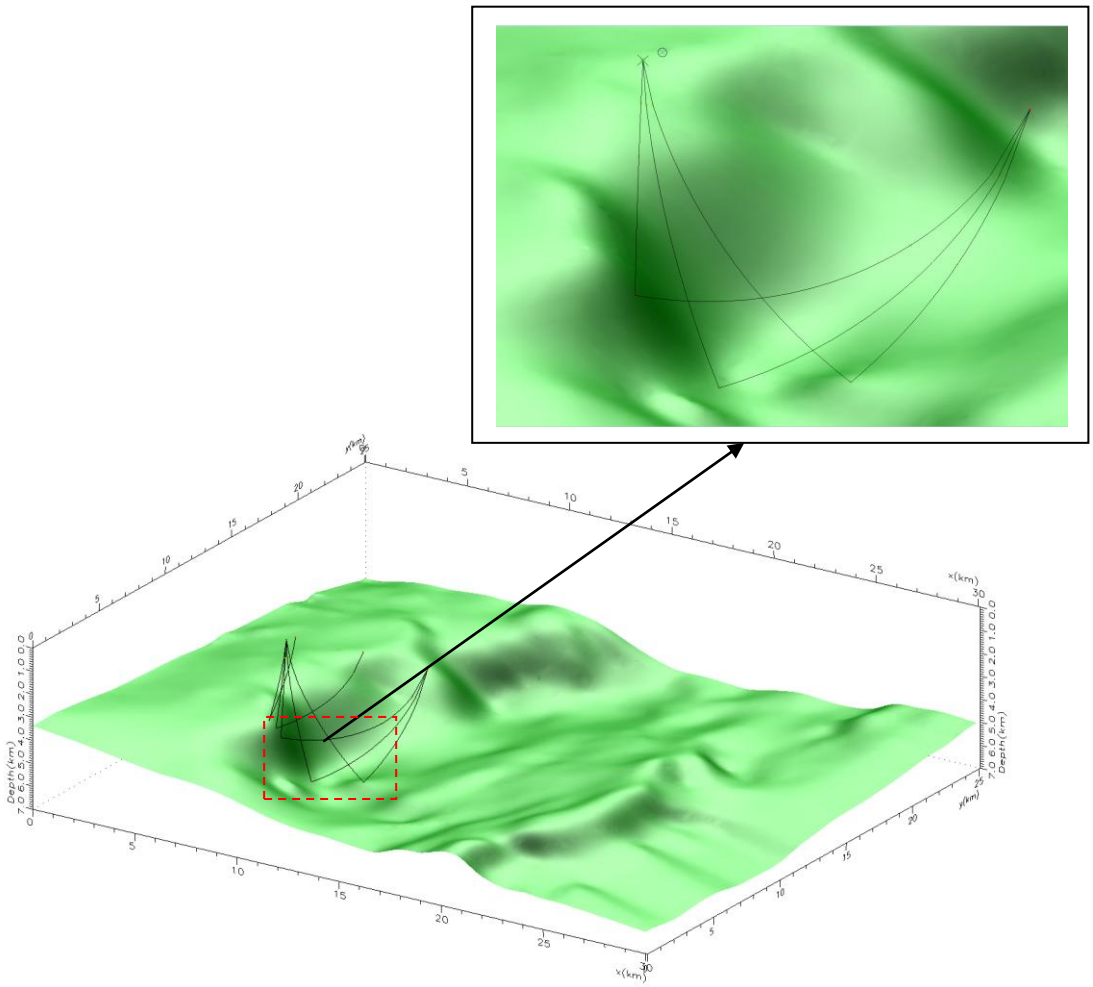

Figure 3.21: The actual ray paths for a fixed shot in the complex model; The ray paths at far offset in the upper-right sub-figure.

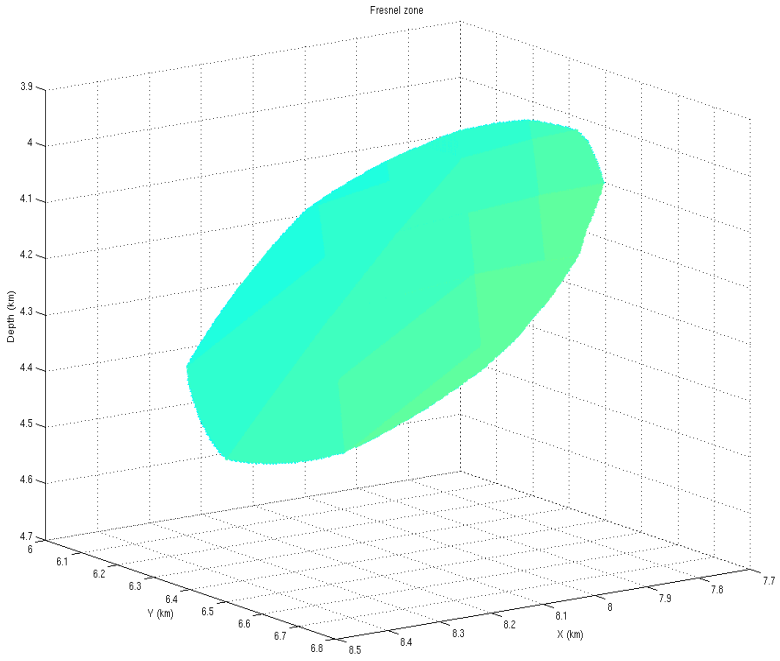

(a)

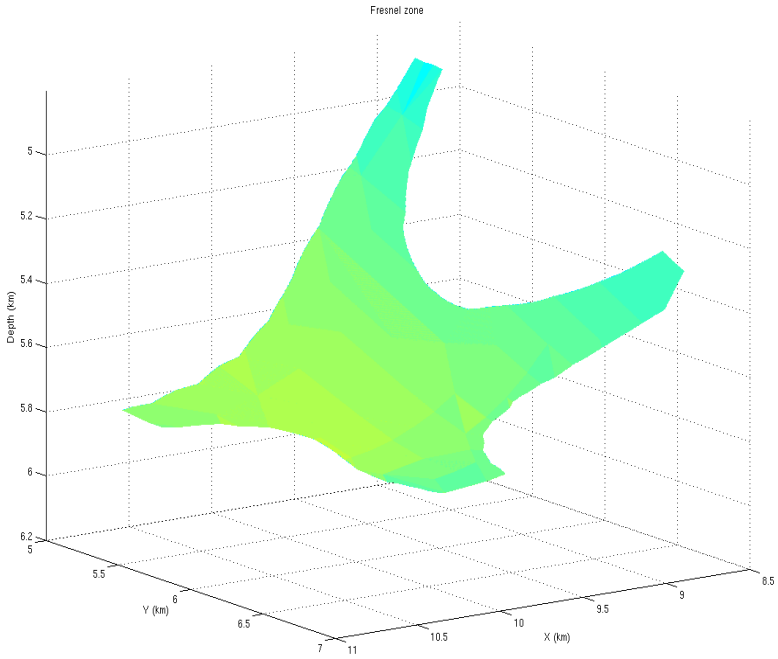

(b)

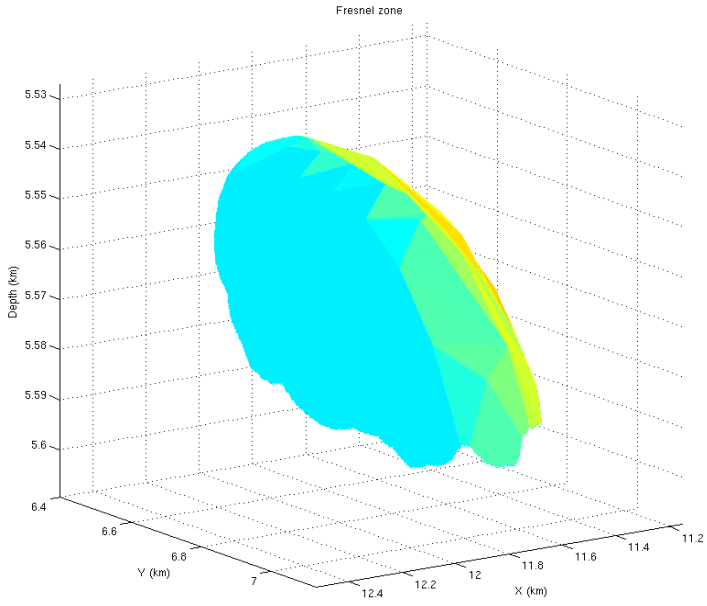

(c)

Figure 3.22 (a)-(c): The actual 3D Fresnel zones for the three specular points at far offset: (a) the left specular point; (b) the middle specular point; (c) the right specular point

From Figure 3.22 (a)-(c) it follows that the shape of the Fresnel zone can be quite irregular in cases of a complex model. This observation should further support our earlier conclusion that the simple analytical Fresnel zone formulas introduced in the Fresnel zone binning analysis should be used with great care.

In the article of Monk (2010), the theory of sampling within the concept of Fresnel zone binning is introduced as 'For a given reflection event in the subsurface, seismic traces that have reflection-ray "points" within the Fresnel zone contribution constructively to the output seismic traces at the center of the Fresnel zone when data are migrated. Conversely, a trace with a ray point at the center of the Fresnel zone actually samples all points on the reflection event with Fresnel zone'. The coordinates of the shot- receiver pair at the various offsets are listed in Table 3.9 together with the mid-point (CMP) coordinate. The corresponding true locations of the specular points are given in Table 3.10.

Table 3.9: The coordinates of the shot-receiver pair for the various offsets

	Near offset		Middle offset		Far offset	
Coordinate (m)	X (m)	Y(m)	X(m)	Y(m)	X(m)	Y(m)
Shot	8204	6493	8204	6493	8204	6493
Receiver	8384	6915	11622	7045	14870	6881
CMP	8394	6704	9913	6769	11537	6687

Table 3.10: The locations of the specular points for the various offsets

	Near offset		Middle offset		Far offset	
Coordinate (m)	X (m)	Y(m)	X (m)	Y(m)	X (m)	Y(m)
Specula points	7314	6550	7716	6453	8053	6322
					9813	5909
					11816	6768

In general, it follows from Tables 3.9 and 3.10 that the specular points do not coincide with the corresponding CMP locations for a complex model. Moreover, in the far offset case, three different specular points exist: one associated with the maximum energy, one associated with the shortest travel time and one that fall in between the others two. Hence, in such a case involving multiple Fresnel zones the simple formulas proposed by Monk (2010) break down.

The concept of Fresnel zone binning is further analyzed in the next chapter by introducing migration. Only by considering final seismic images, the usefulness of this technique can be clearly quantified.

Chapter 4 Migration

In Chapter 2, it was demonstrated that the 'coverage holes' caused by the survey could be minimized employing Fresnel zone-based infill management. In Chapter 3, comparison between hit maps and coverage maps based on Fresnel zone binning demonstrated that the latter concept has the potential of decreasing the percentage of infill needed. In this Chapter, Pre-Stack time migration (PSTM) will be employed to further test Fresnel zone-based infill management.

4.1 Synthetic seismic data and area of interest

The synthetic seismic data (SEGY format) employed in migration were generated in NORSAR3D assuming a zero-phase Ricker pulse. To include the effect of absorption of the Earth, the center frequency of the pulse changed at each model interface, e,g. respectively chosen to be 60Hz, 50Hz, 40Hz, and 30Hz. (c.f .Fig 4.1)

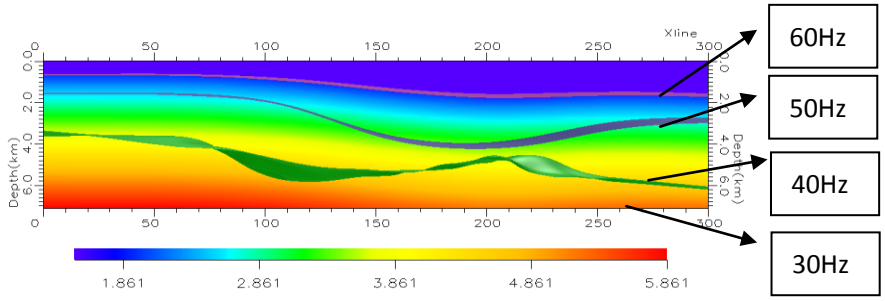

Figure 4.1: The pulse frequency associated with the respective surfaces.

Before carrying out migration, a proper survey area has to be chosen. Figure 4.2 shows the selected survey area and the corresponding geological structures of the model.

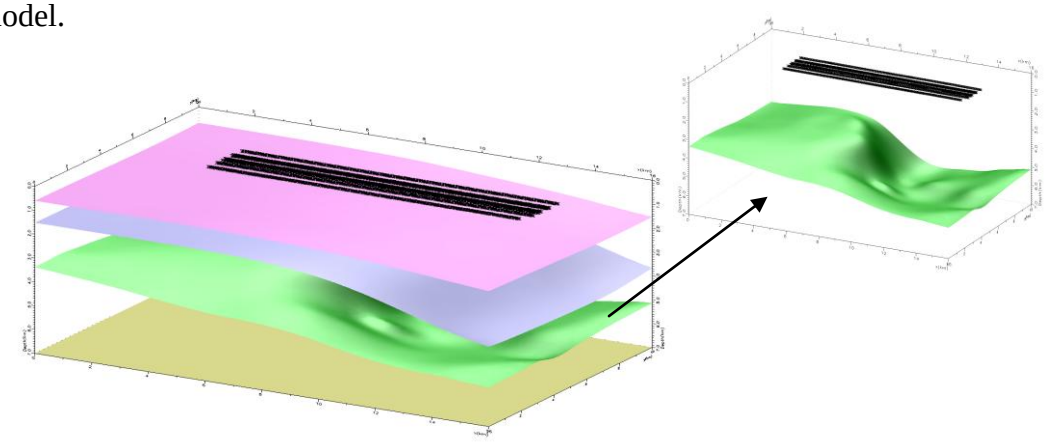

Figure 4.2: Survey area for migration and the corresponding geological structures. Upper right sub-figure shows target surface only.

Within the survey area, a strong dipping structure exists along the target surface (upper-right in Fig 4.2). The approximate dimension of the area covered by all the five navigation lines is 10.8km (inline direction) × 2.5km (crossline direction). To test Fresnel zone-based infill management, PSTM was applied to three different synthetic seismic data sets. In the first survey, the survey area was covered by five navigation lines (from navigation line 14 to navigation line 18) without feathering. In the second survey, the survey area was also covered by the same number of navigation lines (as used in Chapter 2) but now with strong feathering included. In the third survey, two new navigation lines (navigation line 19 and 20) were designed based on Fresnel –zone analysis to fill in the 'coverage holes' caused by the feathering in the second survey. By comparing the respective time migration results of these three surveys, the Fresnel zone-based infill management can be further analyzed.

The main figure in Fig 4.3 shows the hit map at far offset associated with the second survey. Correspondingly, the upper right figure shows the coverage map of a selected part associated with the third survey and the upper left figure shows the hit map after reshooting. The Fresnel zone based infill management has restored most of the coverage holes.

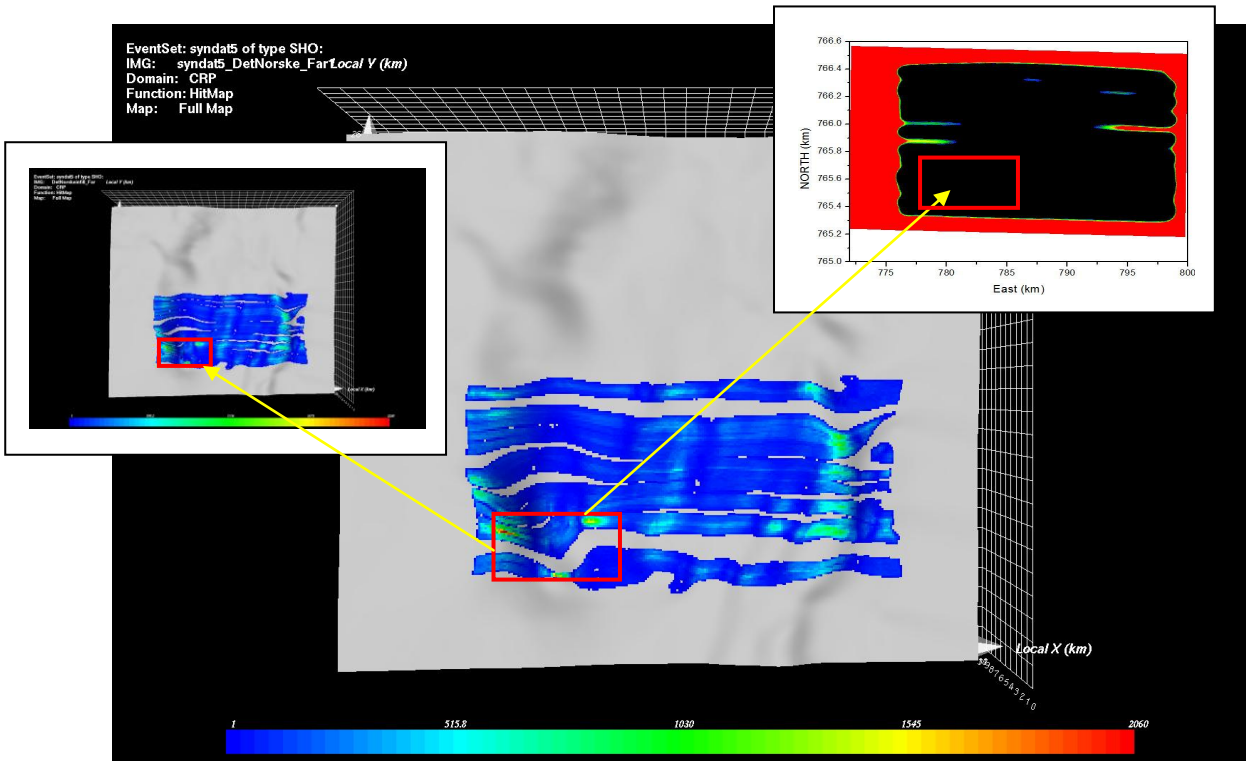

Figure 4.3: The hit map of survey 2 (main figure) and the coverage map associated with survey 3 (upper right) after Fresnel zone-based infill management. Upper left figure shows the hit map after reshooting. The red box indicates the approximate location of the area used in migration

4.2 Data processing and Pre-stack Time Migration (PSTM)

The synthetic seismic data sets were processed using the Uniseis software package. The basic 3D processing flow used in the thesis is shown in Figure 4.4.

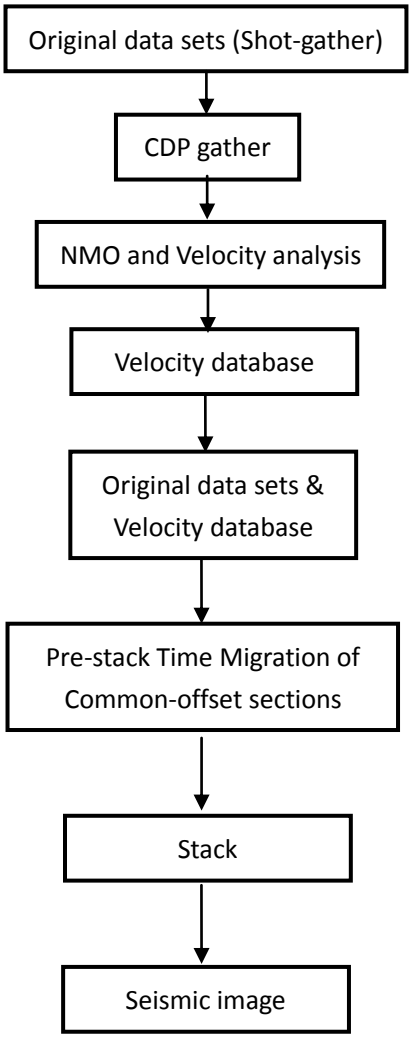

Figure 4.4: The processing flow in case of both feathering case and non-feathering.

In a general processing flow, regularization is needed for a survey including feathering. In case of strong feathering, it is most likely that the number of traces in each bin cell is not the same, and even in some cases, there is no trace at all in the cell. Therefore, regularization ensures that the number of traces in each bin cell is almost the same. However, in this thesis, our task is to test if Fresnel zone-based infill management can minimize the effect of feathering. Since the feathering phenomenon will be reduced by regularization, it was not applied to the seismic data in survey 2 and 3.

There are five navigation lines in our survey area. The separation between each

navigation line is 500 meters. In the grid file, the size of each bin cell is set to 6.25m (inline) × 25m (crossline). Therefore, 20 inlines were generated (the flip-flop shooting case) for each navigation line giving a total of 100 inlines in the survey (defined by inline3D number ranging from 98 to 197). The coordinate of each CDP was determined from the corresponding coordinates of shot and receiver. The range of the CDP3D number is from 559 to 2805 in the survey.

In Figure 4.5, the survey area (yellow color) representes that part of the grid file corresponding to the range of the inline3D and CDP3D numbers.

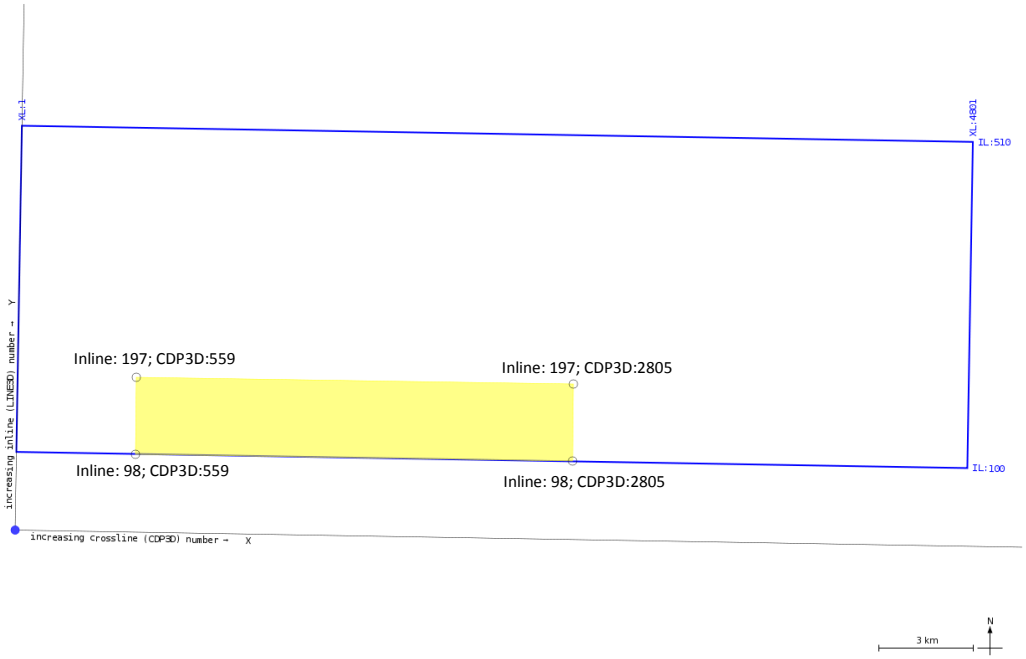

Figure 4.5: The range of the survey area associated with inline3D number and CDP3D number.

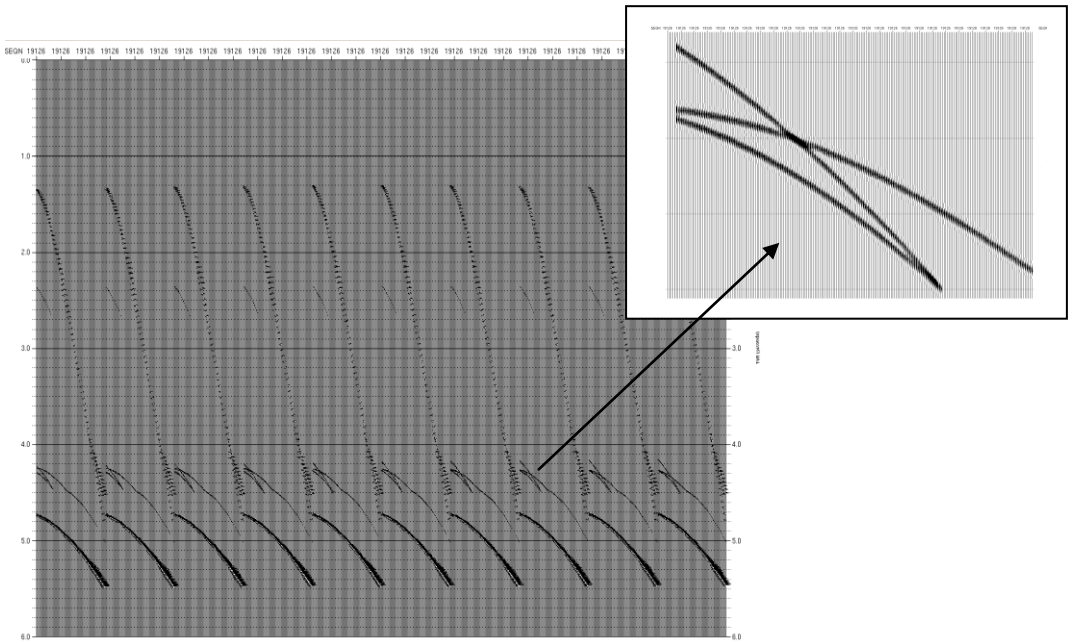

Figure 4.6: An original shot gather (10 cables) corresponding to navigation line 16 (main figure) and an enlarged part of the data (upper-right sub-figure)

In the main part of Figure 4.6, the original seismic data of one shot (navigation line 16) is shown. Reflections associated with each of the four horizons of the model can be clearly observed. The upper right figure shows an enlarged part of the data exhibiting a bow-tie (multi-path) appearance caused by the complexity of the model.

During the 3D seismic data processing, the original seismic data (shot-gathers) were sorted into CDP gathers and then a velocity analysis was carried out to build up the velocity database of the survey area. Figures 4.7 (a) – (c) show respectively the semblance at one CDP location, the corresponding CDP gather, and the picked velocity function.

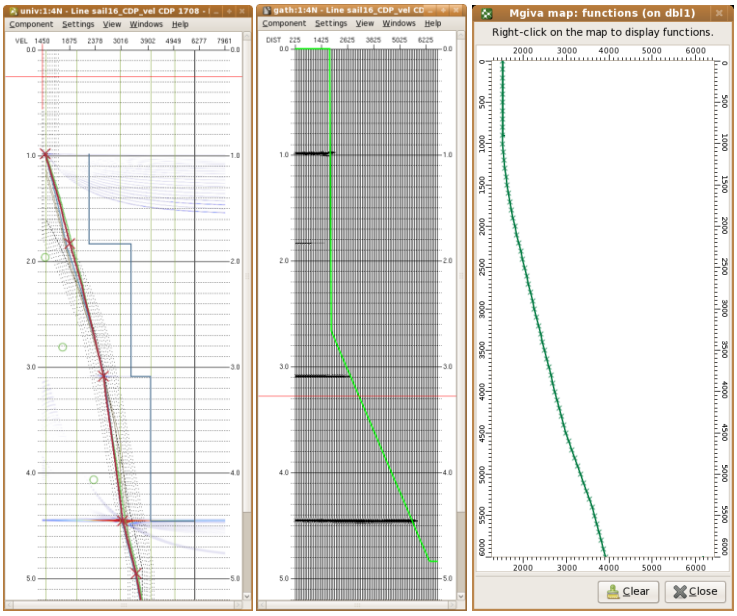

(a) (b) (c)

Figure 4.7 (a)-(c): The velocity semblance (a), CDP gather (b) and corresponding velocity function

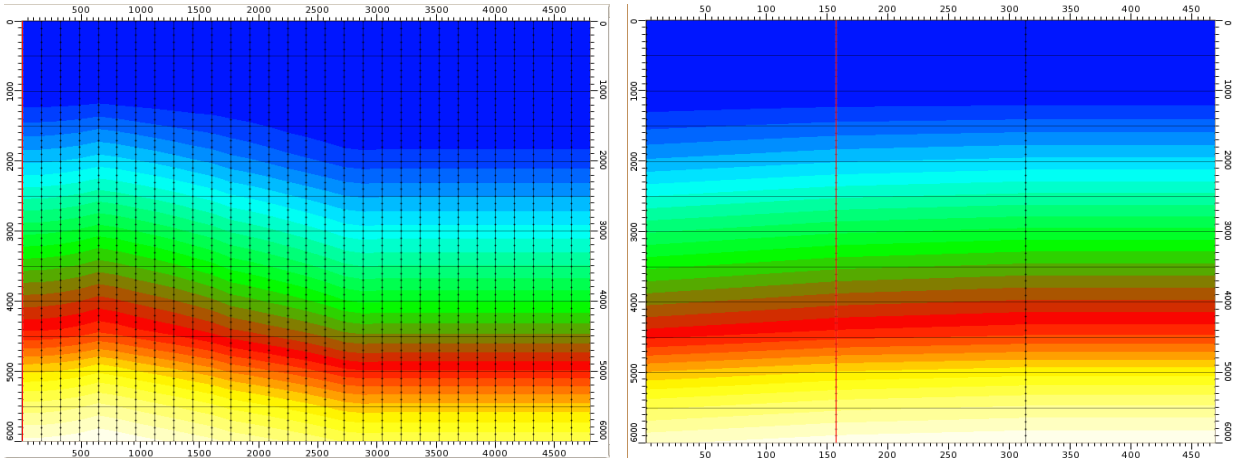

(a) (b)

Figure 4.8 (a)-(b): The velocity distribution along inline direction (a) and crossline direction (b)

Based on the output from the velocity analysis, interpolation was applied to ensure a smooth velocity field. This RMS velocity distribution is necessary input to migration. Figure 4.8 (a) and (b) show the velocity distribution along inline and crossline directions. Before PSTM, two stacked sections (navigation line 16) for respectively survey 1 and survey 2 were generated as shown Figures 4.9 (a) and (b). These stacked sections defined the area of interest for the seismic imaging and were employed for quality control of velocity data base.

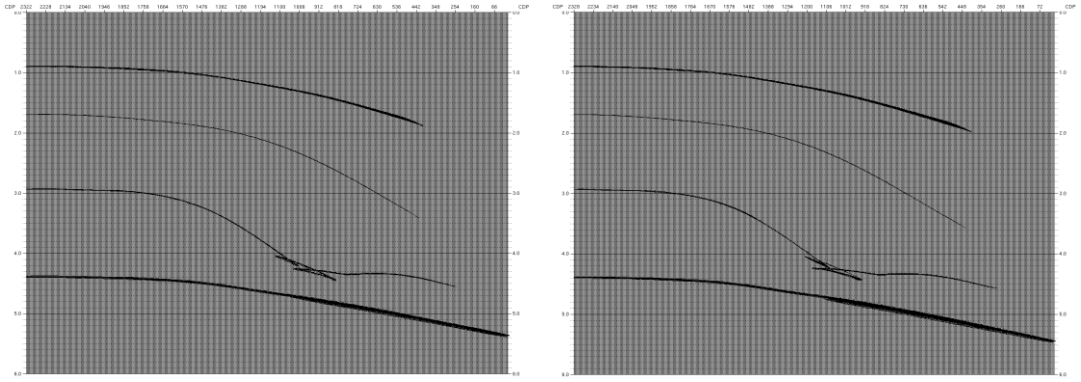

(a) (b)

Figure 4.9 (a)-(b): Stacked section of survey 1 (a) and survey 2 (b).

PSTM works on different kinds of input data and can handle conflict in dips efficiently. The original shot gather data was employed as input data in this thesis. The volume of the 3D seismic survey is defined by the range of inlines and crosslines. Inline seismic images can be created by stacking common-reflection point (CRP) gathers output from 3D PSTM. In this thesis, the commercial prestack migration package called Tsunami was employed. The migration aperture was 4km in both inline and crossline directions and the aperture angle was 45 degree. Figures 4.10 (a) and (b) show the 3D migration operators respectively intersected along both inline and crossline directions. The migration operators were calculated based on the near trace of a shot from navigation line 16. Due to survey limitations, the effective dimension of the migration operators was respectively 4km and 2.5km for the inline and crossline directions.

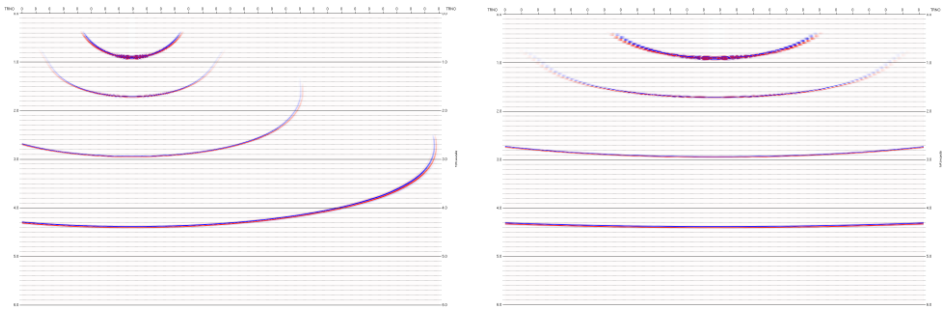

(a) (b)

Figure 4.10 (a)-(b): The migration operator in the inline direction (a); The migration operator in the crossline direction (b)

During the CRP stacking after PSTM, a mute function was employed for each CDP to eliminate the stretch (red ellipse in Fig.4.11 a) at far offset. Figures 4.11 (a) and (b) show a common-offset section respectively before and after a mute function has been applied. Consequently, even for the deeper reflections, a significant part of the far offsets were removed. This also implies that the effect of the Fresnel zone binning will be somewhat diminished.

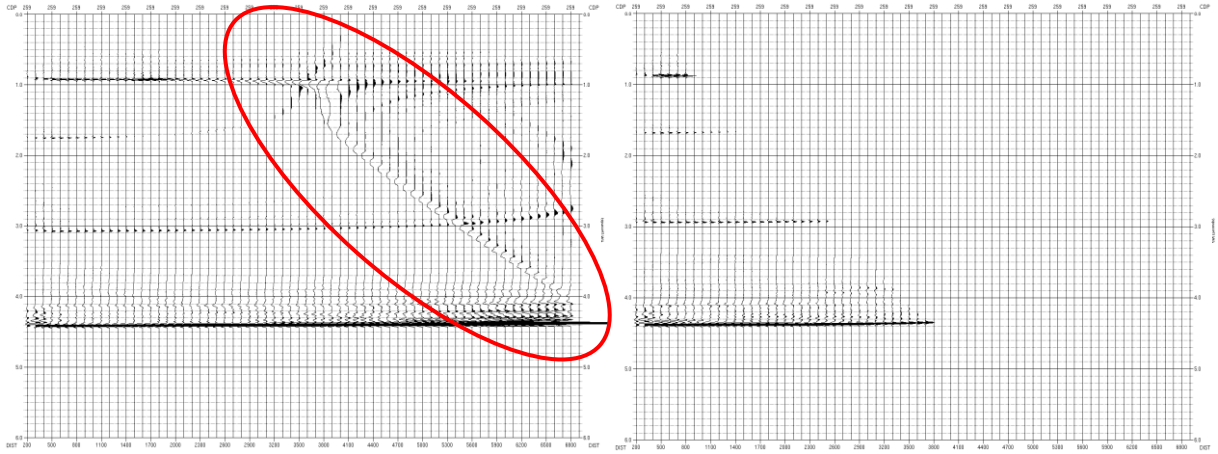

(a) (b)

Figure 4.11 (a)-(b): The common-offset section before mute function applied (a); The common-offset section after mute function applied (b)

4.3 Analysis of the Migration results

Black lines in Fig.4.12 represent original navigation lines and the two red dashed-lines are infilled navigation lines employed to minimize the 'coverage holes' in the survey area. The approximate area of the 'coverage holes' in the inline direction falls between inline numbers 138 and 178.

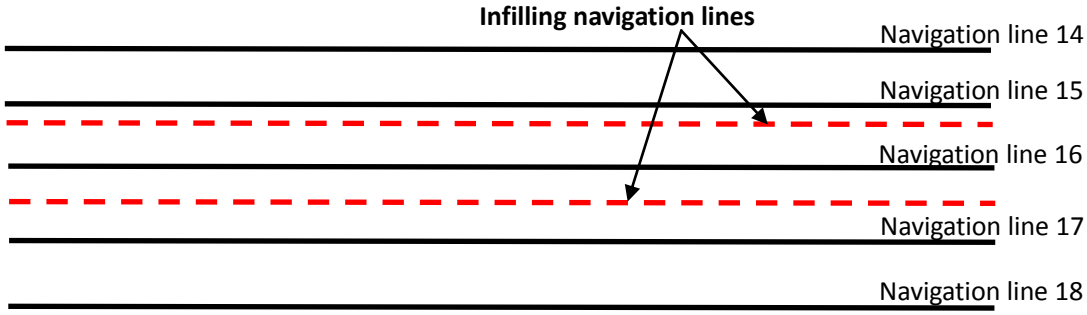

Figure 4.12: Fresnel zone-based infill management in the survey area. Black lines represent original navigation lines and the two red dashed lines show infilled navigation lines.

After PSTM in the inline direction, a family of images could be obtained representing inline numbers from 138 to 144 (the inline numbers are defined by grid file (cf.Fig.4.5)). The columns (a), (b) and (c) in Figure 4.13 show PSTM sections corresponding to respectively survey 1, survey 2, and survey 3. Furthermore, the first row in Figure 4.13 is inline 138 and the last row inline 144. Take now the PSTM image of inline 138 as an example to analyze Fresnel zone-based infill management. First row column (a) represents the ideal image. In column (b) the effect of feathering can be easily observed: the amplitude on the second subsurface is discontinuous (shown by red arrow) and there is also an obvious ‘coverage hole’ (shown by yellow arrow) caused by the amplitude losses on the third surface (target surface). After Fresnel zone-based infill management (first row, column (c)), the amplitude on the second subsurface was well recovered and the ‘coverage hole’ on the target was also well restored. Similar phenomena were also observed for the PSTM images of the other inlines.

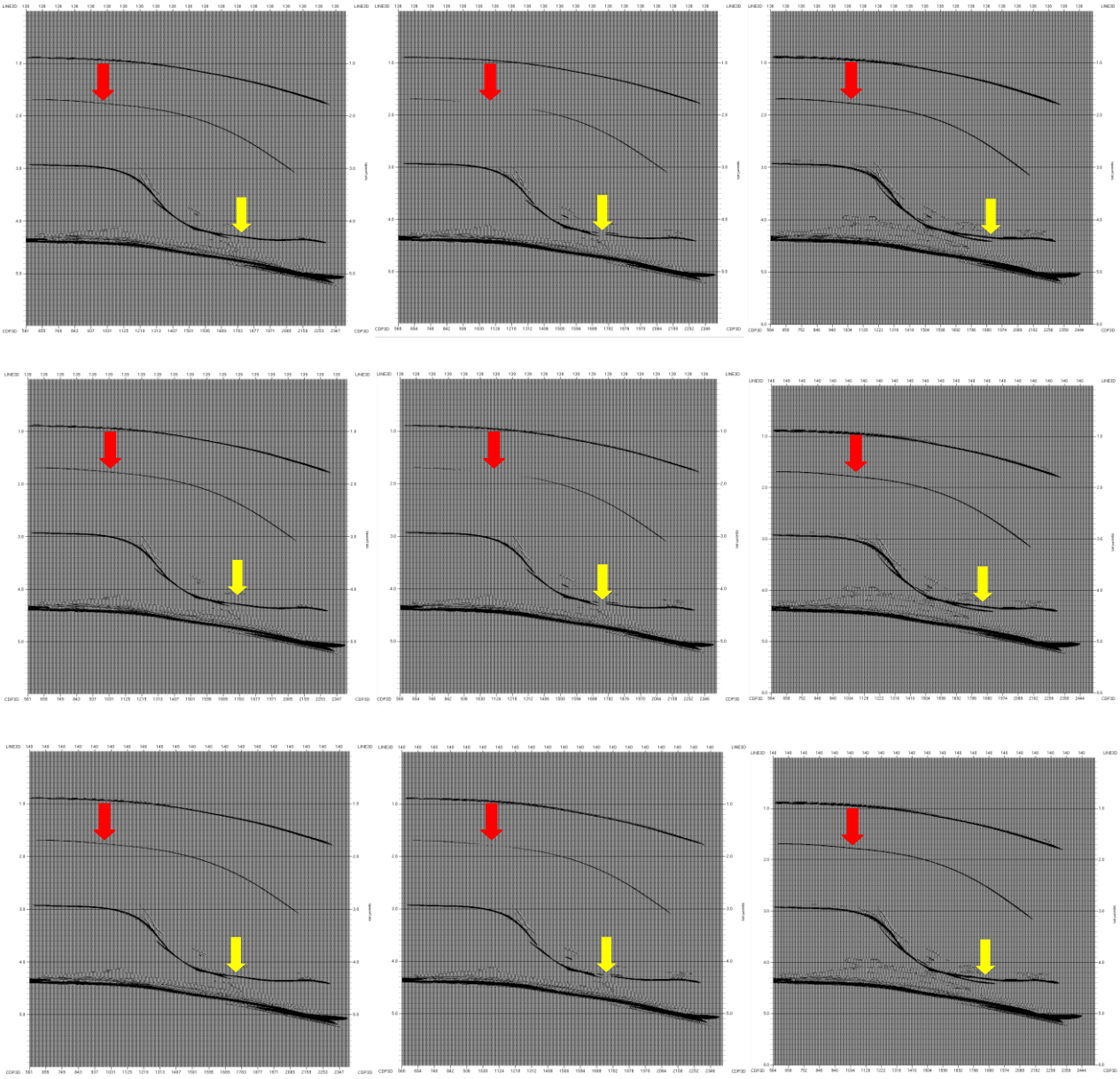

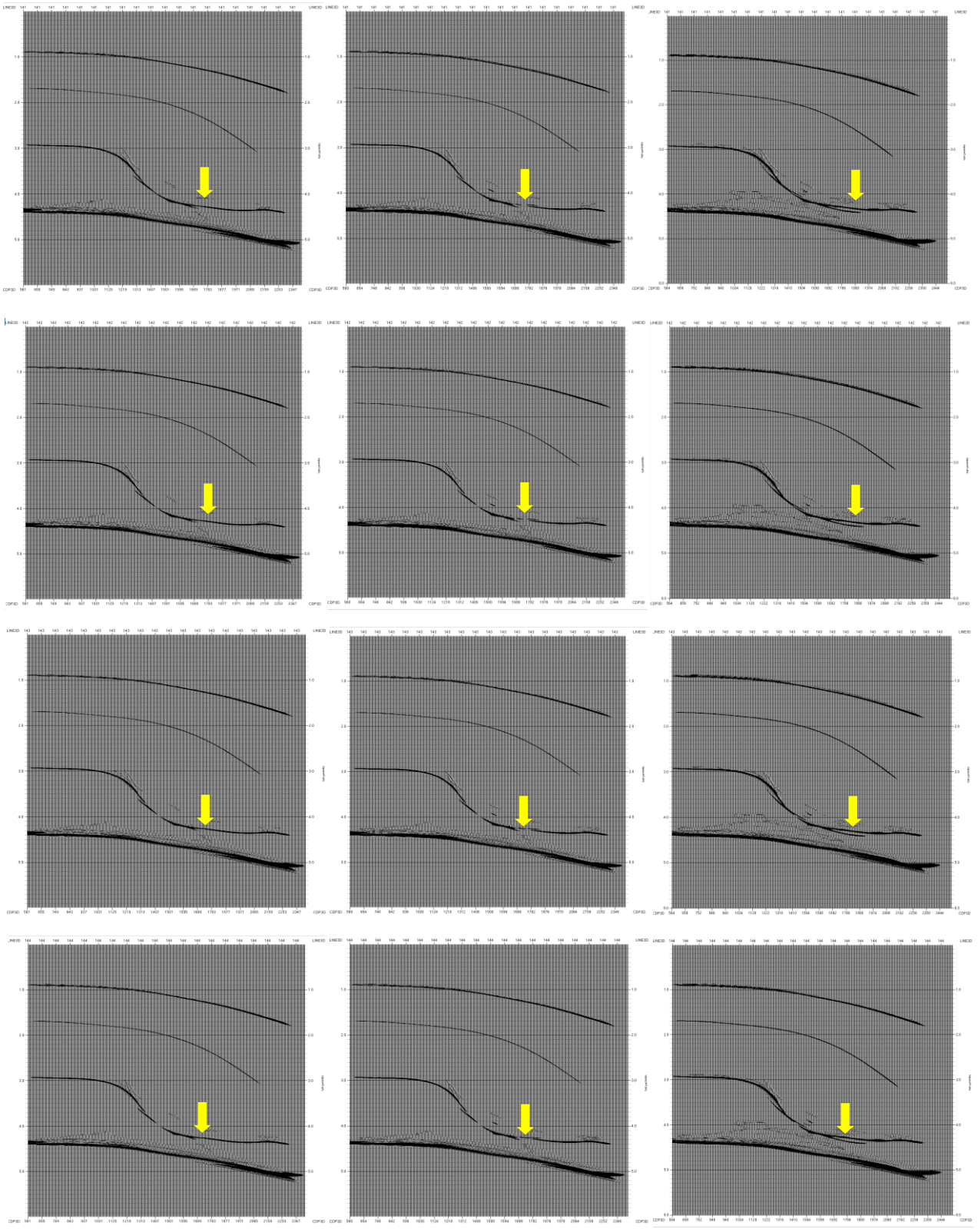

(a) (b) (c)

Figure 4.13 (a)-(c): Column (a): A series of PSTM images for survey 1; Column (b): A series of PSTM images for survey 2; Column (c): A series of PSTM images for survey 3;

To further analyze Fresnel zone-based infill management, the amplitudes (largest peak) associated with the second subsurface were picked for each inline and plotted (Figures 4.14 (a)-(c)).

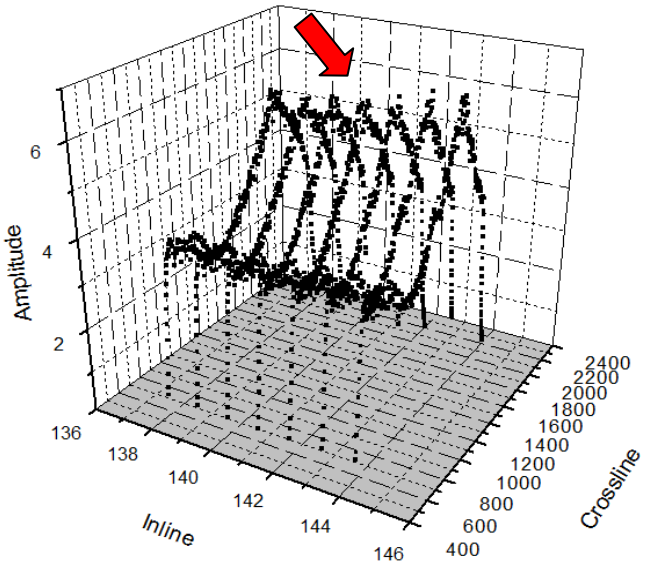

(a)

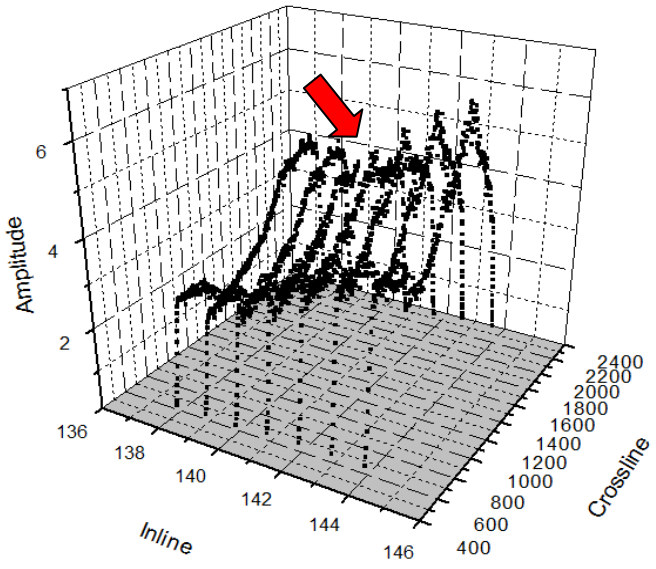

(b)

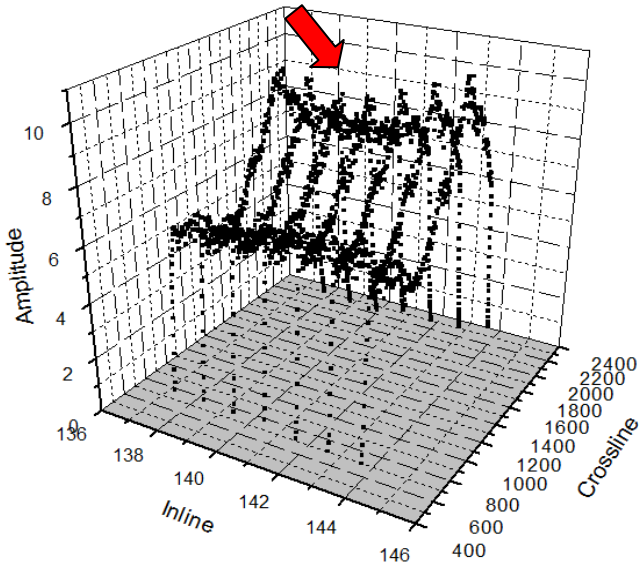

(c)

Figure 4.14 (a)-(c): Amplitude along the second subsurface: (a): survey 1; (b): survey 2; (c): survey 3.

Comparison of amplitudes in Figures 4.14 (a) and (b) show that the amplitude loss is serious in survey 2 caused by the strong feathering (shown by red arrow). After Fresnel zone-based infill management (Fig 4.14 (c)), the amplitudes along the second subsurface were significantly restored in survey 3 (although higher values than the ideal values in survey 1, cf. Fig. 4.14 (a)). Normally a regularization procedure is carried out before PSTM. This technique was decided not to be used here because it will make the analysis of the Fresnel zone binning concept more biased. However, since the Tsunami software apparently does not have a robust trace weight function the effect of introducing infill lines is prominent on the amplitudes. That is why the amplitude level of survey 3 is considerably higher than for survey 1. This phenomenon can be observed also in the figures to come. To further analyze the amplitude losses, inlines 138 and 139 were considered. The amplitude losses in dB were calculated from formula 4.1:

$$\text{Amplitude loss (dB)} = 20\log\left(\frac{A_1}{A_0}\right) \qquad 4.1$$

Where A_1 are the actual amplitude values along the reflector and A_0 represents reference amplitude as given from survey 1.

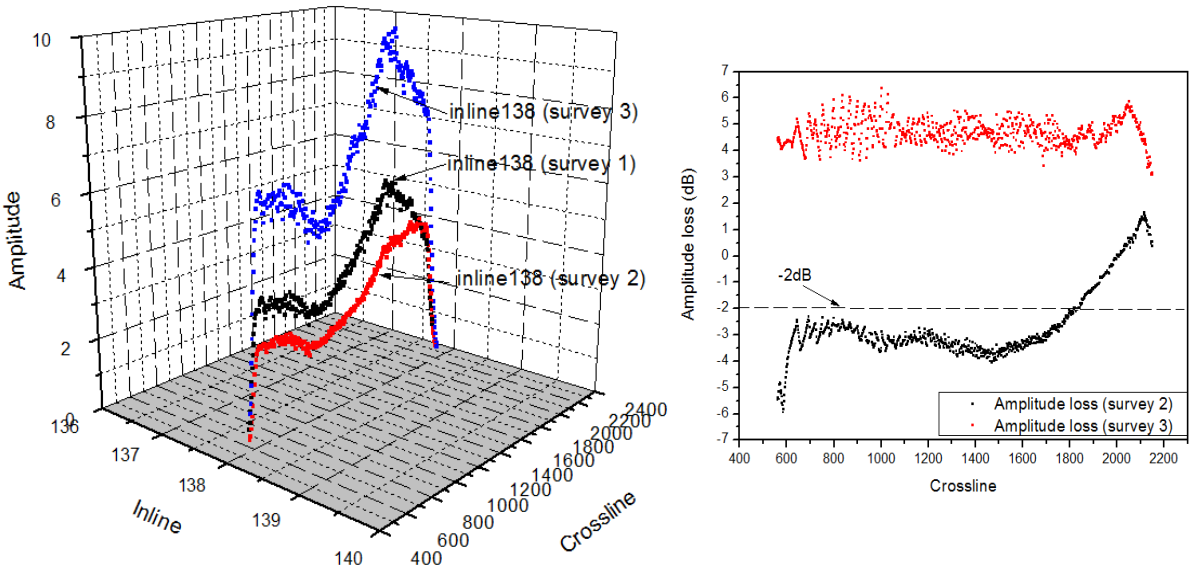

(a) (b)

Figure 4.15 (a)-(b): (a): Variation of amplitudes along the second subsurface (inline 138); (b): Amplitude losses for both survey 2 and 3.

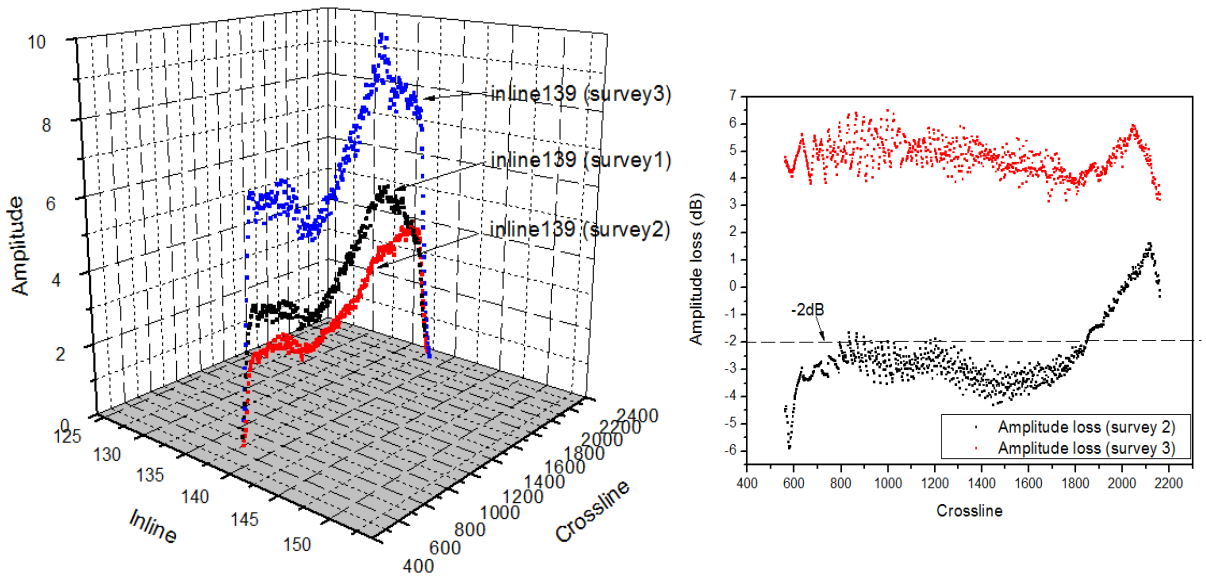

(a) (b)

Figure 4.16 (a)-(b): (a): Variation of amplitudes along the second subsurface (inline 139); (b): Amplitude losses for both survey 2 and 3.

Figure 4.15 (a) shows amplitude variations associated with inline 138. The corresponding amplitude losses (dB value) are shown in Figure 4.15 (b). The amplitude losses for survey 2 is below -2dB for most CDPs. However, after Fresnel

zone-based infill management, the amplitude losses were recovered and further strengthened (red nodes) in survey 3. In Figures 4.16 (a) and (b), similar phenomena were also observed for inline 139.

In Figure 4.13, the continuity of the target surface in the PSTM image was distorted by the 'coverage holes' (shown by yellow arrow). The CDP range of these 'coverage holes' for each inline is approximately from CDP number 1650 to 1780. Within this range, the amplitudes (largest peak) of respectively inline 140, 141 and 142 were picked and shown in Figure 4.17 (a). The corresponding statistical amplitude losses are shown in Figures 4.17 (b), (c) and (d).

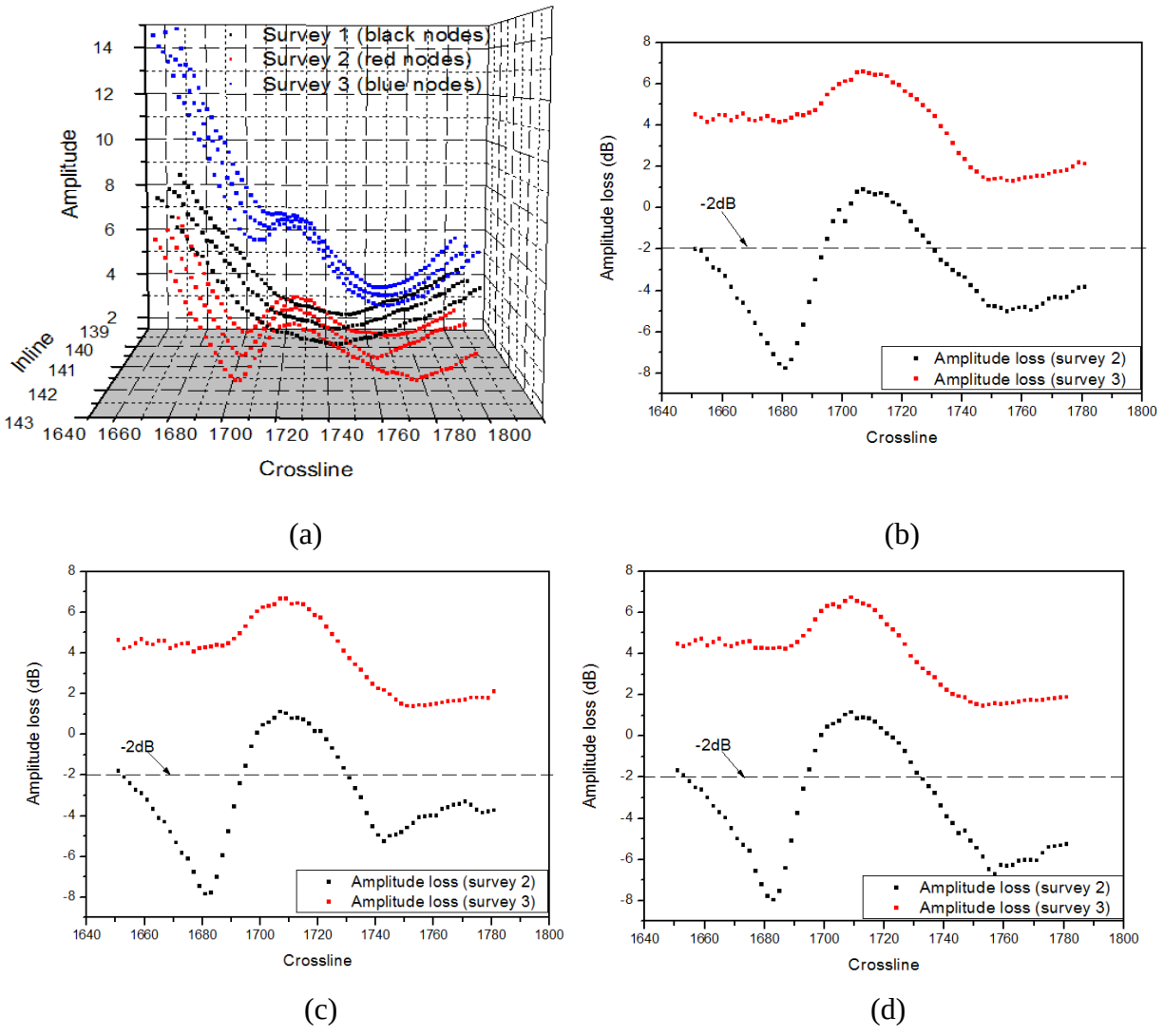

Figure 4.17 (a)-(d): (a): Amplitudes for CDP range 1650-1780 for respectively inline 140,141, and 142. (b): amplitude losses for inline 140; (c): amplitude losses for inline 141; (d): amplitude losses for inline 142;

In Figures 4.17 (b), (c) and (d), comparison of the amplitude losses between survey 2 and 3 demonstrates that the 'coverage holes' were well compensated after Fresnel

zone-based infill management. A similar amplitude loss analysis was also employed to the crossline PSTM images. Crosslines 1050 and 1700 were selected here. The reason for this choice is that crossline 1050 is located in the area where the amplitude losses on the second subsurface are severe and crossline 1700 is located within the 'coverage holes' on the target surface. Figure 4.18 (a) shows the variation in amplitudes along the second surface for crossline 1050. The corresponding amplitude losses are shown in Figure 4.18 (b).

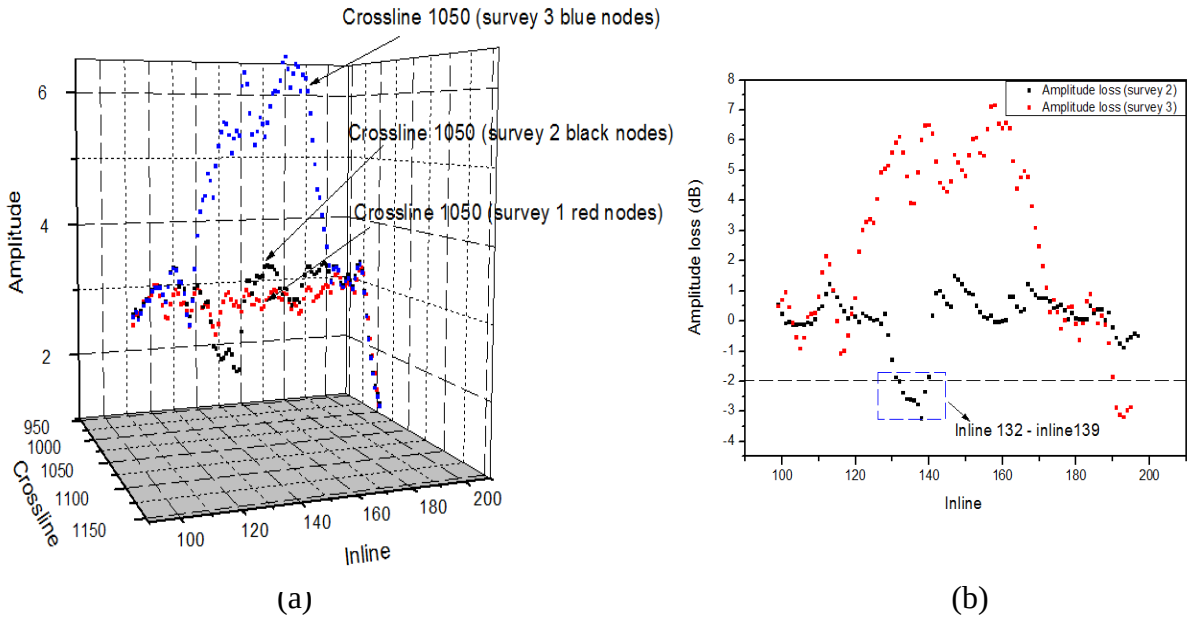

(a) (b)

Figure 4.18 (a)-(b): The variation in amplitudes along the second surface for crossline 1050 (a); corresponding amplitude losses (b)

The blue dashed box in Figure 4.18 (b) shows the inline numbers ranging from 132 to 139. For this inline range, amplitude losses along the second surface is more than -2dB. As shown in Figure 4.13, the PSTM images corresponding to inline 138 and 139 were heavily distorted by amplitude losses along the second surface (shown by red arrow). Figure 4.18 (b) (red nodes) demonstrates well that the amplitude losses were recovered based on Fresnel zone-based infill management. Figure 4.19 (a) shows the amplitude variation associated with crossline 1700. In addition, the amplitude losses are plotted in Figure 4.19 (b). Figure 4.19 (b) shows that in the crossline direction, the amplitude losses in survey 2 are well restored after employing infill management in survey 3.

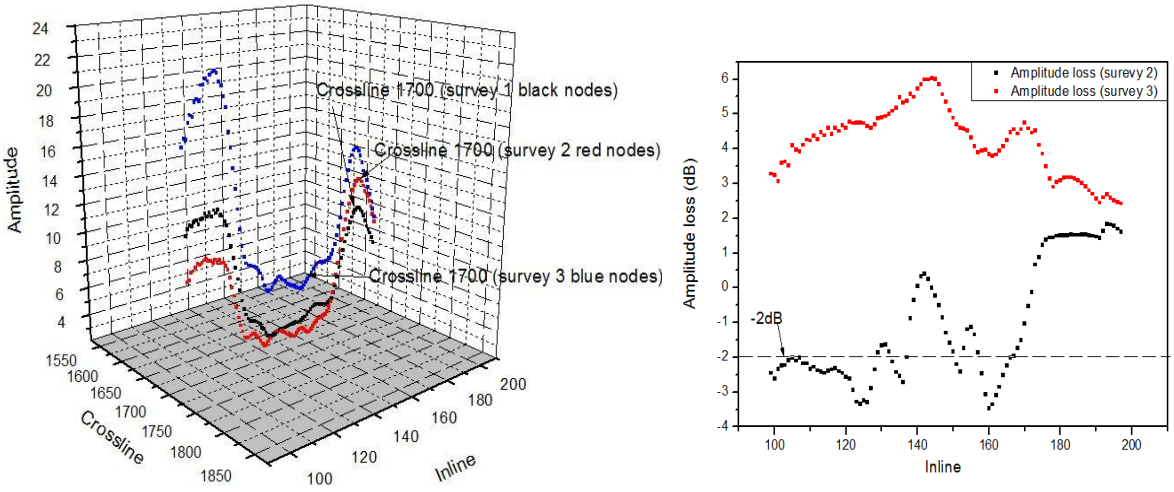

(a) (b)

Figure 4.19 (a)-(b): The variation in amplitude along the target surface for crossline 1700 (a); corresponding amplitude losses (b)

Based on the PSTM images and the amplitude analysis carried out for both inline and crossline sections, it is well demonstrated that Fresnel zone-based infill management effectively improves the quality of the seismic images. However, in our investigation, Fresnel zone-based infill management also can not restore all 'coverage holes'. As an example, Figures 4.20 (a)-(c) show PSTM images for the three surveys associated with inline 165.

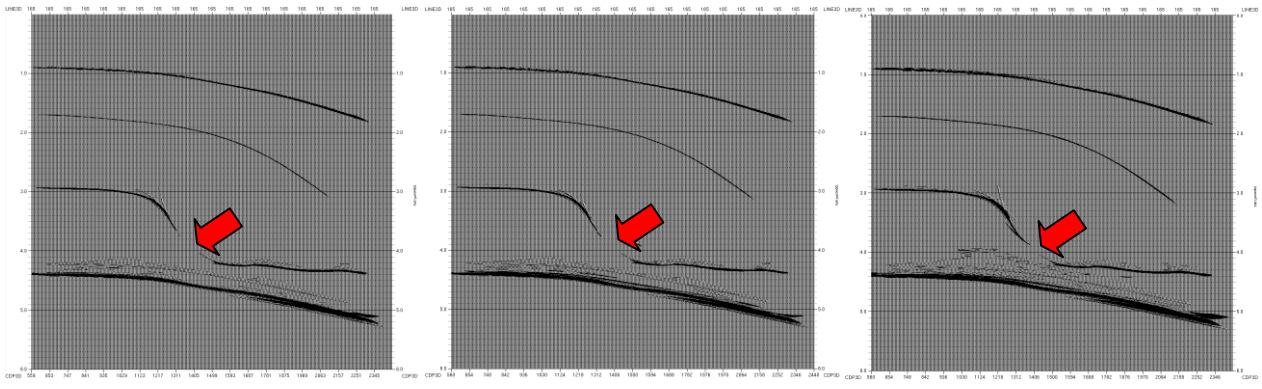

(a) (b) (c)

Figure 4.20 (a)-(c): PSTM images of the three surveys associated with inline 165; (a) survey 1; (b) survey 2 with feathering included; (c) survey 3 based on infill management.

For the reference survey without feathering in Figure 4.20 (a), the strong dipping structure defining the target surface is poorly illuminated (shown by red arrow).

Correspondingly, in survey 3 (Fig 4.20 (c)) established using Fresnel zone-based infill management, the same dipping structure is still not recovered. In Chapter 2, the basic theory of Fresnel zone-based infill management was introduced. It is based on a series of approximations and hypothesis, among them that all subsurface layers being plane horizontal interfaces. Furthermore, it follows from our analysis in Chapter 3 that the size of the Fresnel zone for a dipping layer gradually decreases when the dipping angle increases. Therefore, as supported from the PSTM images, the theory of Fresnel zone-based infill management breaks down in case of dipping layers.

Hence, one should be aware of the weakness of Fresnel zone-based infill management in cases of complex geology.

Chapter 5 Conclusions

In this thesis, our task has been to evaluate a new concept (Monk 2010) denoted Fresnel zone-based infill. The purpose of this technique is two fold: fill in gaps in data spare caused by feathering employing Fresnel zone binning, and at the same time identify the level of reshooting needed (infill management). The basic technique of Fresnel zone binning was introduced in Chapter 1. The dimensions of a Fresnel zone for a given shot and receiver pair were calculated based on simple models, such as horizontal layers and constant interval velocities, or horizontal layers and constant gradient velocities.

To further analyze the concept, two synthetic models (one simple and one more complex) were employed to simulate seismic surveys (Chapter 2). The simple model consisted of four horizontal layers and constant interval velocities. To include a more realistic geology, three curved interfaces were introduced in the complex model together with a constant velocity gradient model. Furthermore, real navigation lines defined the survey. Based on a coverage analysis using the theoretical formulas in Chapter 1, it was demonstrated that some 'coverage holes' were caused by the feathering on middle and far offsets for both models. However, after Fresnel zone-based infill management, three new navigation lines were added to the survey area and as a result, most of the 'coverage holes' were restored.

In Chapter 3, illumination maps (hit maps) for the complex model were calculated based on ray tracing in NORSAR3D. Employing hit maps, it was also well demonstrated that the 'coverage holes' in the complex model minimized after Fresnel zone-based infill management. Furthermore, a set of tests were carried out to validate the simple Fresnel zone formulas. Comparison between the theoretical calculations and the simulations based on ray tracing showed a very good agreement in case of horizontal layers and constant interval velocities. However, in case of a horizontal layer and gradient velocity, the dimension of the theoretical Fresnel zone in the inline direction is significantly larger than the simulated one both at middle and far offsets. This difference is caused by the poor cosine approximation (c.f Equation 3.1). All theoretical formulas in the article of Monk (2010) were derived for a horizontal layer. To further analyze the Fresnel zone concepts, a dipping layer was considered. It was observed that the dimensions of the Fresnel zone decreased with increasing dipping angle. This implies that the theoretical formula used to estimate the size of the Fresnel zone for a non-dipping layer is not accurate enough for a dipping layer. Furthermore, in case of curved layers, the shape of the Fresnel zone becomes irregular and the true specular points are not located at the mid-point (CMP) coordinate as assumed in the article (Monk 2010).

In Chapter 4, PSTM was employed to further quantify the usefulness of Fresnel zone-based infill management. The PSTM images showed that the continuity of target horizons was poor for the survey including strong feathering. After Fresnel zone-based infill management, the images were significantly improved and with the

'coverage hole' apparently being removed. An analysis of the amplitude losses was carried out and demonstrated a satisfactory amplitude level not lower than -2dB after Fresnel zone-based infill management. However, some PSTM images show that the criterion of Fresnel zone-based infill management still breaks down when the target structure is complex, f.ex. strong dipping layers.

This thesis has demonstrated that the Fresnel zone binning concept proposed by Monk (2010) is still immature. In case of more gentler feathering, interpolating data using Fresnel zone binning can save reshooting. For cases including strong feathering, the Fresnel zone concept can still represent an effective infill management technique. Hence, based on such analysis, the cost of infill shooting can be minimized. However, the whole concept is based on simple theoretical formulas to predict the Fresnel zone dimensions. This implies that the concept of Fresnel zone binning should be used with care in case of complex geological models (target zones). Simulations carried out during this thesis work also support this conclusion.

References

Capelle, P. 2008. "Intelligent Infill" for cost effective 3D seismic marine acquisitions Extended Abstract SEG Las Vegas 2008 Annual Meeting P.135-137

Claerbout, J.F. 1985. "Imaging the Earth's Interior", Published by Blackwell scientific ISBM 0-86542-304-0

Lindsey, J.P. 1989. "The Fresnel zone and its interpretive significance", The Leading Edge, October issued P.33-39

Long, A. 2006. "Understanding the azimuth challenge", PGS technical note. December 1

Monk, D.J. 2009. "Fresnel zone binning: Application to 3D seismic fold and coverage assessments". The Leading Edge, March, P. 288-292.

Monk, D.J. 2010. "Fresnel Zone Binning: Fresnel zone shape with offset and velocity function". Geophysics, February 2, Vol 75, No.1, P. T9-T14.

Sheriff, R.E. 1980. "Nomogram for Fresnel-zone calculation", Geophysics, May Vol.45. No.5 P. 968-972

Strand.C, Buchan.I, and Mostavan.A, PGS, Ross.J and Monk.D, Apache, 2008, "Evaluating infill requirements when acquiring a marine 3D seismic survey along pre-plot lines", SEG Las Vegas Annual Meeting P. 70-74

Yilmaz, Ö, 1988, "Seismic data processing", Published by Society of Exploration Geophysicists, ISBN 0-931830-40-0, P. 385-389